STUDY OF MICROWAVE-ASSISTED MAGNETIZATION DYNAMICS IN MAGNETIC FILMS AND STRUCTURES

VELLEYUR NOTT SIDDHARTH RAO

NATIONAL UNIVERSITY OF SINGAPORE

2014

STUDY OF MICROWAVE-ASSISTED MAGNETIZATION DYNAMICS IN MAGNETIC FILMS AND STRUCTURES

VELLEYUR NOTT SIDDHARTH RAO

(*B.Tech (1st Class with Distinction), SRM University, India*)

A THESIS SUBMITTED FOR THE DEGREE OF DOCTOR OF PHILOSOPHY

DEPARTMENT OF ELECTRICAL AND COMPUTER ENGINEERING

NATIONAL UNIVERSITY OF SINGAPORE

2014

DECLARATION

I hereby declare that the thesis is my original work and it has been written by me in its entirety. I have duly acknowledged all the sources of information which have been used in the thesis.

This thesis has also not been submitted for any degree in any university previously.

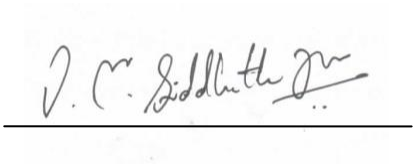

Velleyur Nott Siddharth Rao

January 17, 2014

ACKNOWLEDGEMENTS

I have spent an enjoyable and enriching four years in Singapore, gaining an education that is afforded to very few people. My time here has been a truly rewarding experience, and is a result of the support and guidance of several people during the course of my research. I would like to take this opportunity to thank all of them at this juncture.

First and foremost, I am grateful to my supervisors – Professor Charanjit Singh Bhatia and Assoc. Prof. Hyunsoo Yang, for giving me the opportunity to work and study in a multidisciplinary research group with world-class facilities. They have always encouraged me to work harder and smarter, while giving me enough freedom to explore the field of spintronics on my own without losing sight of the final goal. I am also grateful for their trust in my abilities by assigning me with several important responsibilities in the cleanroom and measurement labs. My experience in working with them has greatly improved me both as a person and as a professional, and will stand me in good stead for the future.

This thesis would not have possible without the experimental and analytical support of Dr. Sankha Mukherjee, Dr. Jan Rhensius and Dr. Jungbum Yoon who went an extra mile and more in their assistance. I would also like to thank Dr. Kwon Jae Hyun, Dr. Kalon Gopinadhan and Dr. Ajeesh Sahadevan for training me during my freshman year on fabrication and measurement techniques.

I have spent my time here in two labs – the Information Storage Materials Laboratory (ISML) and the Spin Energy Laboratory (SEL), and I would like to thank all its members for their useful inputs in both research and

academic matters, and interesting conversations over a cup of coffee. I would like to offer a special thanks to the administrative staff of Ms. Loh Fong Leong, Ms. Habeebunnisa Ellia, Mr. Sandeep Singh Vahan and Mr. Robert Jung at both labs for their superlative efforts in keeping the labs functioning well.

I have enjoyed my research life in NUS due to the presence of colleagues such Gopi, Sagaran, Praveen and Shreya who have been good friends and pillars of support throughout these four years, in more ways than one. I am also grateful to my friends outside NUS including Kushagra, Munami, Sujata, Gagan, Avinash, Faraz, Pushparaj, Abdul Wahab and many others for their valuable support and friendship, and for keeping me on track with the rest of the outside world.

Above all, I would like to thank my parents and my brother for their love, support and understanding throughout my life.

Finally, I would like to acknowledge the financial support for this work by Singapore National Research Foundation under CRP Award No. NRF-CRP 4-2008-06 and the NUS research scholarship offered in collaboration with the Nanocore programme (WBS No. C-003-263-222-532).

ABSTRACT

Spintronics is a new, emerging technology that has shown great promise in solving the scaling issues that beset the CMOS-based semiconductor device industry today. By utilizing the spin of electrons as a new degree of electron freedom, great strides have been made in developing new devices and technologies that are applied in several fields including memory devices, especially magnetic data storage in hard disk drives (HDD). However, current technologies used in HDDs are projected to reach their maximum limit at areal densities of 1 Tb/in^2. Microwave-assisted magnetization reversal (MAMR) has been suggested as an alternative recording scheme to extend areal densities in hard disk drives beyond 1 Tb/in^2. In this thesis, we investigate microwave-assisted magnetization dynamics in different spatial regimes by electrical and optical techniques to understand their influence on reversal processes, and suggest new device design concepts to implement this technology. Time-resolved optical techniques have been developed to study spin wave generation in magnetic structures ranging from large area thin films to sub-micron sized patterned elements, and the interaction of different spin wave modes. We have studied the magnetization reversal process at sub-nanosecond time resolution to identify the effect of propagating spin waves on the reversal process and the reversal modes. These studies present a novel solution for implementing MAMR on high coercivity hard disk media materials of the present and the future.

The dynamics of propagating spin waves in patterned rectangular ferromagnetic thin films are characterized by time-resolved magneto-optical Kerr effect (MOKE) experiments. Spin wave propagation is characterized as a

function of position and bias fields to identify the origins of spin wave interference patterns and non-reciprocal behavior. It is observed that the non-reciprocity of spin waves can be tuned by an external bias field – a promising feature for implementation of spin wave logic devices. A beating interference pattern in the frequency domain is observed at a distance away from the stripline, due to the interaction of two centre modes separated by a relative frequency and phase difference. Spatial dependence studies across the width of the stripe reveal the presence of localized edge modes at lower frequencies than the centre modes. These results are important in understanding the effects of short pulse excitation on magnetization dynamics, a concept that is employed to switch patterned magnetic elements in Chapter 6.

Spin pumping-mediated detection of MAMR is presented as a novel characterization technique to overcome the bottlenecks presented by complex impedance matching issues in spectroscopy techniques. The reversal is detected as the change in the polarity of the measured spin pumping signal. The technique is shown to be suitable for switching studies regardless of material parameters and geometry. It demonstrates its versatility by detecting an indirect signature of domain nucleation and switching in large area thin films of CoFeB. In patterned microwires, partial switching of the microwire array is evident from the presence of two features (peak and dip) in the measured spin pumping signal. This technique is suitable for studying the effect of material variations on magnetization dynamic properties in granular films, amongst others.

MAMR has been extensively investigated by electrical methods, yet the physics of the reversal process is still under debate. Spin waves have been

suggested to initiate reversal, before domain wall dynamics take over as the driving force of the switching mechanism. We present time-resolved X-ray images of MAMR in patterned magnetic elements measured at sub-nanosecond time resolution. Due to the effects of a shape-varying demagnetizing field, spin waves generated along the easy axis of the element are shown to initiate the reversal process followed by the generation of several edge-mode spin waves. Throughout the entire reversal process, spin waves are the driving force and low frequency dynamics such as domain wall dynamics (< 2 GHz) are shown to be largely absent. In addition, the excited spin waves are three times higher in frequency than the microwave excitation signal. This concept of switching is a very promising method for switching high anisotropy magnetic materials such as FePt in the future using a low frequency excitation.

In addition, the fabrication and characterization of nanopillar magnetic tunnel junctions (MTJ) for spin transfer torque (STT) applications is discussed. The STT effect is demonstrated through the current-induced switching sequence of the nano-sized MTJ junctions. Further optimization of the device may lead to a spin torque oscillator, which can be integrated in future hard disk drives as a writing sensor by generating microwaves.

TABLE OF CONTENTS

List of figures

List of tables

Chapter 1: Introduction

The data storage industry is currently one of the world's largest sectors with a revenue well in excess of 9 billion USD in 2012 [1]. This dependence on '*memory storage*' has necessitated intensive research over the years to improve existing data storage devices. Ever increasing demands of devices with higher storage capabilities, faster read and write access times, lower power consumption and smaller physical dimensions have driven the need for intensive research in the field of magnetic data storage. The industry has kept abreast of the demands by physically scaling down the devices according to Moore's Law [2]. However, as the device sizes approach atomic scales, we have witnessed a paradigm shift in the physics that governs the behavior of the devices. In addition to utilizing electronic charge to store data as in capacitors, other natural degrees of freedom in materials such as electronic spin have been considered for applications. This field of research is known as 'Spintronics'. The commercialization of such devices in hard disk drives (HDDs) as read-write heads has brought spintronics to the forefront of the information technology boom, culminating in the 2007 Nobel Prize in Physics to Dr. Peter Grunberg and Dr. Albert Fert.

1.1 Moore's Law and the scaling trends of devices

Gordon Moore of Intel Corp. predicted in 1965 that the number of transistors per square inch on integrated circuits would double every 18 months (Moore's Law). Since this famous prediction, device sizes have scaled down immensely but are now approaching a limit with conventional CMOS technologies. To overcome this barrier, new technologies to harness other

electronic properties have to be developed. Exploiting the property of electronic spin has opened up an entirely new avenue of device research – both in fundamental studies and commercial applications. Today, it is possible to simultaneously manipulate both the electronic charge and spin as is done in HDDs and novel devices, such as magnetoresistive random access memory (MRAM). The discovery of giant magnetoresistance (GMR) – in which two stable electronic states (high resistance and low resistance) were accessed by reorienting the relative magnetizations in a multi-layer magnetic film stack – by Fert [3] and Grunberg [4, 5] in 1988-89 and the succeeding research done by Stuart Parkin [6-8] in the area of interlayer exchange coupling led to the incorporation of GMR devices as read heads in HDDs. The tunnel magnetoresistance effect (TMR), which involves a quantum mechanical phenomenon of an electron tunneling across a thin insulating barrier between two ferromagnetic conductors, is able to generate magnetoresistance values at least 10 times higher than GMR heads [9-13]. This huge increase has found immediate acceptance in HDDs as read heads. Along with improvements in the read-write capabilities of HDDs, the magnetic media has also seen huge improvements, as witnessed by the steep increase in areal densities offered by HDDs between 1995 – 2005. The growth of the areal density in HDDs with time is illustrated in Fig. 1-1.

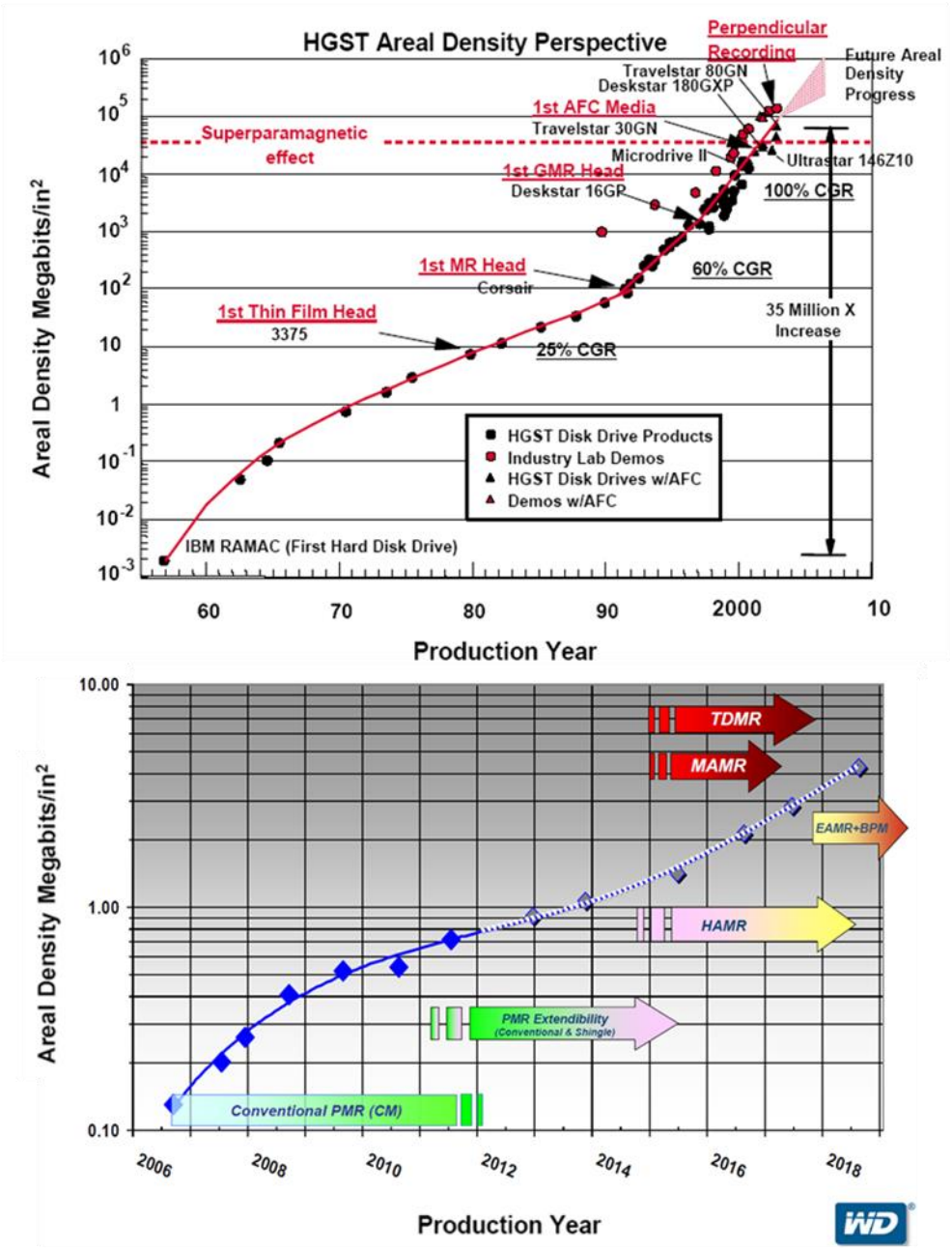

Figure 1-1: Areal density growth in HDDs over the years [14].

In magnetic media, there was a shift from longitudinal magnetic recording (LMR) to perpendicular magnetic recording (PMR) technology to overcome the impending superparamagnetic limit, as shown in Fig. 1-1. As grains become smaller in size, the magnetic anisotropy energy (K_uV, where K_u is the anisotropy constant and V is the volume of the grain) of the grains decrease. The thermal energy (k_BT), on the other hand, remains constant.

Hence, as the grain sizes decrease, the relative proportion of the magnetic anisotropy energy to the thermal energy is reduced. When the thermal energy due to fluctuations exceeds the magnetic anisotropy energy of the grain, random switching of the grains occurs, resulting in data corruption. The size regime at which these effects occur is known as the 'superparamagnetic limit'. Today, cutting-edge research in PMR media has resulted in an areal density of 700 Gb/in^2 in HDDs being shipped to consumers. The grain sizes in current CoCrPt-based PMR media are ~7 nm and the technology is expected to reach its saturation potential near 1 Tb/in^2 due to the bottlenecks posed by superparamagnetism with further reduction in grain sizes. Therefore, high anisotropy materials such as $L1_o$ FePt are being intensely researched as future media alternatives. However, increasing the magnetic anisotropy alone can lead to further problems such as an increase in the required switching fields. A trio of issues known as the magnetic or media 'trilemma' encapsulates the bottlenecks in current magnetic media technology, and is discussed in greater detail in Chapter 2, Section 2.4.2. Thus, materials such as $L1_o$ FePt have to be considered in conjunction with alternative technologies such as bit-patterned media (BPM) or energy-assisted recording techniques (EAMR). These technologies are also discussed in further detail in Sections 2.4 and 2.5 of Chapter 2. These techniques are summarized in Fig. 1-2.

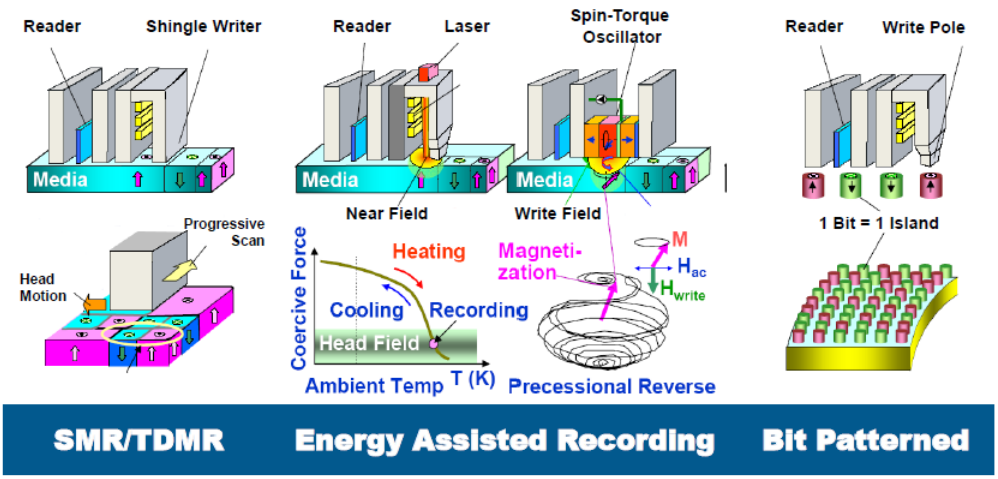

Figure 1-2: New alternatives in magnetic recording present a way to overcome the superparamagnetic limit [15].

In the technique of BPM, the media is grown or processed into individual magnetic islands separated by non-magnetic material to avoid magnetic coupling. Several methods of forming BPM are being considered, such as electron-beam lithography defined film, self-assembling media using block copolymers, and mold-based formation of BPM. The other way to go is with EAMR using techniques that would reduce the effective coercivity of the magnetic media and thus assist in magnetization reversal. Heat-assisted magnetic recording (HAMR) and microwave-assisted magnetic recording (MAMR) are the two most important EAMR techniques being widely studied as of today. Both have the potential to exceed an areal density of 3 Tb/in^2, but are well away from large-scale commercialization due to issues in implementation. These include integration issues with the current head assembly in HDDs, low power outputs of the MAMR-based write heads, heat dissipation and material deformation issues with HAMR, amongst others. These issues are discussed in greater detail in Chapter 2 of this thesis. Of the

two technologies, MAMR has been chosen as the subject of focus for this research work. Practical implementation of MAMR in hard disk drives requires the use of high coercivity perpendicular magnetic anisotropy (PMA) materials (such as FePt and CoCrPt) as magnetic media, in addition to the head-related problems stated above. Given the limitations posed by the magnetic trilemma, it is imperative that a more efficient method of generating microwave-assisted switching processes is developed, and this requires an in-depth understanding of the switching process. This research dissertation will, therefore, mainly focus on understanding the fundamental physics governing the MAMR process. It will also present results that have the potential to overcome bottlenecks in the implementation of MAMR on future magnetic media.

1.2 Objectives and organization of thesis

In this thesis, we have attempted to resolve the issues of microwave-assisted magnetization reversal in a two-fold manner:

(a) To gain a fundamental understanding of the mechanism of microwave-assisted magnetization reversal and study the influence of shape and patterning effects on the reversal process, and

(b) To suggest improvements in current characterization techniques to utilize the magnetization dynamic information and gain more insight into the reversal process.

With these goals in mind, we have developed novel experiments to extract useful knowledge about MAMR such as time-resolved imaging experiments, amongst others. As such experiments have few precedents and the field is not well explored, we have consciously chosen to work on soft

magnetic materials rather than high coercivity PMA materials. Consequently, this thesis has been organized into seven chapters. Chapter 1 gives an introduction to the world of magnetic data storage and the progress made over the years. It also provides a brief introduction to the field of spintronics and how the utilization of electronic spin has revolutionized the HDD industry. An outline of the challenges facing the industry today and the potential solutions are presented. One such solution, known as MAMR, is presented as the chosen area of study. A set of research motivations and objectives are presented to support this chosen area of research. A more detailed summary of the MAMR technology and the roadmap for future application of MAMR in HDDs is given in Chapter 2.

Chapter 2 delves on the concepts of magnetism, magnetization dynamics and spin-dependent transport. A detailed review of past and current magnetic recording technologies, including LMR and PMR, is presented. Amongst the suggested alternatives, emphasis has been given to MAMR. An overview of the work done on MAMR along with the research and commercial challenges is presented. Current and future directions of research in MAMR from an industry perspective are also presented. A discussion on spin transfer torque (STT) and spin waves is provided at the end of this section as these are critical to possible practical applications of MAMR.

Chapter 3 describes the experimental methods used in this research work, including sample fabrication processes, measurement setup and techniques. The time-resolved measurement procedures, namely pump-and-probe experiments for electrical and optical measurements, are discussed in detail. This chapter also presents the efforts made towards fabricating an STT-based

device in-house. The structural and electrical characterizations are presented, culminating in the current-induced switching seen in nanopillar MTJ junctions. The necessary improvements required for fabricating good quality STT devices are briefly discussed.

The literature review of MAMR in Chapter 2 brings us to the conclusion that spin wave dynamics can be excited by microwave signals in patterned magnetic structures. However, the influence of these spin wave dynamics on the precessional magnetization reversal process is not well understood and requires a more detailed study. In Chapter 4, this research problem is tackled by time-resolved measurements of spin wave dynamics in patterned structures and the non-reciprocal behavior of magnetostatic surface spin waves is discussed. The observation of a unique beating interference pattern is presented and the origins of this phenomenon are discussed. The implications of beating due to multimode spin wave excitation are summarized at the end of the chapter.

Chapter 5 presents a novel characterization technique for MAMR in in-plane anisotropy materials. The advantages of this method over conventional FMR and MOKE-based spectroscopy studies lie in its simple data acquisition technique which utilizes the spin pumping phenomenon to convert a time-varying magnetic signature to a simple DC output voltage. Reversal modes in magnetic structures of different aspect ratios are also discussed.

Chapter 6 shows time-resolved images of an MAMR process in patterned magnetic elements for the first time. The contributions of spin waves in the reversal mechanism of these elements are analyzed with the help of experiments and micromagnetic simulations, and a method to generate high

frequency spin waves to assist reversal with low frequency microwave excitation is proposed. Fourier analysis of the switching data also highlights the existence of multiple spin wave modes that influence the reversal process, as hypothesized in Chapter 4.

Chapter 7 summarizes the thesis and presents future prospects for MAMR research and technology.

Chapter 2: Literature Review

2.1 Magnetism of materials

A particle moving through space possesses angular momentum, a vector, defined by **L** = **r** × **p**, where **r** and **p** are the position and momentum vectors respectively of the particle. This is also known as orbital angular momentum, usually when describing a particle that is orbiting around a central attraction. Now consider the case of an electron. The electrons occupy discrete energy levels and are orbiting around the central nucleus. From the point of view of classical physics, an orbiting electron (μ_{orb}) carrying an electric charge will generate a tiny current loop which will produce a dipolar magnetic field. The strength of this field is given by its magnetic moment or spin angular momentum (μ_s) defined as:

$$\mu_{orb} = -\frac{e}{2m_e} L, \mu_s = -\frac{e}{m_e} S \tag{2.1}$$

where e is the charge of an electron, m_e is the mass of the electron, L is the orbital angular momentum, and S is the spin angular momentum. Since the electrons in an atom occupy discrete energy levels, the angular momenta are also quantized. Hence, the possible values for the magnitude S of the spin angular momentum is:

$$S = \sqrt{s(s+1)}\hbar \text{ ; s = 0, ½, 1, 3/2, 2 …} \tag{2.2}$$

Thus, any vector component of S can have only two possible values, namely $\pm 1/2\,\hbar$. This quantization of spin was first proposed by Niels Bohr and experimentally demonstrated by Otto Stern and Walther Gerlach in 1922 [16].

A beam of particles was sent through an inhomogeneous magnetic field and collected on a screen. The deflection of the particles into two neat lines, separated by a small distance, indicated the presence of electron spin. This confirmation of 'directional quantization' in a material under the influence of a magnetic field led to intense study in the field of magnetism. Magnetic transport studies on ferromagnetic materials are especially interesting given the strong influence of electron spin on the material properties of the ferromagnet. The theoretical understanding of ferromagnetism in transition metal elements such as Co, Ni and Fe, developed in the 20^{th} century, attributes the net magnetic moment to the presence of partially-filled 3*d* orbitals. These orbitals possess a number of unpaired spins, due to the electron filling rules laid down by the Pauli Exclusion Principle and Coulomb repulsion, and being more localized orbitals, there are strong exchange interactions between their magnetic moments. These interactions are believed to cause an asymmetric energy profile between the up and down spin electrons, resulting in an asymmetric spin profile at the Fermi level in the material as well seen in Fig. 2-1. As the transport properties of a metal are determined by the electrons at the Fermi level, the spin imbalance in the conduction electrons give rise to a spin-polarized current. This model, known as the Stoner model of ferromagnetism [17], however, does not differentiate between the localized *d*-orbital electrons and the less-localized *sp*-orbitals. The Stoner model, though, establishes that the necessary criterion for ferromagnetism is the presence of strong quantum exchange interactions (leading to high magnetic susceptibility) that overcome thermal fluctuation effects to present a net magnetic moment. This spin imbalance in a ferromagnetic material also results in the creation of

free energy within the material system comprising of several energies due to magnetostatic effects, anisotropy effects, exchange interaction and Zeeman field effects, amongst others which will be discussed in the following pages.

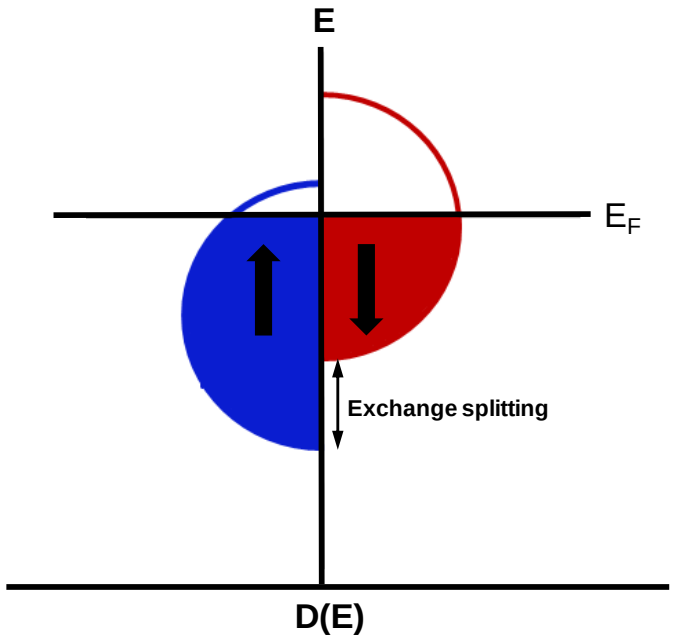

Figure 2-1: Schematic of the Stoner model of ferromagnetism. The density of states D(E) is shown on the *x*-axis, and the energy E on the y-axis. Due to Hund's rules of coupling, we see an exchange splitting in density of states (DOS) between opposite spins. Thus, at the Fermi level E_F, we see a net spin moment.

2.2 Magnetization dynamics and the considerations for micromagnetic modelling

As is the case with the motion of an electron in a magnetic field, the magnetization of a material also tends to undergo a precessional motion around a local effective field when drawn away from its equilibrium state. If this precession were to be a dissipation-less motion, then the magnetization would continue to precess as though on a constant energy surface for infinite time. In reality, these precessions always tend to damp down and die out, returning the magnetization to an equilibrium state. To account for these

sources of energy loss, Landau and Lifshitz introduced a phenomenological damping torque in the equations of dynamic motion in 1935 to form the Landau-Lifshitz equation of magnetization dynamics. The damping term was modified by Gilbert to reflect the dependence on the time-derivative of the magnetization, rather than the effective magnetic field. This is known as the Landau-Lifshitz-Gilbert (LLG) equation, and it is this form that is commonly used to model the behavior of magnetic dynamics in hard disk drives, amongst other applications.

Landau-Lifshitz form: $$\frac{dM}{dt} = -\gamma_o^{'}(M \times H_{eff}) - \frac{\lambda}{M_s} M \times (M \times H_{eff}) \tag{2.3}$$

Gilbert form: $$\frac{dM}{dt} = -\gamma_o \left(M \times H_{eff}\right) + \frac{\alpha}{M_s}\left(M \times \frac{dM}{dt}\right) \tag{2.4}$$

γ_o is the gyromagnetic ratio, α is the Gilbert damping parameter, and λ is the Landau-Lifshitz damping parameter. The relation between the two equations can be worked out as shown below:

$$\gamma_o^{'} = \frac{\gamma_o}{1+\alpha^2}, \lambda = \frac{\gamma_o \alpha}{1+\alpha^2} \tag{2.5}$$

The value of γ_o for a free electron is given as 2.21×10^5 $(A/m)^{-1}s^{-1}$, and the SI units for M are in T (Tesla) and for H_{eff} in A/m.

In addition to the above terms, there is one more term that contributes to magnetization dynamics, known as the spin transfer torque. It was postulated by Berger in the late 1970s that magnetization reversal could occur due to the torque generated by spin-polarized electrons in a precessing magnet [18-20]. The first observations were made by Berger's group in moving domain walls

in thin films with currents as large as 45 A. Due to the unfavorable need for large currents, this phenomenon did not attract much interest until 1996 when Slonczewski [21] and Berger [22] independently predicted that current flowing perpendicular to the plane in a metallic multilayer can generate a spin torque large enough to reverse the magnetization in one of the magnetic layers. The modified form of the LLG equation to account for this Slonczewski term was given as:

$$\frac{dM}{dt} = -\gamma_o \left(M \times H_{eff} \right) + \frac{\alpha}{M_s} \left(M \times \frac{dM}{dt} \right) + \frac{\gamma_o}{M_s V} m \times \left(m \times M \right) \qquad (2.6)$$

where *m* represents the magnetization of the free layer in a magnetic multi-layer system, and *M* represents the magnetization of the pinned layer.

The spin transfer torque (STT) phenomenon is extremely useful following the discoveries of giant magnetoresistance (GMR) and tunnel magnetoresistance (TMR). Potential applications have included non-volatile memories such as STT-RAM, high frequency microwave devices such as spin torque oscillators (STOs) and magnetic sensors. These applications, along with the STT effect, will be discussed in greater detail towards the end of this chapter.

From the LLG equation modified with the Slonczewski term, we can depict the orientation of the forces acting on a magnetic moment in the ferromagnet. The precessional torque causes the magnetization to precess about the effective magnetic field in the path described, while the damping term tends to align it in the direction of the effective field. The spin transfer torque tends to pull the magnetization away from its equilibrium state, thereby making it more unstable. At a certain threshold, the spin transfer torque

overcomes the damping torque and reorients the magnetization in the opposite direction. The absolute magnitude of M remains constant throughout the motion. An illustration of the forces acting on the magnetization is shown below in Fig. 2-2.

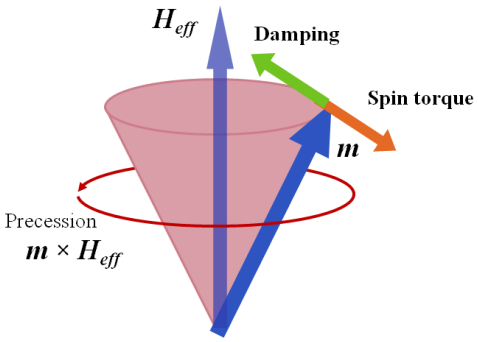

Figure 2-2: Direction of the three torques in the LLG equation during precessional motion.

2.3 Magnetic materials as storage media

As businesses and personal computing applications look to maximize every competitive advantage, the demand for data storage has skyrocketed to record highs. Over the past four decades, not only has the capacity of storage drives increased exponentially, the cost per bit has also gone down in similar fashion as postulated by Gordon Moore. For the past twenty years, magnetic recording technology has served as the mainstay for large capacity and high data density storage devices, while magnetic recording media goes even further back in time with respect to real-world applications. Introduced in principle by Oberlin Smith in 1878, the first demonstration of magnetic recording was a signal recorded on a wire around a drum by Valdemar Poulsen in 1898. Since these humble beginnings, the magnetic tape recorder application was patented in 1928, and widely used in early computers such as

the UNIVAC, ENIAC and other IBM mainframes. Magnetic core memory, which consisted of several tiny magnetic toroids (cores) through which wires were threaded to read and write information, was developed in the late 1940s and used as the predominant memory between 1955 and 1975 [23]. Tape memory usually served as a back-up or secondary memory to core memory and its variants such as core rope memory, bubble memory, thin film memory or twistor memory. A breakthrough was being made in parallel, however, at the IBM research centers in the form of the first hard drive – the 350 RAMAC [23, 24]. The RAMAC was the size of two refrigerators for a measly storage space of 5 MB. The materials used for storage at that time were barium ferrite ($BaFe_2O_4$) and iron oxide (Fe_2O_3) magnetic particles of dimensions ~0.5 μm. With the advent of thin film technology, the storage media was a magnetic thin film of uniform and exchange decoupling grains having high anisotropy and coercivity, and these films were arranged on platters that were stacked vertically. Thus, there was a significant increase in storage capacities that have seen consistent growth ever since – areal densities have increased by 10^8 times over the past 50 years [25].

In conventional hard disk drives (HDDs), the data is stored as bits on magnetic media material. Each bit can consist of several grains of the magnetic media. The schemes used to record information on these bits have also undergone improvements over the years. Earlier, longitudinal magnetic recording (LMR) was predominantly used to record data as magnetic moments aligned parallel to the media surface. With increasing demand for higher areal densities, the industry has switched to perpendicular magnetic recording (PMR) since 2006. In PMR, the data is written such that the magnetic

moments are aligned either into or out of the plane of the media surface. Thus, the effective bit area has gone down, thereby increasing the storage density limit. These recording schemes will be discussed in detail in the following pages as background to the motivations of this dissertation.

2.4 Conventional and future recording schemes

2.4.1 Longitudinal magnetic recording (LMR)

The longitudinal magnetic recording scheme is used to write information on bits along the surface plane in magnetic media made using the thin film technology. The materials of choice are Co-based alloys such as CoPt, with the presence of additive elements such as Cr, B and Ta [26-30]. These CoPt alloys are grown epitaxially in a hexagonal close-packed structure (hcp) with a strong anisotropy along the *c*-axis. The Pt atoms give a strong anisotropy to the media, thus increasing its coercivity. The additive elements move to the grain boundaries, resulting in efficient segregation of the magnetic grains and suppress any exchange coupling between them. Since the *c*-axis is usually oriented in the out-of-plane direction, a Cr-based underlayer is used before the deposition of the CoPt to direct growth along the (1120) crystallographic plane. The grain sizes are ~30 nm for areal densities in the range of 100 Gb/in^2 [31]. Figure 2-3 shows the schematic of a read/write head in the LMR scheme.

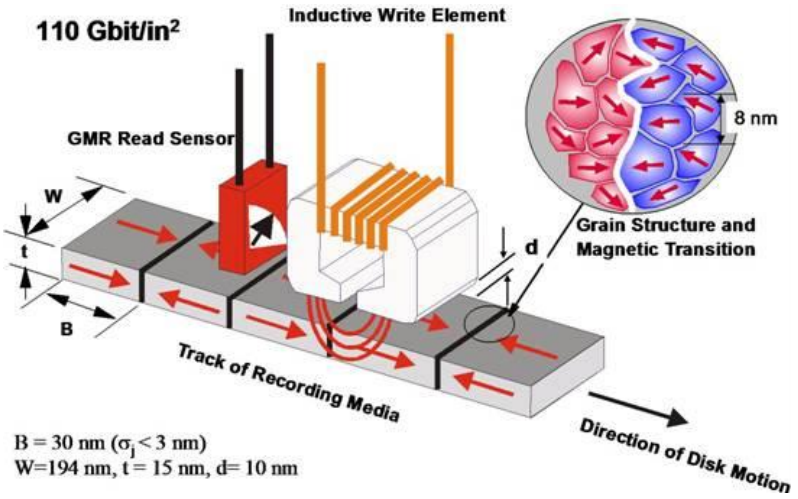

Figure 2-3: Schematic of LMR and the grain boundaries in the magnetic media [32].

The write head is an inductive pole with an air gap positioned over the media. The magnetic field through the pole exhibits fringing at the air-gap which is used to write data into the magnetic bit. The read head used is a conventional GMR head and the presence or absence of a magnetic transition is read as a '1' or a '0' respectively. The bit size in LMR media is around 4 μm × 0.2 μm. To achieve a reasonable signal-to-noise ratio (SNR) in conventional media, the number of grains per bit is very important. As the demand for areal densities increased above 100 Gb/in^2, the grain size in LMR began to approach the superparamagnetic limit [33] – a physical limit at which the thermal fluctuations in the grains are comparable to its anisotropy energy. Because of this, the bits can randomly flip their magnetizations, resulting in data corruption. A temporary solution was found in the form of antiferromagnetically coupled media (AFC-LMR) [34-36]. Two magnetic layers sandwiching a thin Ru layer maintain an anti-parallel magnetic orientation with respect to each other. This configuration, akin to antiferromagnetic coupling, stabilizes the magnetization, thereby increasing its

anisotropy energy and suppressing superparamagnetism [7]. However, at densities ~130 Gb/in^2, the increased packing densities and size reduction of the grains result in higher demagnetizing fields and more crosstalk. Perpendicular magnetic recording was presented as a solution to these problems.

2.4.2 Perpendicular Magnetic recording (PMR)

In the mid to late 1970s, Iwasaki and Takemura [37, 38] proposed a number of recording schemes such as single-pole head, CoCr alloy media with a perpendicular anisotropy, and recording media with soft magnetic underlayers. However, it was not until 2005 that intensive research was carried out to incorporate perpendicular magnetic recording into HDDs. The main reason for this was to overcome the superparamagnetic limit that was being faced by LMR. To achieve a high signal-to-noise ratio (SNR) with increasing areal densities, the number of grains per bit has to increase. In LMR, this requires a reduction in the grain size, which leads to increasing demagnetizing fields in the grain and the onset of superparamagnetism. This causes circular magnetization to be formed in LMR if thick films were used and as a result, output voltages are severely affected. These disadvantages necessitate a switch to PMR. In PMR, the demagnetizing fields of the grain are oriented out of the plane, as shown in Fig. 2-4. Thus, a reduction in lateral grain size does not affect the demagnetizing effect and avoids the onset of superparamagnetism.

In PMR, the media is written by means of a single pole head. The unique feature in PMR is the presence of an additional layer in the media known as the soft magnetic underlayer (SUL) [39, 40]. As seen in Fig. 2-4, the media is written by the gap field, and not by the fringing field as in LMR. The

SUL layer is made of a material that exhibits high M_s, high magnetic permeability (high μ) along the circumferential direction and low μ along the radial direction. Due to these characteristics and the ability of the SUL to conduct flux easily, it is possible to generate very intense fields in the gap where the media bits are written. This technology makes it viable to use materials with high magnetocrystalline anisotropy and smaller grain sizes. While the field required to write into such media is higher, once it is set, the magnetization is inherently more stable.

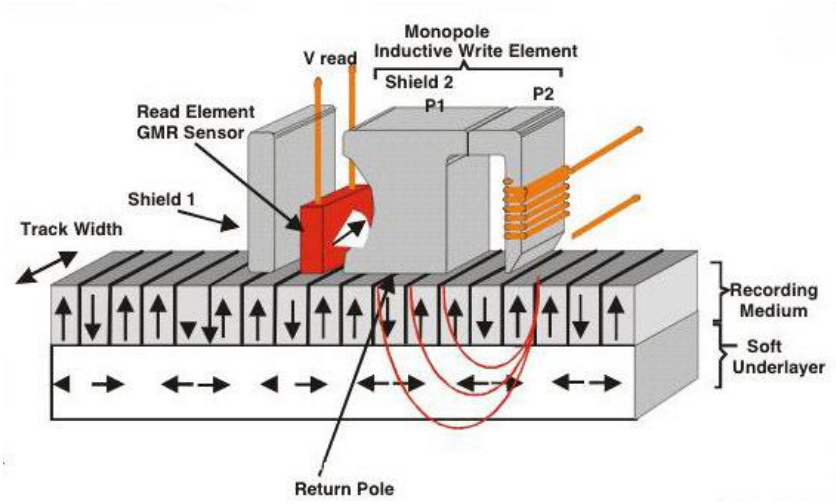

Figure 2-4: Schematic of PMR. The flux return path through the thicker pole head is spread out over several bits, and hence will not disturb their orientation [32].

PMR has been tested on CoCrPt alloys [41], CoCrPt-oxide based alloys [42, 43], CoPt alloys [39] , amongst many others. The oxide materials serve to promote grain segregation while the Ru underlayer is grown in a textured *hcp* orientation to promote the same *c*-axis anisotropy in the magnetic media [44]. The materials of choice for SUL are amorphous materials such as CoTaZr or FeCoB [45-47]. To minimize the spike in the readback signal arising from domain wall transitions, a spacer layer is used to antiferromagnetically couple

the SUL to the media. The flux path through the SUL ensures that the interference between adjacent tracks is greatly minimized.

PMR has undergone significant improvements in the past eight years and the variation in the choice of the magnetic layer, SUL, intermediate and under layers has pushed back the onset of the superparamagnetic limit on PMR. Current industry standards in areal densities are at 700 Gb/in^2 [48]. As a result of these improvements, the cumulative growth rate (CGR) in the HDD industry has seen a steady 40 % increase since 2007 [49].

Media trilemma

The continuous improvements in PMR technology are believed to have extended its areal density limits to 1 Tb/in^2. Beyond this, the bottleneck appears in the form of a set of limiting conditions known as the magnetic trilemma shown in Fig. 2-5 [50], concerning the thermal stability, SNR, and writability of the media material. The superparamagnetic limit is the source of the thermal stability issues. This term was coined by Neel in 1949 and demonstrated later that at elevated temperatures, ferromagnets behave like paramagnets due to excess thermal fluctuations [51]. The term 'superparamagnet' was coined to account for the higher M_s values seen in ferromagnets. At this limit, the grain sizes are small enough to flip under the effect of thermal fluctuations [52, 53]. The magnetization is held in place by the magnetocrystalline anisotropy of the grains, and the ratio of the thermal energy to the anisotropy energy is used as a figure of merit to discuss the stability. For HDDs to have a data retention period of 10 years, this ratio defined as [40]:

$$\frac{K_u V}{k_B T} > 40 - 60 \tag{2.7}$$

where K_u is anisotropy constant, k_B is the Boltzmann constant = 1.38 × 10^{-23} $m^{2}.kg.s^{-2}.K^{-1}$, T is the absolute temperature in Kelvin (K), and V is the volume of the magnetic grain.

If the onset of the superparamagnetic limit is avoided by using larger grains, the SNR is affected due to the presence of fewer grains per bit [39]; the current grain size at areal density of 600 Gb/in^2 is ~7 nm [39, 54]. As a result, research efforts are now concentrated on manufacturing materials with high magneto-crystalline anisotropy and optimizing growth techniques to make grain sizes as small as possible. A consequence of these efforts has been a significant increase in the coercivity H_c of the media material, thereby affecting the writability of such media. Currently, the maximum magnetic field that can be generated by the write head is ~2.4 T [50], and this can be a critical issue in using high-K_u materials as the media.

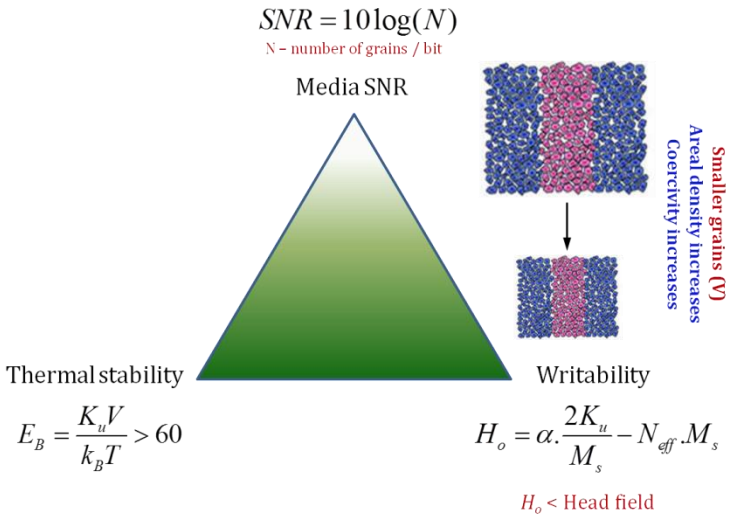

Figure 2-5: Considerations of the magnetic trilemma.

To overcome the above issues, several changes in media fabrication and recording techniques have been suggested. These include using exchange-

coupled composite media (ECC), bit patterned media (isolated magnetic islands), and energy-assisted recording techniques. In BPM, the recording layer is patterned into physically separated magnetic islands. Each island represents one bit of data. Thus, in BPM, the volume of the magnetic island increases ensuring the thermal stability of the bit (K_uV/k_BT, V – volume of the bit). Such a system does not require high K_u magnetic materials. The magnetic decoupling present in patterned media, allows for increased data densities. Thus, the superparamagnetism issue is mitigated.

On the other hand, in EAMR, the change is in the recording technology for storing data in high K_u continuous magnetic media. Using high K_u materials permits the fabrication of thermally stable, smaller grain sizes. By replacing current CoCrPt-based PMR media with high K_u materials such as $L1_0$ FePt, an increase in switching field values is expected. In EAMR, an additional energy (thermal or microwave) is delivered to the magnetic media bit resulting in a decrease in the effective coercivity of the magnetic bit. Under such conditions, the required switching field also drops to reasonable values. Therefore, EAMR is able to bypass the superparamagnetic limit.

The scope of this thesis is limited to implementing new recording techniques in HDDs to reverse new high coercivity media materials with ease. Hence, we will concentrate on energy-assisted magnetic reversal techniques from this point onwards. Suffice to say, the research in the field of media is currently concentrating on making exchange-decoupled $L1_o$-phase FePt the material of choice as PMR media, and as BPM in the future.

2.5 Energy-assisted recording

Energy-assisted recording is a new class of recording techniques that aims to assist the magnetization reversal process by an external magnetic field, rather than completely drive it. These techniques offer the twin benefits of writing capability on high anisotropy materials and smaller sized grains (< 5 nm) while maintaining thermal stability. Heat-assisted magnetic recording (HAMR) and microwave-assisted magnetic recording (MAMR) are the two techniques that are currently being actively researched for areal density requirements > 1 Tb/in^2. In HAMR, a laser source is used to locally heat the magnetic media, thereby reducing its coercivity such that the magnetization reversal can be achieved at reduced applied magnetic fields [55]. Marked improvements in the coercive force temperature gradient have been made with materials research more suited to the HAMR application. In MAMR, commercial media materials such as CoCrPt-SiO_2 of areal densities up to 700 Gb/in^2 have been successfully switched with microwave power of 25 dBm [48]. From numerical simulations, MAMR has shown a capability of achieving 3.5 Tb/in^2 [56], while HAMR can reach up to 10 Tb/in^2 [57].

2.5.1 Heat-assisted magnetic recording (HAMR)

In HAMR, a laser source is used to locally heat a spot on the ferromagnetic material. This causes the material to heat up to temperatures close to its Curie temperature. At these temperatures, the coercivity of the high-anisotropy material drops to values below the head field, thereby making it possible to write the bit. Figure 2-6(a) illustrates a potential setup of the HAMR head in a HDD, while the concept of HAMR recording is depicted in Fig. 2-6(b). Once written, the material is cooled to room temperature rapidly

which causes its coercivity to rise again and thus, provides data protection from stray fields. The origins of HAMR can be traced back to 1954, when a group of PL Corp engineers working for RCA filed a patent, which described the basic principle of using heat in conjunction with a magnetic field to record data [58]. These concepts were applied to magneto-optical recording in the 1980s, until Katayama [59] and Saga [60] independently proposed a new recording technique in 1999 which is now known as HAMR. HAMR overcomes the problems posed by the magnetic trilemma and at the same time, provides a very effective high write field gradient that is independent of the magnetic characteristics of the write head. This can be explained by the relation:

$$\frac{dH_{write}}{dx} = \frac{dH_k}{dT} \times \frac{dT}{dx} \tag{2.8}$$

where H_{write} refers to the net write field gradient and H_k is the anisotropy field. The anisotropy of the ferromagnet vanishes at the Curie temperature; therefore, the first term dH_k/dT is extremely large at elevated temperatures. The second term dT/dx represents the temperature gradient with distance on the media, which is again quite high due to the localized heating source. This gives the high write field gradients in HAMR [55, 61].

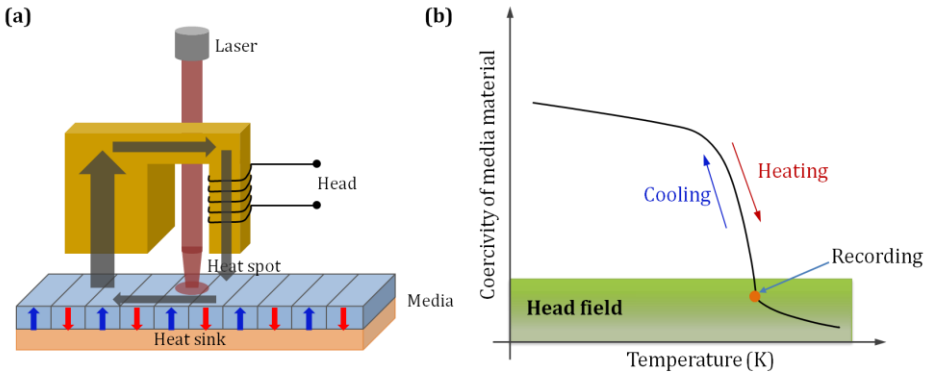

Figure 2-6: (a) Schematic of the HAMR head. (b) Principle of HAMR.

In spite of the advantages evident in HAMR, there are some significant engineering challenges that have yet to be addressed, and are currently bottlenecks to the widespread deployment of HAMR heads in HDDs.

- **Laser source has to be integrated with an efficient light delivery system and also ensure good coupling to the recording media.**

Optical waveguides are a good way to confine the light onto a single spot while near field transducers (NFTs) can be used in conjunction with the waveguides to enhance the optical field in a radial region a few nanometers away from the localized region in the media that is to be written [62, 63].

- **Integration of the laser into the writing head.**

This represents a significant engineering challenge in HAMR. The laser must be incorporated in such a way that the write pole is at an appropriate distance from the optical waveguides. Being too close to the pole will result in increased optical losses and undesirable increase in pole temperature, thereby altering the magnetic field lines. Being too far from the pole will affect the focusing and translational capabilities of the optical spot. The close proximity ensures that adjacent bits are not written [64, 65].

- **Materials engineering of media with specific thermal properties to address thermal diffusion issues in the media stack.**

The heat flow is dependent on the thermal characteristics of the individual layers in the stack. The addition of a heat sink at the bottom of the stack will provide a common path for the major part of lateral heat flows [55, 66].

- **Degradation of carbon overcoat and lubricant at elevated temperatures.**

The media surface is protected by a carbon overcoat coated with perfluoropolyether (lubricant). Laser heating, under HAMR conditions, can cause the diamond-like carbon overcoat to graphitize. In addition, the heat induces thermo-capillary stress in the lubricant leading it to degrade and/or desorb. Hence, lubricants and overcoats need to be developed which can withstand high temperatures, thermal cycling for reliable head/media interface. Additionally it should not affect the efficiency of light delivery to the magnetic media [67, 68].

The above mentioned challenges show that there is still some way to go before HAMR can be incorporated into HDDs on a large scale. There are alternative methods to incorporate energy-assisted recording in magnetic storage devices, and one such scheme is MAMR. MAMR works on the principle of microwave-induced Larmor precession in the media material which is then switched by the write head field. This circumvents the engineering challenges of HAMR. These factors suggest that it would be easier to integrate a MAMR recording technique into the current write head design. The following sections will discuss the work carried out in the area of MAMR to date and the challenges present in the long-term implementation of MAMR in HDDs.

2.5.2 Microwave-assisted magnetization reversal (MAMR)

The MAMR technique utilizes a microwave field in the frequency range of a few GHz to tens of GHz to assist the reversal process. The microwave field excites spin precession in the magnetic material and if the frequency of precession matches the natural frequency of the media magnetization, the condition of ferromagnetic resonance is established and

maximum microwave energy is absorbed by the magnetic grains, as shown in Fig. 2-7. At this stage, the material can be switched by a magnetic field smaller than the lower bound imposed by the Stone-Wolfarth model. This phenomenon is known as microwave-assisted switching (MAS) and is illustrated by a simple model in Fig. 2-8 below [64, 69].

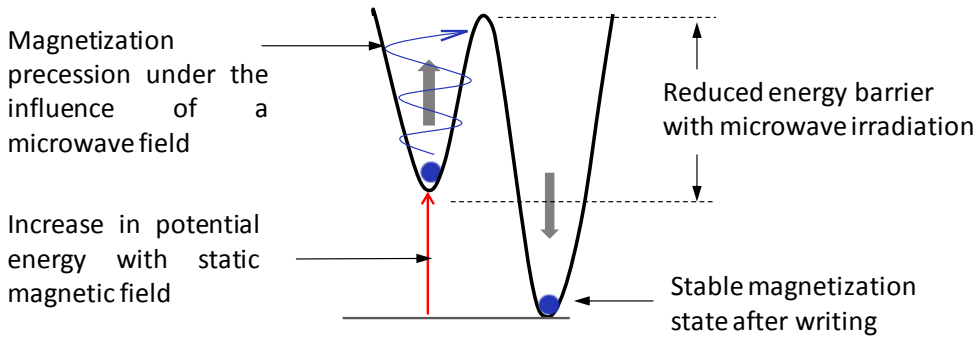

Figure 2-7: Energy diagram explaining the principle of an MAMR process.

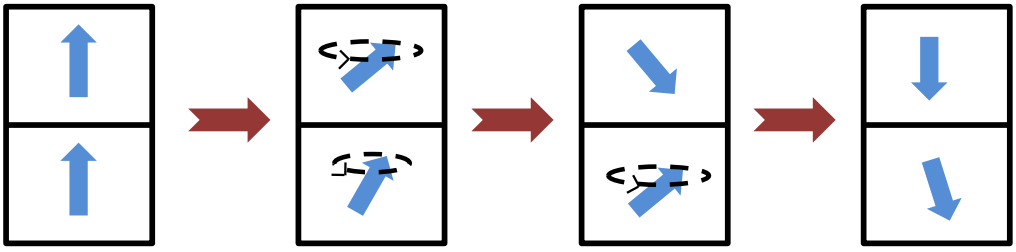

Figure 2-8: Schematic of an MAMR process. The precession is caused by the application of a microwave field (modified from [56]).

Let us consider the effect of a microwave excitation on a single domain particle. The magnetization dynamics of such a particle is well-defined by the Landau-Lifshitz-Gilbert (LLG) equation as

$$\frac{dm}{dt} = -\frac{\gamma}{1+\alpha^2}(m \times H) - \frac{\alpha\gamma}{1+\alpha^2}\left[m \times (m \times H)\right] \tag{2.9}$$

where $H = H_{ani} + H_{ext} + H_{exch} + H_{demag} + H_{rf}$ is the effective field, m is the normalized magnetization vector (M/M_s), γ is the gryomagnetic ratio, and α is the damping constant of the material. While there exists few exact solutions for large non-linear motions of the magnetization M undergoing dynamics,

this issue can be partially resolved by considering a rotational symmetry around a certain axis. For ease of calculation, we consider this to be the *z* axis and as a result, the following assumptions are made in a rotational symmetric system:

(a) The damping parameter (α) is a function of H and m, and is independent of the rotational chirality with respect to the reference frame about the *z*-axis.

(b) The crystal anisotropy is uniaxial and is defined as $H_{ani} = \left(\frac{2K_1}{\mu_o M_s^{\,2}} \right) \mathrm{e}_z$, where $\mathbf{e_z}$ is the direction oriented along the z-axis.

(c) The single domain particle is assumed to have a spherical symmetry.

Assuming that the microwave field H_{rf}(t) is circularly polarized, has a constant amplitude H_{rf}, and an angular frequency of ω, the solution of Eq. (2.9) has been previously derived by Bertotti *et al*. [70, 71] in the form of a fourth-order equation

$$\frac{b_n^{\,2}}{1-m_z^{\,2}} - \frac{\left(b_z + m_z\right)^2}{m_z^{\,2}} - \Omega^2 = 0 \tag{2.10}$$

where $m_z = M_z/M_s$, $\Omega = \alpha\omega K_{eff}$, $K_{eff} = \frac{2K_1}{\mu_o M_s^{\,2}}$, $b_z = \frac{\left(\frac{H_{ext}}{M_s} - \omega \right)}{K_{eff}}$, and $b_n = \frac{\left(\frac{H_{rf}}{M_s} \right)}{K_{eff}}$.

Such an equation has four solutions, whose stability can be determined from first order perturbation theory as done in previous works [71-74]. We then arrive at the following stability conditions:

- Stable oscillations : det $A > 0$, tr $A < 0$
- Unstable oscillations, magnetization reversal : det $A > 0$, tr $A > 0$
- Saddle point : det $A < 0$

where,

$$\det A = \frac{{K_{eff}}^2}{1+\alpha^2}\left[\nu^2 - \left(1-{m_z}^2\right)\nu + \Omega^2 {m_z}^2\right], \qquad \text{tr}\, A = \frac{2\alpha K_{eff}}{1+\alpha^2}\left[\nu - \frac{1-{m_z}^2}{2} + \frac{\Omega m_z}{\alpha}\right],$$

and $\nu = \frac{b_z}{m_z} + 1$. Substituting known expressions and simplification by algebra, we arrive at the following expression for the microwave field required for switching at a given applied magnetic field (H_{ext}):

$$H_{rf} = \sqrt{\left(1-\cos^2\theta\right)\left({\nu_o}^2 + \alpha^2\omega^2\right)} \tag{2.11}$$

where:

$$\nu_o = \frac{H_{ext} - \omega}{\cos\theta} + K_{eff}$$

$$\cos^2\theta \geq \left(\sqrt{1 + \frac{\omega^2\left(1+\alpha^2\right)}{{K_{eff}}^2}} - \left|\frac{\omega\sqrt{1+\alpha^2}}{K_{eff}}\right|\right)^2 \tag{2.13}$$

and θ - angle of M with respect to the external field

These equations describe microwave-assisted switching in a single domain particle of spherical shape, while neglecting the effects of other effects in real systems such as domain interactions and spin wave dynamics. Such an assumed system is rarely found in real applications, and numerical solutions are required to obtain the final required microwave fields. Such research is still ongoing, and no purely analytical solution exists for switching with microwave assistance.

The first experimental reports of MAS were by Thirion *et al.* who observed reversal in single Co-nanoparticles through a dc micro-SQUID experiment [69]. Since then, extensive research has been carried out on MAS

by a number of techniques. VNA-FMR spectroscopy has been used to study the reversal of sub-micron wires [75-78], magnetic tunnel junctions [79], and patterned individual element arrays [80, 81] amongst other similar experiments. Nozaki *et al.* demonstrated the first VNA-FMR based experiment by switching an array of 0.36 μm-wide permalloy wires [76]. A reduction in the coercive field by 25% under the influence of a 17 dBm-strong microwave signal was demonstrated. However, a side effect of the reduced switching field is a broader switching field distribution, which was attributed to the presence of multiple nucleation sites on the wires. Moriyama *et al*. [79] demonstrated that it is possible to selectively switch a single magnetic layer in an MTJ by tuning the microwave field strength. Nembach *et al*. [80] showed a 26% reduction in a coercive field of sub-100 nm elements with an rf field at 8% of the absolute value of H_c.

Once it had been proven that MAMR was feasible experimentally, a recording system that incorporates spin torque oscillators (STO) as the microwave source was proposed by Zhu *et al*. [56, 82]. Numerical simulations indicated that for the most efficient switching process, the rf field must be at least half the anisotropy field of the magnetic material. The initial design considered a linearly-polarized rf field for ease of calculations; however, later studies on the polarization of the rf field showed that a circular polarized rf field is more efficient in switching as it can match its chirality with the precessing magnetization, thus reducing the sensitivity to parameters such as the damping constant [56]. Other approaches to improve MAS efficiency involve tuning the frequency, amplitude, and pulse shape characteristics of the microwave excitation. Okamoto *et al*. [83] studied the feasibility of frequency

modulation of the microwave signal and showed that this technique is favorable for the reduction of the coercive field, but increases the switching time. Wang *et al*. [84] proposed the use of a '*chirped*' microwave signal as the excitation, thus maintaining the system in a resonant condition at all times. The chirp of a pulse is usually understood as the time dependence of its instantaneous frequency, as shown in Fig. 2-9. Specifically, an up-chirp (down-chirp) means that the instantaneous frequency rises (decreases) with time. In microwave applications, this chirp is usually obtained by modulating a high-frequency carrier signal by the RF signal used to generate the AC magnetic field. Simulations reported by Wang *et al.* show that the system is always driven at its dynamic resonance frequency, the overall pumping process is optimal, and that large-angle precession can be excited with the microwave of significantly low power. In light of the above results, the proposal of Zhu *et al*. [82] to use a spin torque oscillator (STO) as the microwave source is very interesting. By controlling the current injected into an STO, the output frequency can be controlled and thus, dynamic resonance can be maintained. However, several factors could affect the operation of such a device, namely strong anisotropy in magnetic materials, dispersion of magnetization in certain film structures, etc. Thus, chirped microwave-assisted reversal presents an avenue for further research studies.

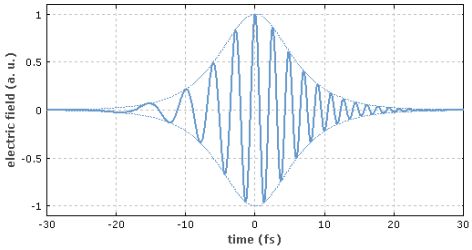

Figure 2-9: A '*chirped*' microwave signal [84].

2.5.3 Current challenges and ideas in MAMR

The practical implementation of MAMR has driven research in this field towards commercial media materials such as CoCrPt-SiO_2 and $L1_0$ FePt. In recent years, MAMR has been carried out on commercial media CoCrPt-SiO_2 of 500 Gb/in^2 [78] and 700 Gb/in^2 [48] areal densities by VNA-FMR spectroscopy [76-78, 80, 81], Hall bar measurements [85] and magnetic force microscopy (MFM) [48, 75] studies. Microwave-assisted switching experiments include both static and dynamic detection techniques. In the static method, the material is switched by an external magnetic field under the influence of a microwave signal followed by an MFM scan to confirm the switch [48]. The confirmation of switching can only be done by comparing the data with an MFM scan of the same area before switching. While this technique is useful for gaining some insight into the required microwave power for reversal, it is too cumbersome and limited to analyze the reversal physics in detail. In the dynamic detection scheme, ferromagnetic resonance measurements are carried out using a vector network analyzer (VNA) [75-78, 80]. The frequency and microwave power from the VNA can be swept, along with the bias field sweep, and an abrupt change in the FMR frequency indicates the switching field. While such a measurement is very simple, the VNA is an expensive tool that is not readily available to all. A third technique to switch higher coercivity FePt is the use of spin waves to assist magnetization reversal, as will be discussed in further detail later in this section. Another key finding was that beyond a certain threshold power, microwave-assisted switching (MAS) occurs for a wide frequency range that is usually centered just below the natural frequency of the material. This

indicates that the MAMR process is yet to be optimized in terms of amplitude levels and frequency characteristics of the microwave signal. Most of the data published has been using coplanar waveguides in contact with the magnetic material, unlike the case in HDDs. Boone *et al*. showed, by Hall measurements, that microwave-assisted switching occurs in granular films at frequencies higher than those predicted by contemporary single-grain models, and this is due to long-wavelength collective spin wave modes that may be assisting the reversal. Efforts to improve the rigor of existing models to predict the microwave-assisted switching process in granular films and exchange-couple composite media are under research currently. Additionally, research on improving the performance of write heads in MAMR devices is also imperative. MAMR write heads are designed to include a spin torque oscillator (STO) as a microwave source in the gap between the write poles. Recording simulation studies using an STO head have reported write field transition lengths reduced to ~5 nm for a write field gradient of 700 Oe/nm using magnetic parameters of commercial media [86], while other studies have reported achievable write field gradients of 1800 Oe/nm and higher [82, 87]. Simulations by Zhu *et al*. [64, 82] and companies such as Western Digital Inc. [88] show that the amplitude response of the STO output is highly influenced by the granular structure of the media material, in addition to the choice of materials used in the fabrication of the STO device. To generate a high intensity, high frequency magnetic field, the saturated magnetic flux density and the thickness of the Field Generating Layer (FGL) in the STO device has to be increased. The magnetic flux density can be increased by incorporating 3d such as Co, Fe and Ni, and adding 5d transition elements to increase the

magnetic anisotropy. However, this causes the damping constant to increase, thereby reducing the intensity of the high frequency magnetic field [89-91]. Thus, materials research is another pressing area in the implementation of STO-based MAMR. As the power requirements of MAMR are currently in the ~mW range, this places a huge demand on high-power STOs which have to date generated a maximum output power of ~0.43 μW [92]. If the necessary power can be generated by synchronizing multiple STOs, then it is important to study the effect of phase distortion in the microwave signals on the reversal process. Recent reports have shown that it is possible to achieve MAS in materials with a microwave excitation below the FMR frequency. Seki *et al*. recently reported the use of spin waves to assist magnetization switching. They study magnetization reversal in a bilayer magnetic film of FePt and Py, where the FePt is engineered to have in-plane magnetization. Perpendicular standing spin waves (PSSW), generated in the Py layer, propagate into the FePt layer and generate magnetization dynamics [93]. This leads to a similar behavior as a MAS process. FePt and other high-K_u materials are known to have f_{FMR} > 10 GHz [48, 93, 94] and exciting a high power microwave excitation at this frequency is impractical. Since spin waves are usually of the order of 10 GHz and higher, this interesting experiment utilized this feature by exciting spin waves in the neighboring soft magnetic layer of the permalloy which behaved in a similar way to an exchange spring in exerting a strong torque on the FePt. This experiment revealed the influence of spin waves on the MAMR technique, a factor that has been largely neglected so far. In fact, spin waves represent a very efficient mode of MAMR as it utilizes features such as the shape and size of the magnetic material and microwave excitation

pulse shapes. This thesis will analyze the contribution of spin waves in greater detail in Chapter 6 where it looks at MAMR experiments in patterned magnetic elements.

2.6 Spin waves

The concept of spin waves was first introduced by Bloch [95] as the lowest-lying magnetic states above ground state in a ferromagnet or antiferromagnets. The spins were considered to be slightly deviated from their equilibrium states and interact with each other akin to a magnetic dipole, giving rise to a magnetization variation that propagates through the magnetic medium as a wave. These waves are mostly created by dipole interactions for a wide range of wave-vectors ($30 < k < 10^6$ cm^{-1}) and hence, are known as magnetostatic spin waves. Depending on the relation between the magnetization and the spin wave propagation direction, there are three types of magnetostatic spin waves. Magnetostatic surface spin waves (MSSW) [96] exist when the saturation magnetization (M_s) is in-plane and is perpendicular to the propagation direction or wave-vector (k). The spin waves are nearly localized to the surfaces of the magnetic medium and hence, are known as surface waves. They were first described by Damon and Eshbach [97-99] and are also called Damon-Eshbach (DE) modes. When the M_s and k are parallel to the plane of the ferromagnetic medium, the spin waves generated are called magnetostatic backward volume mode (MSBV) [100]. The third mode is generated when the M_s is perpendicular to the magnetic film plane and the k-vector as well. This is known as the magnetostatic forward volume mode (MSFV) [101]. These waves are described in Fig. 2-10.

Other than magnetostatic spin waves, there is another class of spin waves known as dipole-exchange spin waves. These spin waves exist when the exchange interaction between spins is the dominant form of interaction over long-range interactions. Exchange interactions usually exist in the short range regime of 4 – 10 nm depending on the magnetic material being considered.

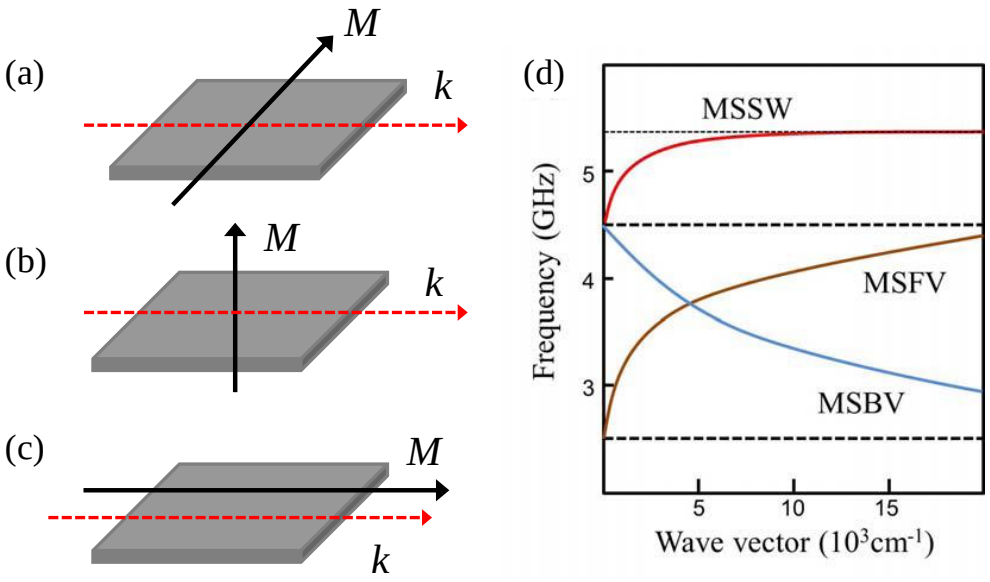

Figure 2-10: Dispersion relation of the three types of spin wave modes and the relation between frequency ranges and their corresponding wave vectors, depending on factors such as material parameters, pattern geometry and film thickness [102, 103].

For an infinitely long thin film, the dispersion relation of the MSSW mode can be given as [104, 105]:

$$f_R = \frac{\gamma_o}{2\pi}\sqrt{\left(H_b + H_k - 4\pi M_s\right)\left\{H_b + H_k - 4\pi M_s + 4\pi M_s\left(1 - e^{-2kd}\right)\right\}} \qquad (2.9)$$

where γ_o is the gyromagnetic ratio, H_b is the external bias field, H_k is the anisotropy field, M_s is the saturation magnetization, k is the wave vector, and d is the film thickness. When ($kd << 1$), the f_R would be the same as that of MSBV ($kd >> 1$) and the FMR frequency.

The dispersion relations of the MSFV mode is approximated as [104, 106]:

$$f_R = \frac{\gamma_o}{2\pi}\sqrt{\left(H_b + H_k - 4\pi M_s\right)\left\{H_b + H_k - 4\pi M_s + 4\pi M_s\left(1 - \frac{1-e^{-kd}}{kd}\right)\right\}} \quad (2.10)$$

An important point to note is the invariance of the dispersion relation with respect to changing the direction of propagation of the MSFV modes. This is because the direction of propagation is always perpendicular to the bias field. Similarly, the dispersion relation for the MSBV modes is given as [104, 106]:

$$f_R = \frac{\gamma_o}{2\pi}\sqrt{\left(H_b + H_k\right)\left\{H_b + H_k + 4\pi M_s\left(\frac{1-e^{-kd}}{kd}\right)\right\}}. \quad (2.11)$$

Spin waves can be considered as the eigenmodes of the magnetization dynamics, and hence provide a picture into the temporal and spatial evolution of magnetization in any magnetic system. One constant during any study of spin waves is that the absolute value of the magnetization remains the same; in other words, the sample temperature is assumed to be well below the Curie temperature of the film. Also, we assume that saturating the film with an external magnetic bias field removes the possibility of any singularities existing within the system such as vortices. In the succeeding chapters, we will demonstrate the detection of spin waves by optical methods and their contributions to MAMR.

2.7 Spin transfer torque (STT) and its applications in HDDs

The giant magnetoresistance (GMR) effect was discovered in 1988 by observing a change in the sheet resistance of a multilayer structure of a ferromagnet/non-magnet in the presence of a magnetic field. The sheet resistance of the multilayer film was shown to change as a dependence on the relative magnetic alignments of the ferromagnetic layers [3, 5]. The current

passing through this structure was spin-polarized and acted as two independent current channels through the materials. Hence, the spin scattering observed by the electrons at the ferromagnet/nonmagnet interface was also unequal and this gave rise to the MR phenomena observed. This is known as the two-current model and was proposed by Sir Neville Mott in 1936 [107].

When the barrier separating the two ferromagnetic materials was replaced by a thin insulating barrier such as AlO_x or MgO, the MR ratio became higher and approached values of 600% [108]. This was a new phenomenon known as the tunnel magnetoresistance effect (TMR) and the principle involved in this case was no longer spin-dependent scattering; rather, it was spin-dependent tunneling (Fig. 2-11). It was postulated, and later confirmed, that the spin-polarized electrons of the majority spin are able to tunnel through the barrier if they possess a certain set of characteristics (Bloch state) as compared to other electrons that do not have these characteristics or belong to the minority spin [109].

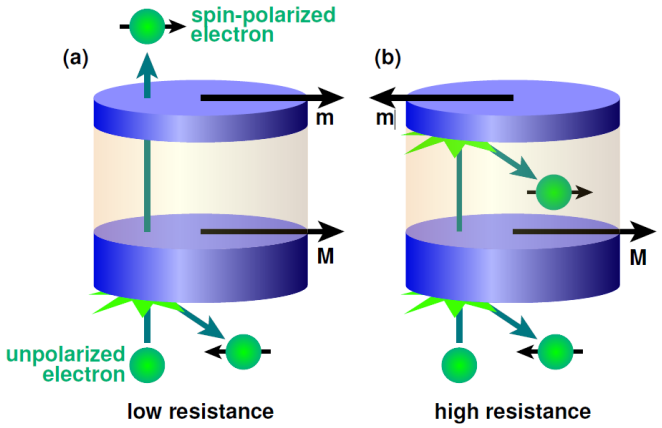

Figure 2-11: Spin-dependent tunneling in magnetic tunnel junctions (MTJ)[110].

Since these initial discoveries, GMR and TMR heads have been incorporated in HDDs as read/write heads and thus were able to increase

capacities by an order of five. However, HDD heads working on these phenomena still required an external magnetic field to cause a switch in the data stored on magnetic bits or to sense the information from a magnetic bit. This proved to be a bottleneck as devices begun to scale down and approached CMOS design limits as they were constrained by the design of the external bias field. In some cases, adjacent bits also underwent data corruption due to the magnetic field being too high. In 1996, Slonczewski and Berger suggested that the magnetization of a material could be switched by merely passing a current through a GMR or TMR multi-layer stack [21, 22]. When unpolarized electrons pass through a magnetic layer, their spins get preferentially aligned in the same direction as the magnetization of that layer (spin polarization). These spin polarized electrons then travel through a thin spacer layer made of a non-magnetic material (metal or insulator) and arrive at the second magnetic layer (shown here as the free layer). At the second magnetic layer, the spins of the electrons exert a torque on the free layer magnetization. As a result of this, the magnetic moment of the free layer begins to tilt and precess. In such a situation, there are two possible outcomes – the magnetic moment of the material either flips [111-113] or precesses at a stable rate about an axis [114-116]. This effect is known as the spin-transfer torque (STT) and is depicted in Fig. 2-12(a).

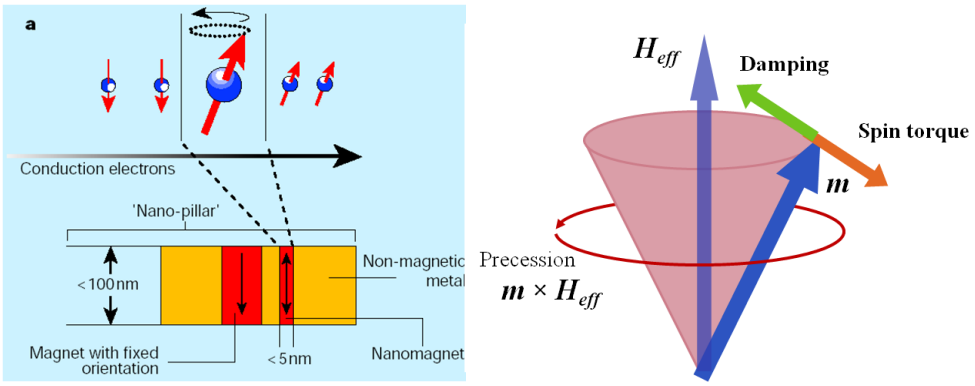

Figure 2-12: (a) STT effect in a nanopillar junction. The trilayer structure considered is a GMR spin-valve structure [117]. (b) Spin transfer torque is opposed by the damping torque that tends to realign the magnetization to its initial state.

The resistance to this reorientation of magnetization due to STT is known as the damping torque, shown in Fig. 2-12(b). Depending on the direction of the current though the multilayer stack, the STT term can overcome, equal or be lesser than the damping. The LLG equation models this situation with the addition of the Slonczewski STT term given as:

$$\frac{d\vec{m}}{dt} = -\gamma(\vec{m} \times \vec{H}_{eff}) + \alpha(\vec{m} \times \frac{d\vec{m}}{dt}) + \frac{\gamma}{M_s V}\vec{m} \times (\vec{m} \times \vec{M})$$

(2.12)

As mentioned above, the relation between the damping torque and the STT torque governs the behavior of an STT device. Thus, we can classify three regimes of operation as shown in Figure 2-13:

(1) When the STT term is less than the damping, the free layer undergoes damped precession before relaxing back to its initial equilibrium state.

(2) When the STT term is greater than the damping, the free layer precesses at larger and larger angles before abruptly reversing magnetization and then relaxing to its final state.

(3) When the STT term is exactly equal to the damping, a steady state is achieved whereby the magnetization continues to precess at a constant frequency and angle of precession for infinite time, producing an oscillating output signal.

The reversal aspect of STT has been considered for applications in the data storage industry as STT-RAM. In this device, the data is stored in MTJs with each MTJ holding one bit of information. Information is written into the MTJs by passing a high enough current (such that current density $J > 10^7$ A/cm^2) to reverse the magnetization in the free layer. A change in magnetization is read as a '1' and no change is read as a '0'.

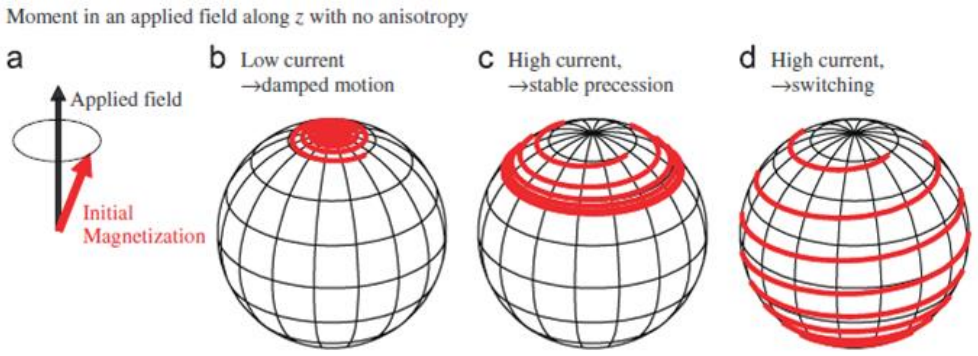

Figure 2-13: (a) – (d) shows the different scenarios possible due to competition between the spin transfer torque and damping torque [118].

The main concern with spin transfer-based switching (STS) is the high current densities required to switch the material. The industry requirement is ~5×10^5 A/cm^2 while the best results achieved until early last year was ~10^6 A/cm^2. Since then, Toshiba have demonstrated a 30 nm diameter MTJ with a critical switching current density (J_c) of 5×10^5 A/cm^2 [119]. The next set of challenges involves deeper materials research to reduce the damping constant of the ferromagnetic electrodes chosen as a lower damping torque aids in

faster STS times. Thadani *et al*. studied the influence of the magnetic field, angle of field, and anisotropic effects in the sample on the switching current density [120]. Recent reports indicate that adding a capping layer of materials such as Ru or Au to the multilayer stack reduces the critical switching current density in exchange-biased nanopillars [121]. This is because the presence of strong spin relaxation in the capping layer increases the spin polarization of the current and also reduces the spin accumulation in the free layers, thereby leading to faster switching. Many different ferromagnetic materials have been studied in the bid to reduce J_c; the most common techniques involve replacing the free layer with materials that have low moment (such as NiFe and CoFeB) or by reducing the thickness of the free layer [122]. A new technique involves replacing the spacer layer by a material such as FeCo which is then oxidized in specific sections (by natural oxidation and ion-assisted oxidation) to form nano-oxide layers (NOLs) [123, 124]. Thus, by limiting the area of the conduction channels through which electrons can move from one FM layer to another, it is possible to increase the current density (J_c) without a corresponding increase in the actual current sourced through the nanopillar. Other studies include thermal-assisted switching of magnetic multilayers [125, 126]. The recent STS demonstration by Toshiba was achieved by the insertion of specular and spin-scattering layers [121, 127], using synthetic antiferromagnets [128] or dual spin valve and dual MTJ structures [129]. In such dual structures, a single free layer is sandwiched between two insulating barriers of different resistances and differing pinned layers on either side of it. Due to a sequential tunneling process and a steady spin relaxation in the free layer, the spin torque efficiency increases significantly, thereby reducing the J_c

for switching. Studies to understand the intrinsic nature of damping in STT-based devices and the strength of the perpendicular component of STT are still ongoing. It was shown by Sankey *et al*. [130] and by Kubota *et al*. [131] that STT is not unidirectional but has an in-plane and a perpendicular component. It is postulated that the perpendicular component plays an important role in reducing the switching current density by as much as 30% [130]; however, the origins of this component are still being debated. Conclusive experimental evidence is still being sought in this area of study.

The second effect of STT which generates steady-state precession has also found applications in the real world, both in HDDs and in replacing conventional CMOS devices. STT in this setting has been used to fabricate spin torque oscillators (STOs), a high frequency microwave source. STOs have found applications as read heads in HDDs [132, 133], microwave sources in MAMR experiments [82], and high frequency sources in CMOS devices [134]. Braganca *et al*. proposed that STOs can serve as efficient read heads using the bit magnetization to alter the effective field contributions [132]. The main challenge in using STOs is its extremely low output powers (< 1 μW). To replace conventional CMOS devices, this barrier has to be crossed before meaningful investment can be done in this field. The highest output power to date from a single nanopillar has been achieved for CoFeB-MgO-based MTJs at ~0.43 μW [92]; however, this was from the non-linear precession regime which makes it more difficult to control. The solution is to phase synchronize several oscillators together to improve the overall output power [135-137]. Current research in STO is mainly focused on improving the power outputs of STOs by a number of methods. In this thesis, the fabrication processes

required to make an STT device are discussed, along with basic electrical characterization techniques such as current-induced magnetization switching (CIMS). In terms of STO applications in MAMR, current research is on improving material parameters in the STO device to generate high-intensity, high frequency magnetic fields as discussed in Section 2.5.3. In addition, a narrow STO device with PMA reference layer and field generating layer (FGL) are indispensable for achieving areal densities greater than 5 Tb/in^2 [138, 139]. Further research on STO devices in MAMR have been mentioned in section 2.5.3.

2.8 Micromagnetics – Behavioral considerations and modelling

In order to understand the processes that affect the equilibrium configuration of magnetization in a ferromagnetic material and how they alter the dynamical response of the system following an external excitation, it is necessary to create a platform that can virtually simulate the said process. Micromagnetic modelling provides this tool to model such non-uniformities on a mesoscopic length scale. It does not describe the behavior of individual magnetic moments; rather, it describes the magnetization dynamics on the whole on sub-micrometre length scales.

At equilibrium, the magnetization is aligned under the influence of an effective field direction, which varies as a function of position. The four main contributions to the effective field are as follows [17]:

1. Externally applied magnetic field

2. Magnetocrystalline anisotropy

3. Micromagnetic exchange interactions

4. Magnetostatic field (including shape anisotropy)

All four terms contribute to raising the free energy (Gibbs energy) of the system. At thermodynamic equilibrium, the total free energy of the system over its entire volume must be zero. However, it is the rate of change of free energy with magnetization that reveals the effective magnetic field.

$$B_{eff}(r) = \mu_o H_{eff}(r) = -\frac{dE}{dM(r)} \tag{2.13}$$

The magnetocrystalline anisotropy energy tends to align the magnetization along certain crystallographic axes. These orientations are referred to as the 'easy axis' of magnetization, while the orientations along which it is difficult to stabilize the magnetization are called the 'hard axis'. The cost of energy to align the magnetization in the hard axis rather than the easy axis is known as the magnetocrystalline anisotropy energy. For uniaxial crystals, the magnetocrystalline anisotropy is given by:

$$\phi_K = K_1 \sin^2\theta + K_2 \sin^4\theta \tag{2.14}$$

where θ is the angle between the easy axis and the magnetization. For a permalloy, K_1 is very small and negative, indicating an easy axis along the [111] direction.

Dipole-dipole interactions in the magnetic material give rise to a stray field within it which opposes the direction of magnetization and is a product of the material itself. This stray field is called the 'demagnetizing field' and the magnetostatic energy density is:

$$\phi_s = \frac{\mu_o}{2} H_d . M_s \tag{2.15}$$

where H_d is the demagnetizing field and M_s is the saturation magnetization. The Zeeman energy contribution is similar to the above form and is given as:

$$\phi_{zeeman} = \mu_o H_{ext} . M_s \tag{2.16}$$

where H_{ext} is the externally applied bias field.

Micromagnetic Simulations

To simulate micromagnetic behavior, a set of partial differential equations are solved repeatedly at every point in the magnetic system. This is done by discretizing the magnetic element into a number of small units in a mesh-like structure. The LLG equation is solved in each cell for the given set of user parameters until convergence is achieved, before moving on to the next set of parameters. These calculations are performed by the micromagnetic package known as the object oriented micromagnetic framework or OOMMF, and do not necessitate any user involvement. The OOMMF solver used in this thesis was for 3D frameworks.

To achieve reasonable accuracy in our simulations, it is important that the right cell size is chosen. When the cell size is comparable to the exchange length, the accuracy is guaranteed. Below the exchange length, all the magnetic moments are precessing in-phase. The exchange length in ferromagnetic materials is defined as:

$$l_{ex} = \sqrt{\frac{2A}{\mu_o M_s^{\,2}}} \tag{2.17}$$

where A is the exchange stiffness constant. In this thesis, OOMMF simulations have been used to model spin wave behavior in patterned magnetic elements with a wavelength greater than 1 μm; hence the minimum cell size chosen is 10 nm.

Chapter 3: Experimental Techniques

This chapter presents an overview of the experimental techniques that have been used in this work. The first section details the thin film growth techniques utilized and the requirements for growing good quality films. The following sections discuss the specific requirements for the preparation of micron-sized MAMR devices and nano-sized STT devices. The patterning procedures, subtractive technique of device fabrication and lift-off concerns are critical for making good quality nano-sized junctions. The final section presents the different characterization techniques used for device and film analysis – micro-structural, chemical, electrical, and optical magnetic characterization techniques.

3.1 Thin film deposition process

3.1.1 Magnetron sputtering

Sputtering is a widely used technique in the industry and academic research circles for film deposition. Sputtered films are known for their excellent conformal deposition, density, purity, and adhesion in magnetic films. The principle of sputtering involves bombarding a target material with accelerated argon ions (Ar^+) which results in atoms being ejected from the target and being deposited on the required sample surface. The source of these can either be the plasma of an inert gas such as argon, or an ion beam. Plasma-based sputtering is more popular and can be controlled by tuning process parameters such as discharge voltage, current and gas pressure. To ignite and sustain a plasma discharge, high working pressure is required. However, high

pressure adversely affects the quality of film deposition as the energy of the sputtered particles is reduced, resulting in poor adhesion and granular nature of films. To overcome this situation, it is necessary to increase the concentration of electrons around the cathode. This is achieved by using a magnetic field around the cathode to trap the electrons in the flux lines, thereby increasing the inert gas ionization at the same generated electron density. The electrons describe a helical path due to the force of the magnetic field and cause an increase in the deposition rate, as compared to diode glow discharge systems. This magnetic field is generated by permanent magnets placed underneath the target, hence the name 'magnetron sputtering'. A schematic of the sputtering system in operation is shown in Fig. 3-1.

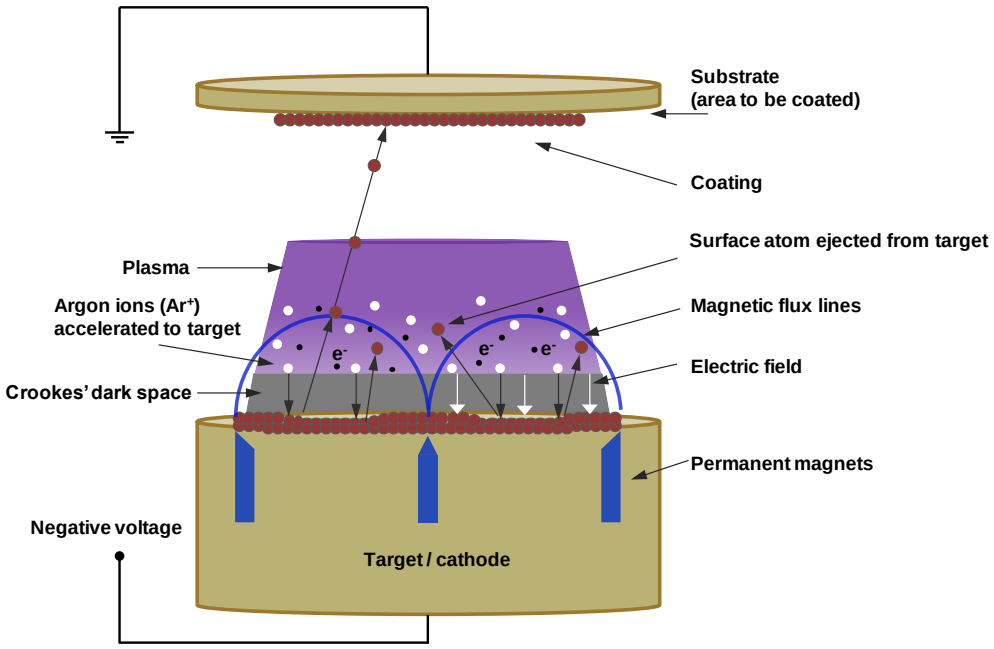

Figure 3-1: Schematic of magnetron sputtering. The material to be coated is directly over the target.

The power supplies used for deposition depend on the type of material being deposited. For metals, a DC power supply is used while insulating materials such as oxides are deposited using an RF power supply. The quality

of the oxide films is very important in both MAMR-based and STT-based devices in this thesis. For the MAMR experiments, the oxide films are used as encapsulation materials to protect the underlying ferromagnetic layer from the current-carrying electrodes and waveguides, which would otherwise cause current shunting effects. In STT devices, the oxide films form the most crucial part of the film stack as the tunnel barrier in the MTJ film. It is not feasible to use a DC power supply for insulators as the continuous build-up of positive charges on the target surface prevents further ion bombardment. A RF power supply resolves this issue due to its oscillating output, but results in an inherently low deposition rate. The deposition rate decreases with an increase in the frequency of the RF source, as well as increasing the magnetic field. A typical value of the RF source's frequency is 13.56 MHz [140, 141].

3.2 Sample preparation and device fabrication for MAMR studies

The samples prepared for studies on MAMR were grown on two kinds of substrates – silicon substrates (700 μm thick) with a 300 nm thick thermally oxidized SiO_2 layer, or a silicon nitride membrane (250 μm thick) thinned down to a 75 nm window in the center of the substrate. Both substrates were diced into 10 mm square samples before proceeding to further fabrication steps, which are discussed in detail below.

(a) Cleaning the substrates

The Si/SiO_2 substrates were passed through several stages of chemical cleaning to ensure a smooth surface for film deposition. They were cleaned in acetone (10 minutes) and isopropanol (10 minutes), with ultrasonication for both processes. The samples were then placed in an ozone stripper (10

minutes) to remove any remaining organic impurities. They were then rinsed in distilled water, followed by nitrogen blow-drying, and finally baked at 100 °C for 15 minutes.

(b) Film deposition

All the samples were prepared by the additive process of device fabrication. Hence, films were deposited by magnetron sputtering after every lithography stage, followed by the lift-off process. The base pressure for deposition was 2×10^{-9} Torr.

(c) Spin-coating and lithography

Photolithography is a micro-fabrication process used to transfer patterns onto a thin film or substrate surface. A light-sensitive material known as photo-resist is applied onto the sample surface by a process known as 'spin-coating' (explained below). UV light (of a certain wavelength) incident on this surface crosslinks areas of the resist surface that are not protected by a mask. The sample is then treated with a chemical developer resulting in the dissolution of the resist surface that is not crosslinked. The pattern is thus transferred to the sample surface as depicted in Fig. 3-2(a). The minimum feature sizes achievable in photolithography are given by the formula:

$$CD = 0.4\left(\frac{\lambda}{NA}\right) \tag{3.1}$$

where CD is the minimum feature size, λ is the wavelength of light used, and NA is the numerical aperture of the lens as seen from the wafer [142]. The photolithography tool used for this research work was a Karl Suss MA6 mask aligner with a light wavelength of 350 nm and a minimum resolution of ~2 μm

(Fig. 3-2(b)). Beneath this value, the diffraction limit sets in, causing poor definition and broadening of features.

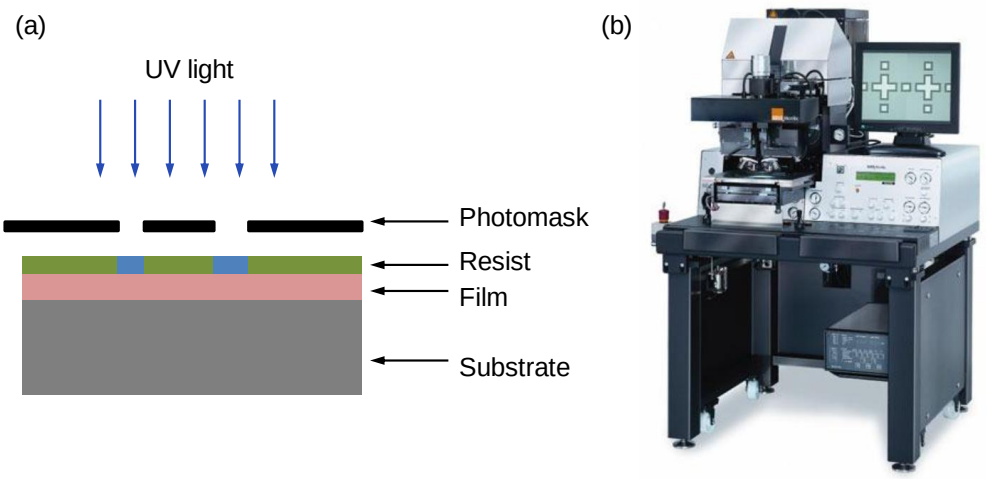

Figure 3-2: (a) Typical photolithography process. The photomask allows selective exposure to UV radiation. The resist is developed for a certain amount of time to create the patterns on the substrate surface. (b) Karl Suss MA6 mask aligner used in this thesis [143].

The electrode definitions, namely waveguides and striplines, were prepared using the 2 μm-thick PFI-D81B8 (from Sumitomo) positive photo-resist. The resist was spin-coated and the samples were exposed for 27 seconds, followed by developing in the AZ300-MIF solution for 25 seconds. The AZ300-MIF is a tetramethylammonium hydroxide (TMAH)-based solution.

In electron-beam lithography (EBL), the process is similar to photolithography, with the major difference being the light source used and the definition of a mask pattern by software. In this case, high energy electrons (10 – 30 keV), focused through a series of electromagnetic lenses, are used to pattern the surface of the resist. Since the electrons have small wavelengths, feature sizes down to ~20 nm can be achieved by choosing the proper resist. The resists used for EBL are known as electron-beam resists. In addition to the choice of resist, the EBL parameters such as electron beam acceleration

voltage (EHT), aperture size and beam dose are equally critical in determining the final feature sizes. The e-beam resist used in the MAMR experiments was positive-tone PMMA 950K (from MicroChem USA) in a 1:1 ratio with the thinning agent Anisole, at a thickness of 120 nm. The dose was optimized for different experimental designs, and the developing was carried out in a solution of MIBK:IPA (3:1) for 45 seconds.

The spin-coater used in this work was a Spin150-NPP model from SPS-Europe. The sample to be spin-coated is fixed on the holder in the coater by means of vacuum suction. The resist, in the form of a viscous solution, is dropped on the sample using a pipette. The appropriate amount of resist is ~2-3 ml. The spin speed used for the PFI and PMMA 950K resists was 6000 rpm for 45 seconds. Following this, the samples are usually pre-baked at a temperature specified by the resist data sheet. PFI was pre-baked for 90 seconds at 90 °C, while PMMA950K was pre-baked at 180 °C for two minutes.

(d) Dry etching (ion milling)

The process of dry etching using an Ar-based ion miller is similar to the sputtering process. In this case, the Ar^+ ions are used to bombard the sample directly and to etch or remove materials from its surface. The sample is usually patterned before proceeding to ion milling so as to selectively etch the material to define micro- or nano-sized mesa structures. As most resists are etch-resistant to Ar^+ ions, the etch selectivity is determined by other parameters such as thickness and thermal dissipation of the resist. Etching parameters such as uniformity can be ensured by rotating the substrate holder, which will also result in vertical side-wall features in the mesa. To account for

the excess buildup of positively charged Ar^+ ions, a neutralization filament is present near the work plate [141].

The power of the ion beam controls the etch rate and in this study, the samples were etched at a power of ~38 W (beam voltage = 300 V, acceleration voltage = -45 V, beam current = 110 mA). The etch rates of all the materials used in this study were calibrated apriori using an external KLA Tencor profiler and an in-built HIDEN secondary ion mass spectrometer (SIMS) with an end-point detector. Thus, it was also possible to determine the etch-stop point during the etching process. Figure 3-3 shows the schematic workflow of a sample coated with positive resist, followed by patterning, ion milling etching and finally, lift-off in acetone.

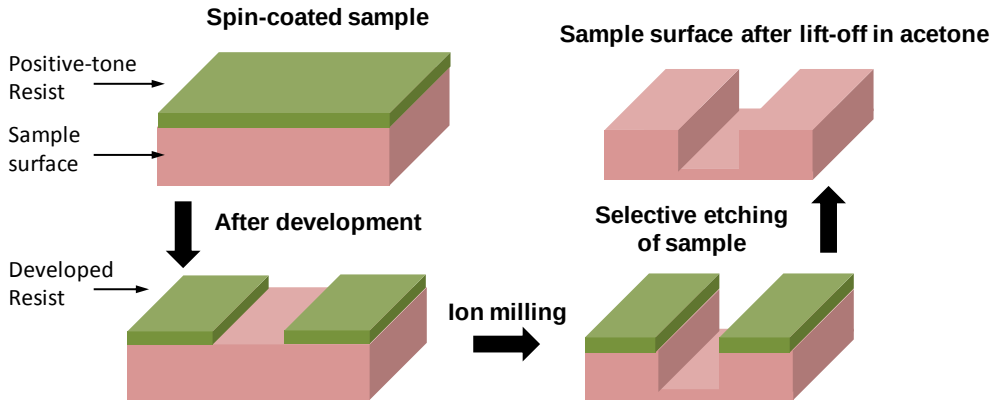

Figure 3-3: Schematic of a positive resist-patterned sample etched by ion milling.

(e) Lift-off process

Resist removal after deposition or ion milling was conducted by submerging the sample in acetone and providing agitation by low power ultrasonication. This caused the resist surface or overlying film surface to develop cracks or fissures which further disintegrated to leave behind the designed features. No ultrasonic was used for the samples prepared on the SiN_x membranes. The samples were placed at a tilted angle in a homemade

plastic container such that the window was never in contact with any surface. Agitation was provided by manually circulating the liquid through a pipette.

3.3 Sample preparation and device fabrication for STT studies

The samples prepared for the study of STT-based devices differed from the MAMR-based devices in terms of growth techniques, resists and associated chemicals used. The STT devices were fabricated by a subtractive process. In other words, a multi-layer film stack was deposited first, followed by lithography, ion milling and lift-off steps in that order. The fabrication work flow is detailed below:

(a) Cleaning of substrates

The 10 mm square substrates (700 μm thick) with a 300 nm thick thermally oxidized SiO_2 layer were cleaned in a similar manner as that described in the previous section.

(b) Film deposition

A multi-layer film stack as shown in Fig. 3-4 was deposited in the magnetron sputtering chamber at a base pressure of 2×10^{-9} Torr. The metallic layers were deposited by DC sputtering, while the oxide layer was deposited by RF sputtering. Prior to deposition, the substrate surface was cleaned by substrate bias (RF power supply) for two minutes at 50 W and 3 mT process pressure.

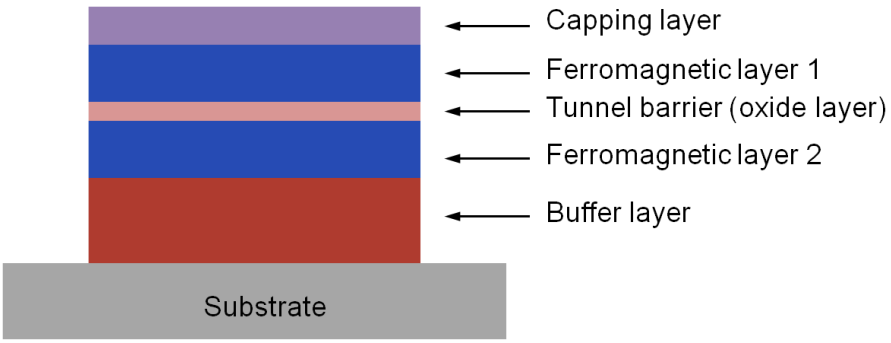

Figure 3-4: Schematic of a multi-layer film stack for nano-sized MTJ junctions.

(c) Spin-coating and lithography

The devices made for the study of STT was of the current perpendicular-to-plane (CPP) geometry. This required the formation of a micron-sized bottom electrode, followed by the creation of a nano-sized MTJ junction on its surface, encapsulation by an oxide layer to prevent shorting across the tunnel barrier and, finally, the creation of top electrodes. The bottom and top electrodes were defined by photolithography using the maN-2405 negative-tone resist and the PFI positive-tone resist, respectively. The bottom electrode mesa was patterned and etched in the first step, so as to isolate devices on the 1 cm × 1 cm sample. The nanopillar fabrication steps were subsequently carried out on the bottom electrode mesas. The nanopillar fabrication was done using three different resists: ma-N 2401, ma-N 2405, and HSQ/PMMA 950K (1:1) bilayer resist. Each was different in its thickness and organic composition, which gave rise to different properties of thermal degradation, minimum resolution, and resist uniformity. The process parameters for all the resists are given at the end of this section. The results of the process parameter optimization in EBL for each resist are shown below in Figs. 3-5, 3-6, and 3-7.

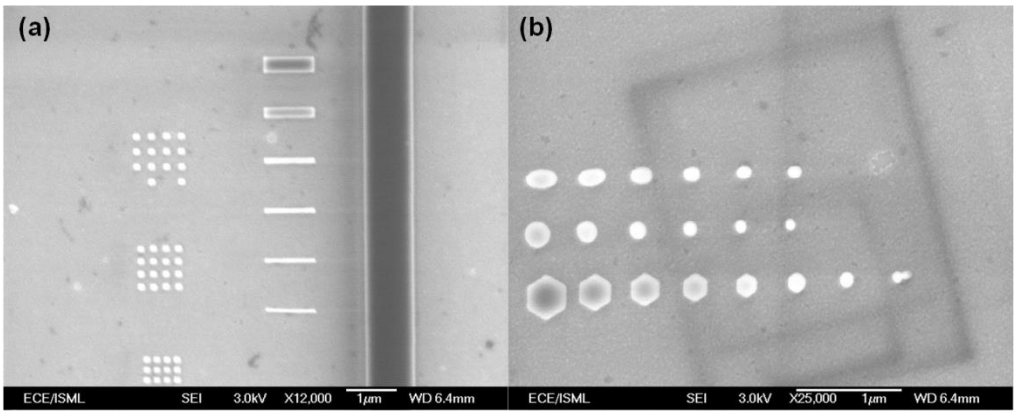

Figure 3-5: SEM top view of device pillars made with ma-N 2401 (with different shapes, sizes and aspect ratios). Minimum feature size achievable was ~40 nm.

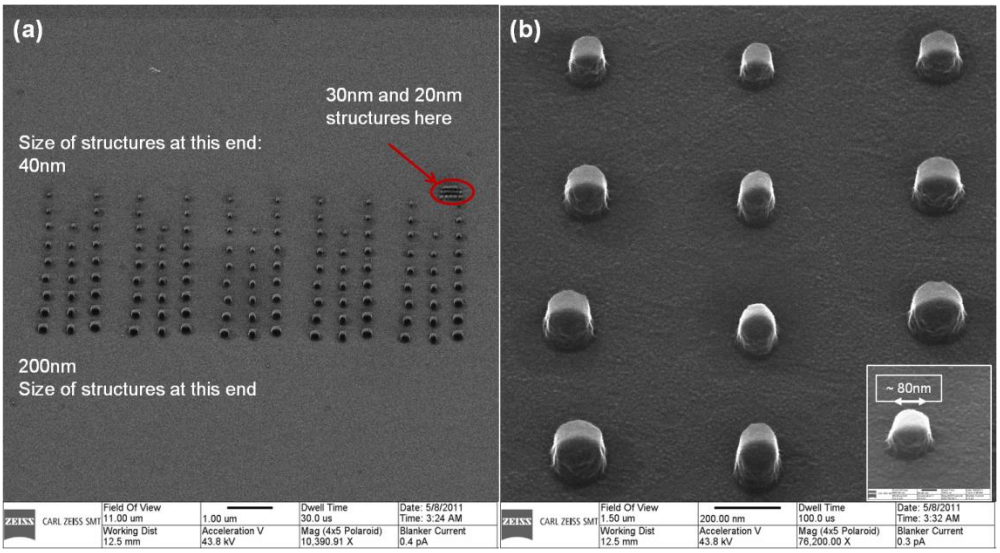

Figure 3-6: SEM top view of device pillars made with ma-N 2405 (with different shapes, sizes and aspect ratios). Minimum feature size achievable was ~60 nm.

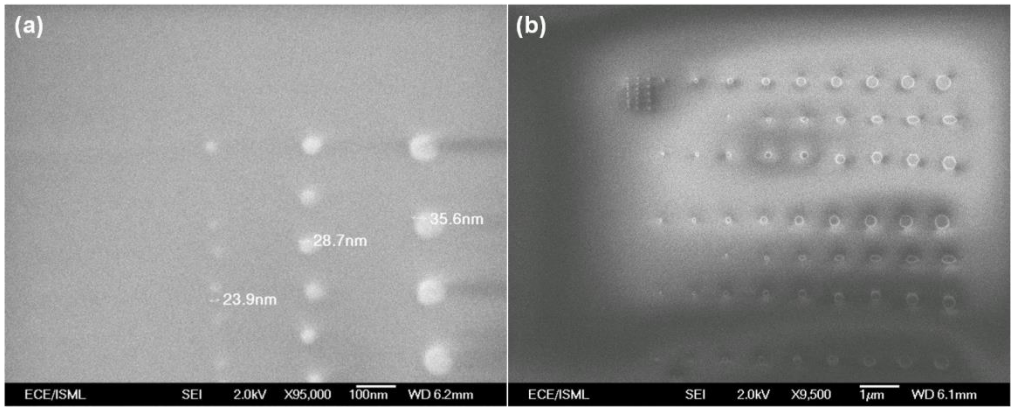

Figure 3-7: SEM top view of device pillars made with HSQ/PMMA 950K (1:1) bilayer (with different shapes, sizes and aspect ratios). Minimum feature size achievable was ~28 nm.

(d) Dry etching (Ion milling and RIE etching)

As explained in the previous section, the samples patterned with the ma-N series of resists were etched by the ion milling technique. It was noticed that the etching conditions corresponding to a power of 38 W caused the substrate to heat up (even with backside water cooling), resulting in burning of the resist for nano-sized features. To overcome this problem, the ion beam power was reduced to ~10 W and the etching process was stepped in shorter durations to allow the substrate to cool down. The etching angle was crucial in developing a good etch profile and preventing the formation of side-walls by metal redeposition.

For the bottom electrode pad, ma-N 2405 was used and etched down to the Ta buffer layer. The etch rate was calibrated using the SIMS and it was estimated to take three minutes to reach the etch stop point. Due to the large feature size of the pad, there was no resist burning and hence, no necessity to run the etching process in a stepped fashion. For the nanopillars, the etching process was run in a stepped fashion at two rotation angles of the substrate holder to create a vertical side-wall profile and to avoid shorting across the tunnel barrier due to the redeposition of etched metal atoms. Each etching step was run for 15 seconds followed by a two minute cooling time, and the process was repeated until the etch stop point was reached. As a result of the short etching duration, the SIMS detector was not strong enough to detect any elemental signal and as a workaround, the etch stop time was calculated using the etch rates of the individual materials. A buffer time of 20 seconds was added to the total calculated time to account for the changes in process conditions in the intermediate stages. The etching angles used were along the

film normal till the etch stop point was reached, followed by a glancing angle etching step (70° to the film normal) for 20 seconds to clean the sidewalls of any redeposited metal atoms. Care must be taken to avoid overmilling the nanopillar junctions, as this can lead to magnetostatic coupling effects between the free and fixed layers across the tunnel barrier.

For the samples prepared with the HSQ-PMMA bilayer resist, the pattern transfer from HSQ to PMMA was performed by RIE etching with O_2 [144]. The gas pressures and flow rates were calibrated to stop the etching at the cap layer of the film stack, following which the sample was subjected to ion milling (explained above) to create sharp nanopillar junctions. The etching time was ~7 minutes at a flow rate of 30 sccm. However, this process was found to degrade the feature definitions and cause expansion, probably due to an insufficient curing process of the underlying PMMA layer and long pre-baking times for the underlayer, amongst others. Thus, the HSQ-PMMA bilayer resist was discarded for future device fabrication.

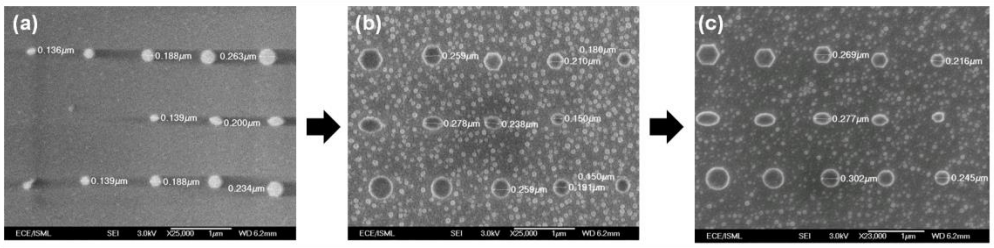

Figure 3-8: Increment of feature sizes during subsequent steps of device fabrication with HSQ/PMMA bilayer resist.

(e) Oxide encapsulation

The oxide encapsulation step ensures that the tunnel barrier is electrically protected from the subsequent step of top electrode definition. Hence, the thickness of the encapsulation must be high enough to electrically isolate the junction, but also thin enough to allow easy lift-off of the resists. As shown in

the schematic workflow in Fig. 3-9, the lift-off reagent, such as Acetone or PG remove (from MicroChem, USA), has to seep through the SiO_2 encapsulation layer to attack the ma-N 2405 resist. A thick oxide layer would make it difficult to access the resist, and hence prevent successful lift-off. In this study, the nanopillar thickness was 18 nm, and the oxide layer deposited was 10 nm above the pillar height, i.e. 28 nm.

The entire workflow for the preparation of an STT device is shown below in Fig. 3-9. An overview of the processing conditions of the different resists (EBL and photolithography) used in this work is summarized in Table 3-1.

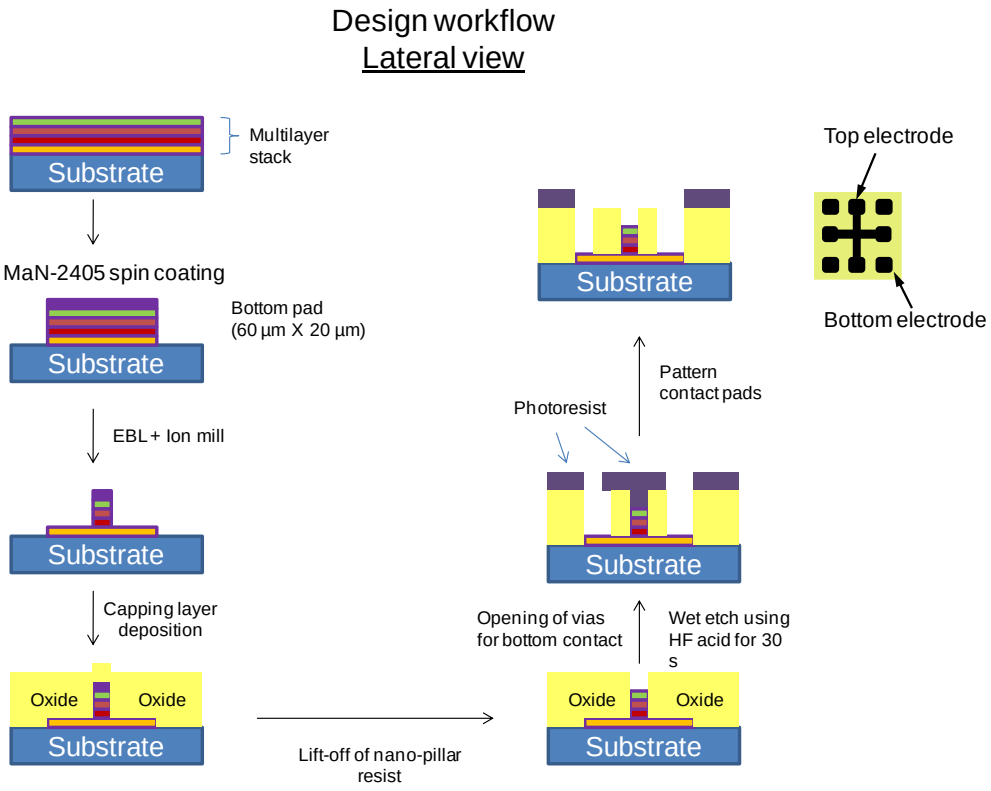

Figure 3-9: Lateral view of a CPP device fabrication process. The final image on the top right corner is a top view of the same sample. The top and bottom electrodes are connected through the nanopillar junction.

Resist	ma-N 2401	ma-N 2405	HSQ/ PMMA950K (1:1)	PFI-D81-B8	PMMA 950K (1:1)
Dilutant	-	-	Anisole	-	Anisole
Nominal thickness (nm)	100	500	175	2000	120
Pre-bake temperature (hot plate)	90 °C	90 °C	150 °C for HSQ, 180 °C for PMMA	90 °C	180 °C
Pre-bake time	90 s	90 s	120 s for HSQ, 120 s for PMMA	90 s	120 s
Spin speed (rpm)	6000	6000	6000	6000	2500
Spin coating time (seconds)	45 s				
Exposure time (photolithography)	-	25 s	-	14 s	-
Exposure dose (EBL resists)	180 $\mu C/cm^2$	250 $\mu C/cm^2$	500 $\mu C/cm^2$	-	180 $\mu C/cm^2$
Developer	AZ300-MIF		NaoH: NaCl developer	AZ300-MIF	MIBK:IPA (3:1)
Development time (seconds)	-	27 s	-	21 s	-
Rinsing agent	DI water				IPA
Removal agent	Acetone, ma-R 404		Acetone		

Table 3-1: Processing parameters of the different resists used in this work.

3.3.1 Preparation of films for STT device fabrication

MTJs with a film composition of Ta (5)/Ru (20)/Ta (5)/$Co_{60}Fe_{20}B_{20}$ (6)/MgO (1)/$Co_{60}Fe_{20}B_{20}$ (4)/Ta (5)/Ru (5) (all nominal thicknesses in nm) were grown by magnetron sputtering in an ultra-high vacuum chamber at a base pressure of 2×10^{-9} Torr. The composition for this film stack was chosen to be the same as that used by Ikeda *et al*. [108], who reported the maximum value of TMR measured at room temperature at 604%. The samples were annealed at 300 °C for 30 minutes in a magnetic field of 200 Oe. The films were subsequently fabricated into nano-sized pillar junctions by a combination of electron beam lithography (EBL) and Ar ion-milling processes for measurement in a current perpendicular-to-plane (CPP) configuration.

3.3.2 Roughness measurements of the underlayers

Improper device fabrication procedures for nanopillar MTJ device can result in the observation of a number of coupling mechanisms across the tunnel barrier, including magnetostatic coupling, domain wall coupling and Neel ("orange peel") coupling. The former two effects may arise at the pillar

etching stage of the device fabrication as a result of overmilling, while the latter occurs due to roughness of the buffer layers propagating upwards through the multilayer stack. Optimization of the etching procedures can minimize the magnetostatic coupling effects, while improving the roughness of the underlayers can minimize Neel coupling. In this study, AFM-based analysis was carried out to characterize the roughness of the sputtered underlayer films. Table 3-2 below shows the different combinations of buffer layer compositions tested to determine an optimum composition for the final device stack.

Ta (10 nm)/ Cu (20 nm)	1.120 nm
Ta (10 nm)/ Cu (20 nm)/ Ta (10 nm)/ Cu (40 nm)	1.979 nm
Ta (4 nm)/ Ru (2 nm)/ Ta (4 nm)	0.965 nm
Ta (10 nm)/ Ru (5 nm)/ Ta (10 nm)	0.603 nm
Ta (5 nm)/ Ru (20 nm)/ Ta (5 nm)	0.210 nm

Table 3-2: RMS roughness of the different underlayer compositions measured using AFM.

3.3.3 TEM of MgO-based MTJs

The AFM and profilometer are used to characterize initial roughness and to assess accurate deposition rates of different materials. Thermally-oxidized Si substrates (300 nm of SiO_2 on top) were patterned by photolithography using positive-tone resists, followed by the sputtering of the material being investigated. The patterned and deposited sample is then submerged in acetone to remove the resist layer, leaving behind a patterned stack of the material being investigated. The height of this stack can be measured using an AFM or a profilometer. From simple calculations of

deposited material thickness over the deposition time, we can estimate the deposition rate accurately. In addition, cross-sectional TEM analysis provides valuable information on the crystalline quality of the MTJ film stack – a key criterion for obtaining high TMR. As the MgO barrier is quite thin compared to the requirements for micron-sized junctions, the possibility of inter-layer diffusion at the ferromagnet/insulator/ferromagnet sandwich structure is of prime concern in fabricating successful nano-sized junctions. TEM analysis has been carried out for the film stacks before annealing and fabricating CPP junctions.

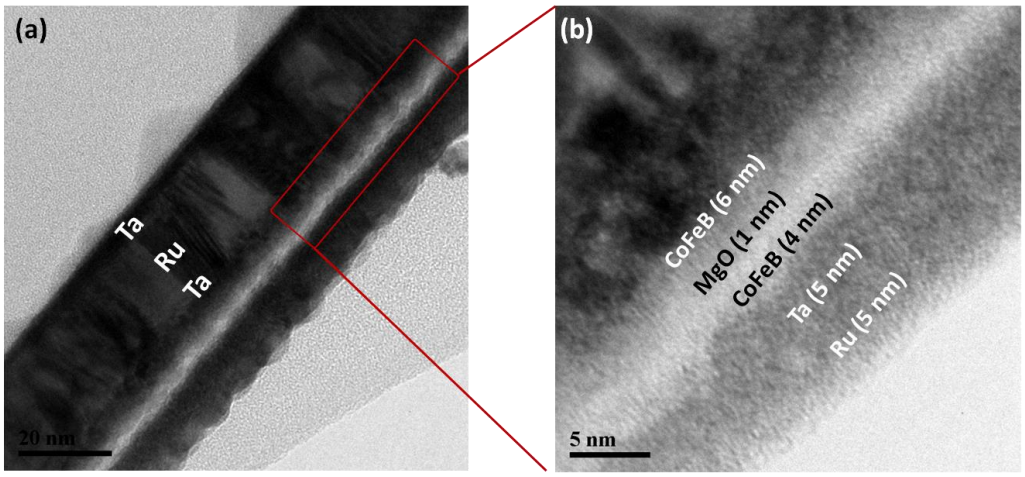

Figure 3-10: (a) Cross-section TEM micrographs of MTJ films before annealing. (b) TEM of the trilayer structure of the film stack. There is no visible crystalline order in the CoFeB layers as expected, but the roughness in the free layer is quite significant.

Figure 3-10 shows the TEM results for MTJ films before annealing. We observed roughness at the upper CoFeB/Ta interface indicating the possibility of interdiffusion of the Ta into the CoFeB electrodes, and that of B into the Ta layers, as previously reported [108]. This shows that the annealing conditions for the 2 nm thick-MgO barrier are not suitable for extremely thin MgO barriers (~1 nm), and it is necessary to optimize the annealing conditions more

carefully. Nevertheless, we proceeded with fabricating nanopillar MTJs for electrical characterization.

3.4 DC characterization of nanopillar MTJ junctions

The films were patterned into nanopillar devices of two size ratios, namely 200 nm × 120 nm and 180 nm × 90 nm. TMR measurements were carried out in a four-point probe station before annealing. We observe irregular MR loops in one junction as shown in Fig. 3-11 (a,b) which suggest that the nanopillar junction may have been formed in a region of significant interdiffusion between the CoFeB and MgO layers. This is seen in the strong coupling between the free and fixed layers, which switch together under the effect of the magnetic field. Figures (c-f) show a more conventional MR loop shape and exhibit two distinct resistance states. However, the R.A product fluctuates from very low (~0.258 $\Omega\cdot\mu m^2$) to moderate values (627.372 $\Omega\cdot\mu m^2$) for a low TMR of 2 -6 %. This can be attributed to the presence of a diffused MgO barrier with several vacancies contributing to the conductive behaviour. Thus, while the inter-layer coupling has been minimized, the effects of diffusion are clearly seen in the MR loop behavior. Redeposition-induced shunting of the junctions, during the nanopillar etching stage, can be responsible for the low junction resistances observed. Thus, it is necessary to optimize the etching angles in the ion milling process to minimize the possibility of shunting.

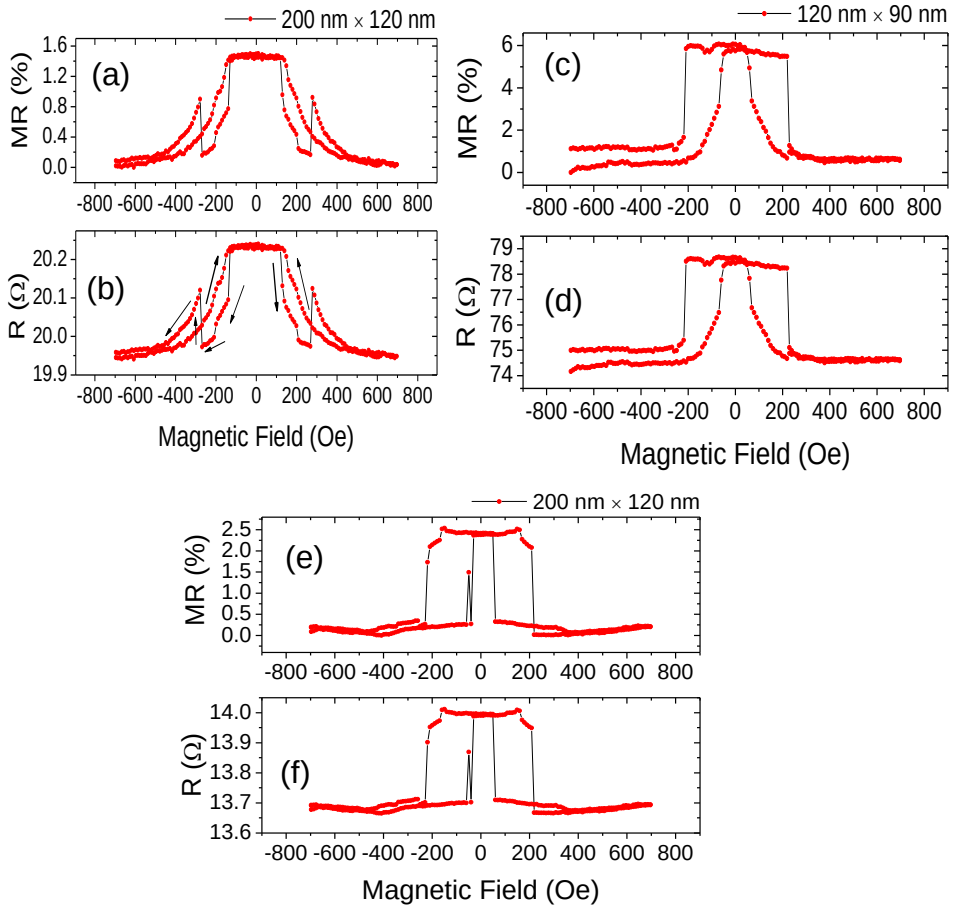

Figure 3-11: (a-f) TMR and junction resistance plots of different nanopillar junctions.

3.4.1 Current-induced magnetization switching in low RA product MTJs

Due to the effects of diffusion in our nanopillar MTJs, a possible conducting path through the MTJ tunnel barrier may lower the effect of STT. Hence, we decided to test our higher resistance devices to observe any signature of STT. In our device design, the top electrodes were connected to the free layer and the bottom electrodes to the fixed layer. The bottom and top electrodes were connected to the negative and positive terminals of the current source, respectively. This implies that a positive current is required to switch from the anti-parallel to parallel state (AP $\rightarrow$P), and a negative current to

switch from the parallel to anti-parallel state (P →AP). The current flowing through the device was swept and the voltage was measured continuously. While there would be effects of Joule heating in the measured signal level, the clear switching loop, seen in Fig. 3-12, under the influence of a DC current confirmed the presence of spin transfer torque (STT),. The switching current densities were calculated to be J_c (AP →P) = 1.592 × 10^7 A/cm^2 and J_c (AP →P) = 8.49 × 10^6 A/cm^2.

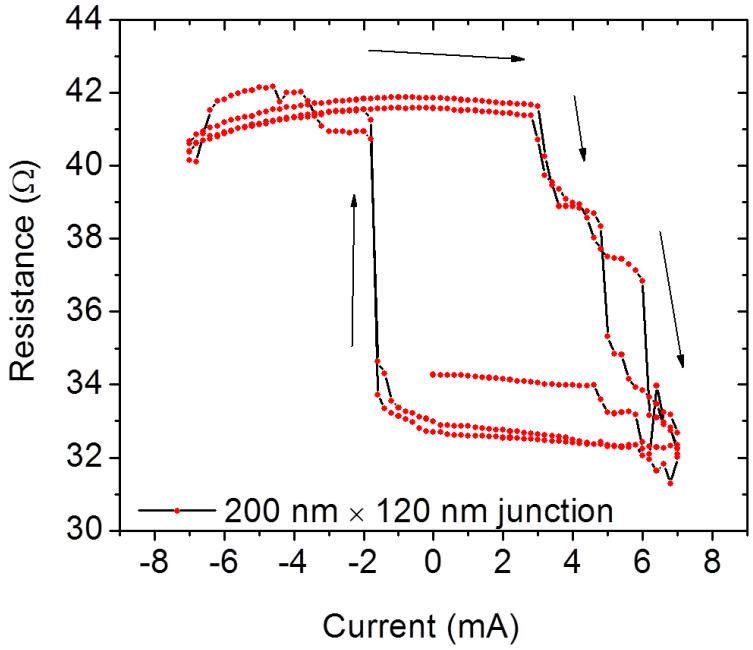

Figure 3-12: Current-induced switching in pseudo spin-valve MTJ junctions of CoFeB/MgO/CoFeB. The device was measured for two loops to confirm the effect of STT.

3.4.2 Future improvements for device fabrications and conclusions

To make high quality nanopillar MTJ junctions, it is important to resolve the diffusion issue at the ferromagnet/tunnel barrier interface. Careful optimization of the annealing temperatures and rigorous TEM analysis are required to determine the most effective process conditions for STT-based devices.

In conclusion, we have shown the capability of fabricating devices that show clear evidence of spin transfer torque in current-induced switching measurements. However, the RA product of the device is lower than the expected values in a similar range, and the quality of the devices is compromised by the interdiffusion at the interface between the ferromagnetic layers and the tunnel barrier. Careful optimization of the growth and process conditions is required to overcome the diffusion issues.

3.5 Characterization techniques

3.5.1 Scanning transmission X-ray microscopy (STXM)

A number of different high resolution magnetic imaging techniques exist today, each with its advantages and disadvantages. Techniques such as magnetic force microscopy (MFM), scanning electron microscopy with polarization analysis (SEMPA) and scanning tunneling microscopy (STM) provide information about the static magnetic configurations, but not dynamic information. On the other hand, techniques such as optical Kerr microscopy (MOKE) with femtosecond lasers can provide dynamic magnetic information down to a temporal resolution of several tens of femtoseconds. The downside of these techniques, however, is their poor spatial resolution which makes it difficult to image structures such as domain walls and spin waves. Further detailed information on these techniques can be found elsewhere [145].

In this work, we used time-resolved scanning transmission X-ray microscopy (STXM), a technique with high spatial and temporal resolution. The technique of X-ray magnetic circular dichroism (XMCD) was used in conjunction with STXM to improve the magnetic contrast of the images, and

this requires the use of circularly-polarized X-rays with wavelengths in the range of 1-2 nm. By exploiting the pulsed nature of synchrotron light and the rastering nature of the STXM technique, fast photon counting is possible and this allows us to use the full capacity of the light for time-resolved measurements. A requirement of the STXM technique is circularly polarized soft X-rays, which are only available in synchrotron facilities. The work presented in this thesis was carried out at the MAXYMUS microscope at the BESSY II synchrotron in Berlin, Germany. At BESSY II, the electron bunches are accelerated up to 1.7 GeV and injected into the storage ring, which has a 240 m circumference. Up to 400 separate electron bunches travel on this ring, with a 2 ns temporal separation between them, as shown below. Each electron bunch is 30 ps long and this determines the ultimate temporal resolution of STXM.

In modern synchrotron facilities, undulators are used to generate monochromatic circular polarized X-rays. These undulators consist of a periodic arrangement of NdFeB magnets that create a circular and periodically alternating magnetic field. Electrons travel on spiraling paths through such a field, causing them to emit circularly polarized light. The periodic arrangement creates a constructive interference mechanism, leading to high light brilliance (photon flux per unit solid angle at certain energy). The field strength and position of the magnetic arrays can be tuned to control the energy of the circulating electrons and the polarization of light. The light is then focused by a mirror collimator onto a plane grating monochromator (PGM) such that the energy of the light can be set by the relative position of the grating with respect to the exit pinhole. The pinhole also serves as a point light

source to illuminate the zone plate lens with spatially coherent light [146]. In STXM, the monochromatic light is shone on a combination of the Fresnel zone plate and order selecting aperture (OSA). The centre stop of the zone plate absorbs the zero order diffracted light, while the OSA absorbs diffracted light higher than the second order. The Fresnel zone plate consists of a series of concentric rings very close to each other (nowadays, as close as 12 nm), which are used to make the spatially coherent light interfere constructively at a central spot. The size of the pinhole around this spot determines the light intensity and its spatial coherence. Figure 3-13 shows a schematic view of the STXM setup available at the BESSY II synchrotron, which was used for the time-resolved experiments of MAMR in patterned elements.

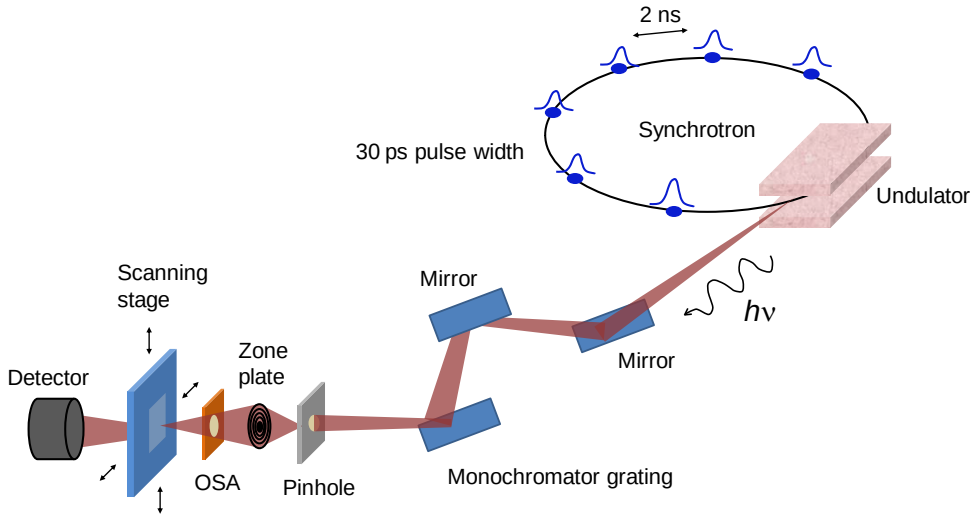

Figure 3-13: Optical components of the beamline at MAXYMUS. The energy range of the circularly polarized electrons is between 700 – 900 eV. The monochromatic beam is focused on a 20 μm-wide pinhole to generate energy-specific and spatially coherent X-rays to illuminate the zone plate lens. The final spot size of the light on the scanning stage is ~25 nm (adapted from [146]).

X-ray magnetic circular dichroism

The XMCD effect is a difference spectrum of two X-ray absorption spectra taken in a magnetic field – one with left circularly polarized light and the other with right circularly polarized light. The difference between the two provides information about the magnetic properties of the atom, such as spin and orbital magnetic moment. Thus, the chirality of the light triggers different energy transitions within the magnetic atom. By choosing an appropriate energy level for the light photons, it is possible to selectively detect the magnetic state of a particular element in the sample under consideration. Figure 3-14 shows the extraction of the XMCD signal from the X-ray absorption spectra of the left circularly polarized and right circularly polarized light. This technique was pioneered by G. Schutz *et al*. [147], who measured the effect in iron (Fe) at the *K*-absorption edge. In this work, our magnetic material under consideration was permalloy and the data was recorded at the L_3 absorption edge of Ni atom (852.7eV).

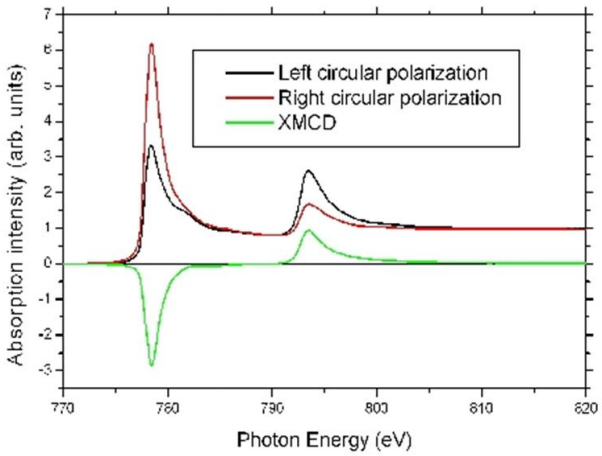

Figure 3-14: Sample data obtained in measurements using the XMCD technique [145].

Pump-and-probe technique

The pump-and-probe technique is a method in which the magnetic structures are excited repetitively with a periodic signal and the configuration change(s) is imaged stroboscopically with rapid photon flashes. This is because of the technical setup of the electron bunches at BESSY II. For practical reasons, not all the electron buckets or pulses (see Figure 3-13) are filled with electrons and their intensities may vary. The most intense electron bunch in the multi-bunch operation is called the camshaft bunch, followed by 50 empty electron buckets. By tuning the frequency of the excitation signal to be synchronized with the 500 MHz clock signal of the synchrotron facility, it is possible to measure the same changes in magnetic contrast millions of times. The microscope detector used is an avalanche photo-diode (APD) detector which allows for single photon counting, and the synchronization of the detection electronics allows the allocation of each photon to individual detection channels. Thus, the total sampling time in this technique is given by:

$$\Delta t = \frac{T_c}{N} \tag{3.2}$$

where Δt is the sampling time, T_c is the period of the excitation signal, and N is the number of counting or detection channels. Further information about the pump-probe techniques used at BESSY II can be found elsewhere [146].

3.5.2 Time-resolved magneto-optic Kerr effect (TR-MOKE)

The magneto-optic Kerr effect is a technique that studies the change in polarization of light reflected off a magnetic surface. The change in the light property, more specifically defined as the rotation of the light signal in the polarization plane, gives information about the magnetic state of the material

under consideration. The Kerr angle (ϕ_K) is a complex summation of the Kerr rotation θ_K and the Kerr ellipticity ε_K.

$$\phi_K = \theta_K + i\varepsilon_K \tag{3.3}$$

The interaction of the magnetic sample with the electromagnetic field is given by the dielectric tensor (DK, ε') as:

$$\phi_K = \theta_K + i\varepsilon_K = \frac{i\varepsilon'_{xy}}{\sqrt{\varepsilon'_{xx}\left(1-\varepsilon'_{xx}\right)}} \tag{3.4}$$

ε' has components along the diagonal and off-diagonal directions. The off-diagonal elements are linearly dependent on the magnetization and are responsible for the magnetic signal. The diagonal elements give a measure of the optical reflectivity [148]. Depending on the relative orientation of the magnetic moment of the sample and the wave-vector (k) of the incident laser, the MOKE setup can be classified into three categories which are depicted in Fig. 3-15.

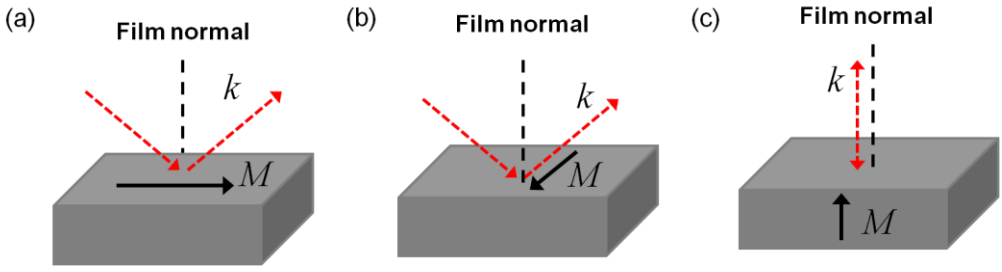

Figure 3-15: Schematic of the various configurations for the MOKE effect: (a) the longitudinal MOKE, (b) the transverse MOKE, and (c) the polar MOKE configurations.

In a time-resolved MOKE setup as illustrated in Fig. 3-16, the pump-and-probe technique is used to access the time-varying magnetization of a magnetic sample. In our experiments, a strong current pulse (10 V) is passed through a linear current-carrying stripline ('pump') to disturb the magnetic

state of the sample, and a picosecond laser pulse (625 μW) is used to measure the change in the magnetization ('probe'). A photo-detector at the end of the setup converts the light information into a time-varying electrical voltage measured by a lock-in amplifier. As in the case of STXM, the current pulse and the lock-in amplifier are triggered at a frequency of 100 kHz while the laser is triggered at 200 kHz. This is done to remove the sinusoidal background noise in the measured signal due to the lock-in reference signal. Thus, every data point is averaged over several cycles of the same magnetodynamics.

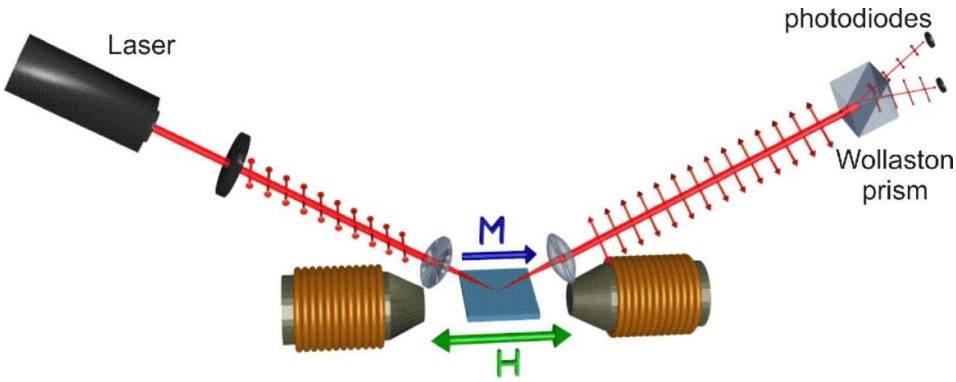

Figure 3-16: A typical MOKE setup used for both static and time-resolved experiments. The difference between the two lies in the measurement cycles (adapted from [149]).

3.5.3 Scanning Probe Microscope (SPM)

The scanning probe microscope was used in this work to characterize the STT device fabrication process. The system used was the Digital Instruments Nanoscope III (DI-3100) multimode SPM system (Figure 3-17). The main requirements were to measure the resist thickness before and after the etching process and characterize the surface roughness of the thin films grown using an atomic force microscope (AFM). For the STT samples, it is

very important to have smooth underlayer surfaces so as to prevent Neel coupling at the tunnel barrier. The AFM was used in the tapping mode in this system. A piezo-stack was used to excite the cantilever stack causing the tip to oscillate. When the tip approaches the surface of the material, van der Waals' forces cause the tip to deflect back. The deflection causes a change in the position of the reflected laser light on the photodetector array, which is converted to an electrical signal giving vertical height information about the sample [150].

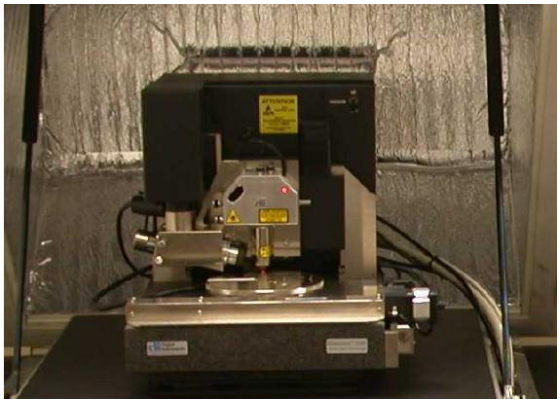

Figure 3-17: The AFM used in this work. The system is shielded from outside noise.

3.5.4 Scanning Electron Microscope (SEM)

The SEM system used in this work was a JEOL JSM 6700F system. The SEM was used at the primary step of the STT device nanofabrication process. Dose optimization of the structures fabricated by EBL was done through imaging using the SEM. To avoid charging effects in insulating materials such as resists, a thin metallic layer such as Au (2 nm) was coated on top of the sample. The SEM utilizes the small wavelengths of accelerated electrons to resolve features down to the nm scale. A sample bombarded by accelerated electrons releases secondary electrons which are collected to retrieve information about the topography and morphology of the sample

[148]. High-end SEM systems also receive signals from transmitted electrons, Auger electrons, X-rays and cathodoluminescence to reveal further information about the composition and crystallography of the sample.

3.5.5 Transmission Electron Microscope (TEM)

The TEM is a high-resolution microscope that is used to characterize the structural properties of a sample. By presenting high-resolved cross-sectional images of the film stack and diffraction patterns of the same, it is possible to extract information about the crystallographic orientation and interfacial microstructure of the grown films. Thus, our requirement to achieve MgO (100) orientation in the trilayer structure of the MTJ film was characterized using the TEM. It is also useful in detecting the regions where MgO diffusion takes place. The TEM uses a high energy electron beam to pass through a very thin sample and the transmitted electrons are collected via a fluorescent screen coupled by a fiber-optic plate to a CCD camera. The electrons are scattered by the sample due to the screening potential around an atomic nucleus. These scattered electrons give a picture of the crystal structure in the films and this technique is known as selective area diffraction (SAED) [151].

3.5.6 Electrical characterization – Four point probe measurement

The first step in characterizing STT devices is to observe the change in the device magnetoresistance with the external magnetic field. For this purpose, the work presented in this thesis made use of a four point probe measurement system. The system, shown in Fig. 3-18, houses four individual probes of 20 μm tip diameter which can be used to make contact with the electrode pads. The system incorporates an electromagnet to generate an in-

plane magnetic field in the range of -800 to +800 Oe. A CCD camera connected to the microscope helps to locate and position the probes on 300 μm-sized contact pads.

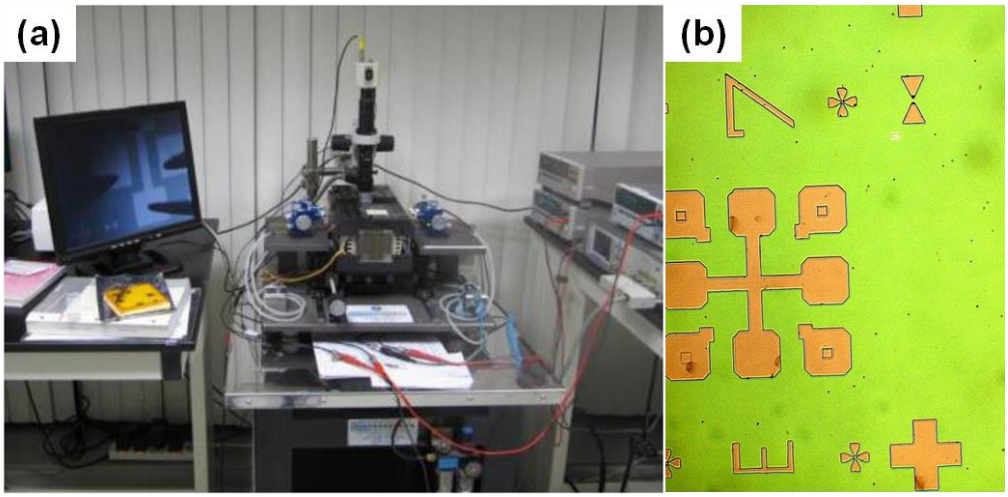

Figure 3-18: (a) Probe station for MR measurement of nanopillar junctions. (b) Microscope image of the completed device. The connected leads are the top electrode while the isolated leads are the bottom electrode.

3.5.7 High-frequency measurements

The characterization of microwave-assisted magnetization reversal by spin pumping experiments was carried in a high-frequency measurement setup. The setup shown in Fig. 3-19 houses a 6 kOe electromagnet at the minimum pole separation distance. Two GSG antennas are connected to this setup terminated by 2.4mm GSG probes (Picoprobe^{TM} from GGB Industries Inc.) which can operate up to 50 GHz.

The high frequency measurements in this thesis involved passing microwave currents in the GHz frequency range. For this purpose, the current-carrying conductors were designed in a special way to minimize electric losses at such high frequencies. The conductors were designed either as coplanar waveguides (CPW) or linear striplines. A CPW consists of a central strip carrying the microwave signal and two ground planes on either side of the

strip. Figure 3-20 shows the schematic of a CPW and the electromagnetic field distributions due to a signal passing through it. To obtain good signal-to-noise ratios, the characteristic impedance of the CPW should be ~50 Ω. The impedance of the CPW can be controlled by varying the thickness of the signal line, spacing between the signal and ground lines, thickness of the deposited electrode material, and choice of substrate.

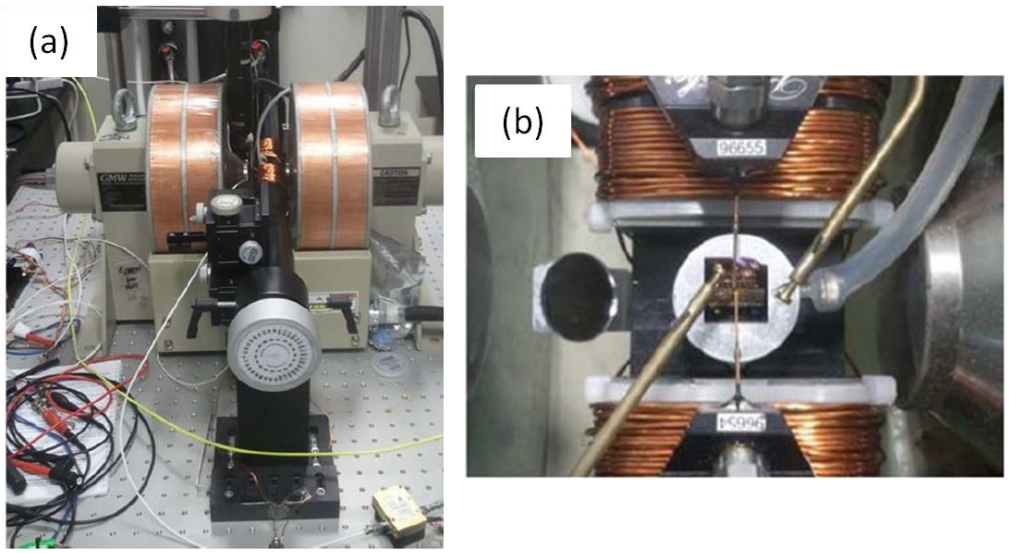

Figure 3-19: (a) High-frequency measurement setup. The orange cylinders house the electromagnet coils. (b) Close-up view of the sample stage between the electromagnet poles. The system has two GSG and two DC probes.

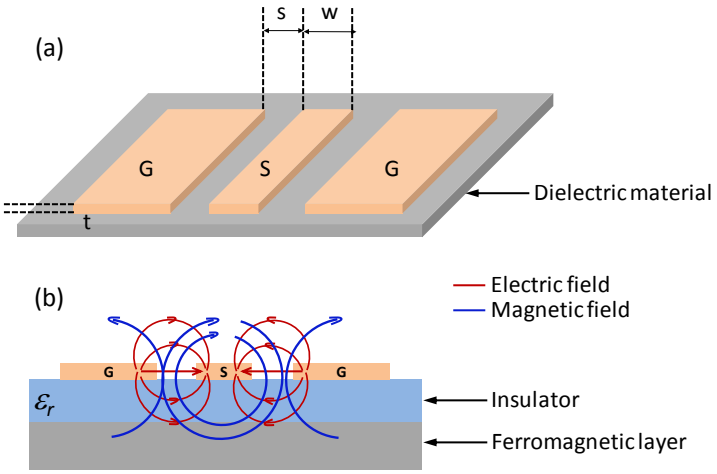

Figure 3-20: (a) Design of a coplanar waveguide. (b) Cross-sectional view of the coplanar waveguide with electric field and magnetic field distributions.

In linear striplines, the design is far simpler. It consists of a single conducting strip that is matched to 50 Ω outputs. The impedance can be tuned only through the width of the conducting strip at the point of contact and the thickness of the deposited material.

Chapter 4: Time-domain studies of non-reciprocity and interference in spin waves by magneto-optical Kerr effect (MOKE)

4.1 Motivation

Recent research in the field of alternative recording technologies such as MAMR has highlighted the capability of spin waves in synchronizing spin torque oscillators or assisting the reversal process itself by lieu of propagating magnetization dynamics. As materials approach the micron scale and below, shape effects play an increasingly strong role in influencing precessional dynamics and can give rise to multiple higher order spin wave modes for a high frequency pulse excitation. These factors have made it important to understand the propagating spin wave characteristics in patterned elements in a time scale similar to the switching durations, as MAMR applications will be within such time and length scales.

In this chapter, we investigate spin wave propagation characteristics in micron-sized rectangular elements of permalloy. We study the interference patterns generated as a result of the magnetization profile created in the element by pulse-generated Oersted fields. Our time-resolved measurements reveal the existence of a unique spin wave beating interference pattern in time, and also demonstrate the ability to tune spin wave non-reciprocity by an external magnetic field. These results are useful in understanding the effects of spin wave interference on MAMR.

4.2 Introduction

Spin waves are defined as propagating disturbances in the magnetic ordering of materials such as ferromagnets, ferrimagnets and antiferromagnets via exchange or magnetostatic interactions. The characteristics of spin waves can be tuned by varying the static magnetization (M) and direction of spin wave propagation (k). These properties have generated immense interest in spin waves due to their potential applications in high-speed information processing [2, 152-156], synchronization of spin torque oscillators [157, 158] and enhancement of the spin pumping effect [159]. Recent reports of interference-mediated modulation of spin waves have highlighted these capabilities by providing a new tuning parameter in designing such circuits [160, 161]. Logic gates based on spin waves have been proposed and experimentally demonstrated [162, 163]. Hence, it is important to understand the magnetization dynamics on a nanosecond time scale in greater detail, as most technological applications will operate in this regime.

The experimental study of spin wave dynamics requires the use of systems with high temporal and/or spatial resolution. Electrical techniques such as spin wave spectroscopy are limited in their spatial resolution, while optical techniques such as micro-Brillouin light spectroscopy (micro-BLS) offer impressive spatial resolution (~250 nm) [164] but moderate temporal resolution. Spin wave excitation and propagation characteristics in laterally confined magnetic stripes using micro-BLS have been extensively studied in recent years [164-168]. The finite size effect due to the lateral confinement of spin waves results in interference between spin wave modes revealing spatial dependency of the spin wave intensity [164, 166]. Time-resolved magneto-

optical Kerr effect (TR-MOKE) scanning microscopy has been used to explore the temporal characteristics of spin wave propagation [169-172]. Spin waves have been detected at distances up to 80 μm away from a coplanar strip (CPS) line [169] in thin permalloy films using coplanar waveguides antennas. Studies on thin permalloy ($Ni_{80}Fe_{20}$) films of different aspect ratios and geometries have reported the observation of mode interference of single-frequency spin waves in the *k*-space [169, 172, 173].

In this chapter, the propagation of spin waves in thin permalloy ($Ni_{78}Fe_{22}$) films is studied by means of TR-MOKE microscopy. A low frequency beat-like interference pattern is observed at the centre of the stripe due to two distinct spin wave frequencies. A simple mathematical model is provided to explain the observations, and it is shown to have a good correlation with the experimental data. In addition, a clear non-reciprocity in the spin wave propagation characteristics under the influence of an external magnetic field is confirmed by time-resolved data. The existence of different spin wave modes across the stripe is shown through spatial dependence measurements, and is attributed to the varying magnetization profile across the stripe.

4.3 Experimental methods

The experiments were performed on samples grown on Si/SiO_2 (300 nm) substrates. Continuous films of composition Ta (2 nm)/ $Ni_{78}Fe_{22}$ (30 nm)/ SiO_2 (3 nm) were sputtered at a base pressure of 2×10^{-9} Torr. The films were patterned into 200 μm × 20 μm stripes by electron-beam lithography. A 9 μm-wide microstrip line of thickness Ta (5 nm)/Cu (150 nm) was deposited and

patterned over the centre of the stripe by standard sputtering and photolithography processes. An external magnetic field (H_b) was applied perpendicular to the long axis of the Py stripe and the electrical pulse-generated Oersted field (h_{pulse}), as shown in Fig. 4-1(a). An electrical pulse of 10 V amplitude and 5 ns duration, with a rise time of 55 ps, was applied to the stripline to generate the Damon Eshbach spin wave propagating to the ±y-direction [174]. The magnetic response was probed by a 45 ps optical pulse with a wavelength of 405 nm in the transverse mode configuration, and the pump-induced Kerr rotation was measured as a function of the delay time between the pump and probe pulses. The measured signal is proportional to the *y*-component of the dynamic magnetization. Figure 4-1(b) shows a representative time response of a signal measured in this setup at the centre of the stripe with a clear Gaussian spin wave packet envelope, while Fig. 4-1(c) shows a representative FFT response of a measured data set resulting from the rising and falling edges of the pulse with an offset in the *y*-axis.

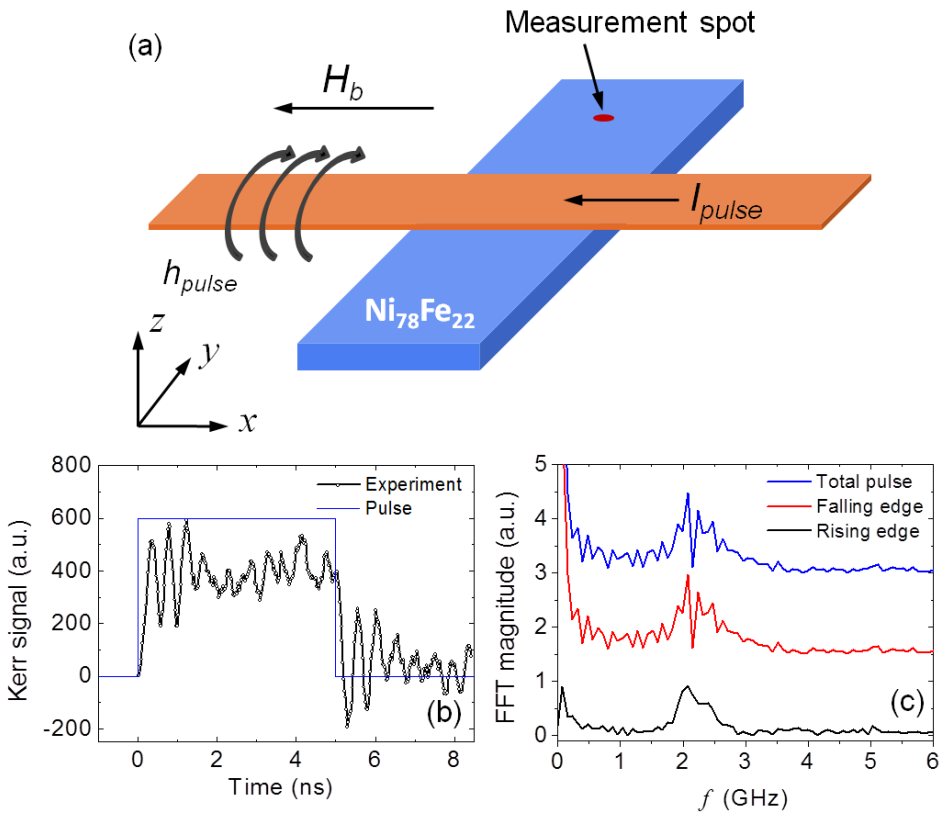

Figure 4-1: (a) Schematic diagram of the experimental setup. The sample is a Py micro-stripe of dimensions 200 μm × 20 μm. A square pulse (I_{pulse}) is applied along the 9 μm-wide stripline, and an external bias field H_b along the $-x$-axis. (b) Time response at a distance of 8 μm from the stripline in the 20 μm-wide stripe for a 10 V, 5 ns current pulse. The open black circles represent the experimental data and the solid red line represents the mathematical fit. (c) Frequency spectrum of a representative data set for rising and falling edges of the electrical pulse.

4.4 Spin wave measurements in the time-domain

Spin waves, excited in the Py stripe in the DE mode, are characterized by time-domain measurements to extract several key parameters of spin wave propagation such as mode characterization, spin wave decay length, and nonreciprocity. The external magnetic field was applied to a maximum of ±100 Oe using a home-made electromagnet. The Py stripe saturates in the transverse direction (along its short axis) for an external field (H_b) of ±50 Oe.

Figure 4-2 shows the characteristic dependence of the spin wave frequency on the external bias field (H_b) at the centre of the Py stripe measured 10 μm away from the current-carrying stripline. The spin wave frequency dependence can be explained by fitting with the magnetostatic surface spin waves (MSSW) dispersion relation:

$$f = \frac{\gamma_o}{2\pi}\sqrt{H\left(H+4\pi M_s\right)+\left(\frac{4\pi M_s}{2}\right)^2\left(1-\exp\left(-2kd\right)\right)} \qquad (4.1)$$

where H is the total effective field in the system, γ_o = 17.6 MHz/Oe is the gyromagnetic ratio, k = 0.5678 μm^{-1}, and the film thickness d = 30 nm. Two frequencies are observed at every bias field value, indicating multiple spin wave mode generation from the square pulse excitation. Both modes are well-fitted with the MSSW dispersion and may be excited for the same 'k'-vector, as has been reported before [175]. Slightly different frequencies from these modes are critical to the interference studies discussed further on.

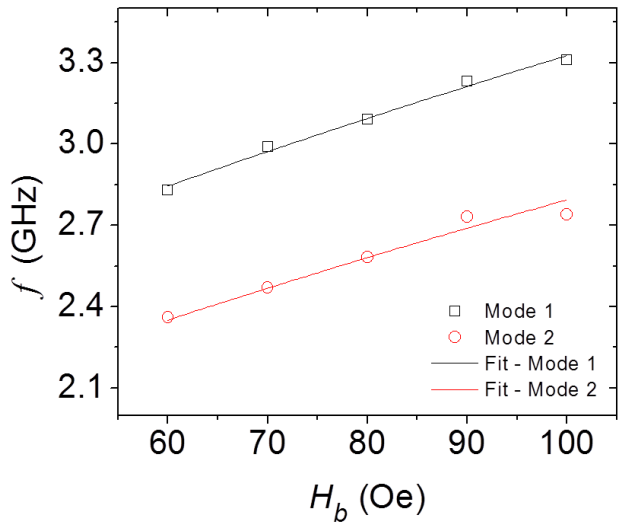

Figure 4-2: Frequency of magnetostatic surface spin wave (MSSW) modes as a function of magnetic field (H_b), measured at the centre of the stripe. Open circles and squares represent the centre mode frequencies, while the solid lines represent the calculated fits according to the MSSW dispersion relation.

To understand the evolution of the centre modes, we analyzed the spatial dependence of the spin wave intensity. Measurements were performed at different distances from the current-carrying stripline by moving the laser spot along the long axis of the Py stripe, and the time-resolved data is shown in Fig. 4-3. The spin wave amplitude (*A*) is extracted from a fitting of the measured signals in the time domain, as shown in the inset of Fig. 4-4 using a Gaussian wave packet of the form $y = A\exp\left[-(t/\tau)^2\right]$, where τ is the spin wave decay time, and the spin wave decay length Λ = 15.44 μm is extracted from the exponential fitting with the formula $A\exp(-x/\Lambda)$, where '*x*' is the distance from the stripline [175, 176] as shown in Fig. 4-4.

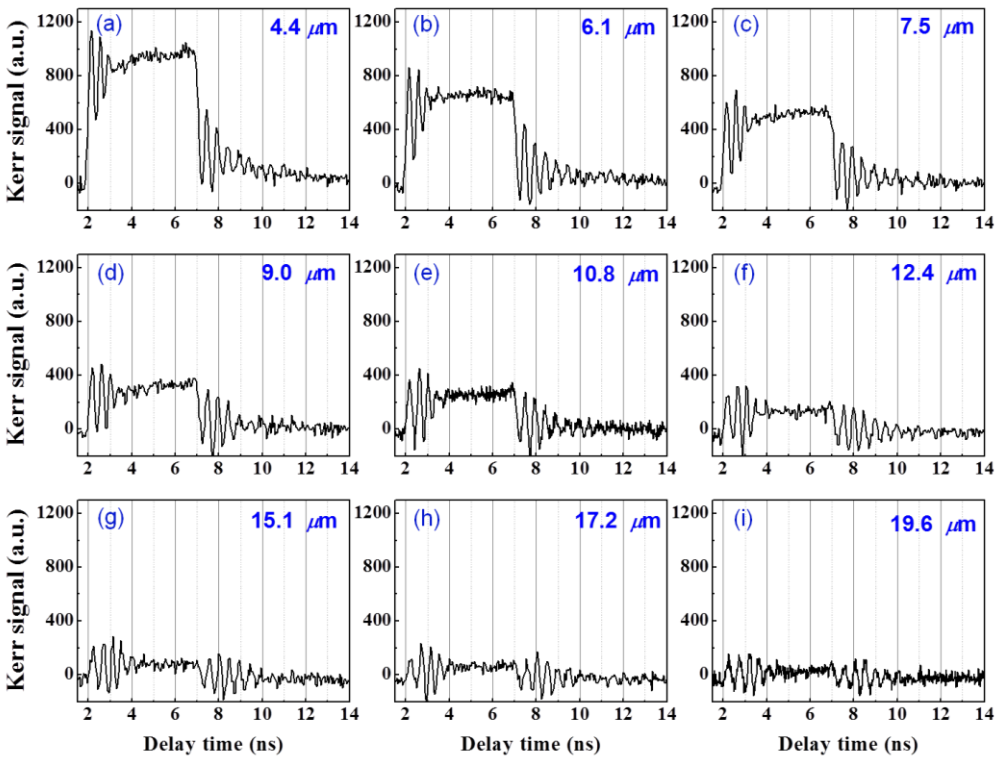

Figure 4-3: (a-i) Time-resolved measurements of spin waves at different distances from the stripline.

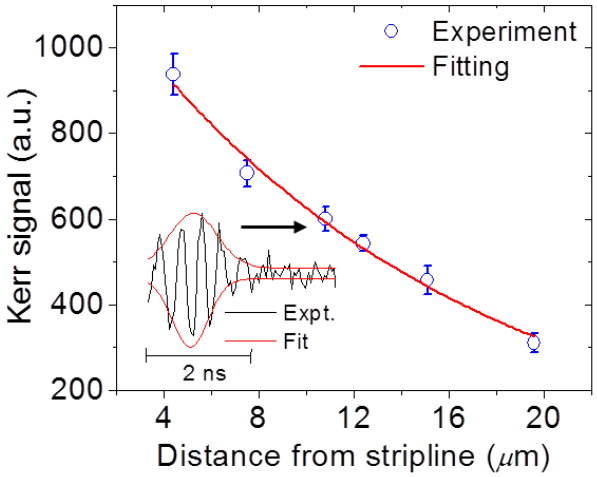

Figure 4-4: Variation in the spin wave intensity as a function of distance from the stripline. The solid red line represents the exponential decay fitting to extract the spin wave decay length. Inset shows a sample Gaussian fitting of the measured spin wave packet to extract the spin wave amplitude.

4.4.1 Non-reciprocal behavior of spin waves

The amplitude of the MSSW signal depends on the relative directions of the magnetization (M) of the material and the spin wave wave-vector (k). Clear non-reciprocal behavior of spin waves is known to exist for opposite signs of wave-vectors ($\pm k$) or bias field ($\pm H_b$), as shown in Fig. 4-6(a), [165, 176, 177]. Therefore, the non-reciprocity factor (κ), defined as $\kappa = A(H_{b+})/A(H_{b-})$, is a function of the bias field as shown in Fig. 4-6(b), similar to electrical measurements of surface spin waves [163]. The non-reciprocity in Fig. 4-6(a) and 4-6(b) is evaluated at a distance of 10 μm from the stripline. The non-reciprocal behavior arises as a result of the asymmetric distribution of the out-of-plane component of the excitation field (h_z) on either side of the stripline [165, 177] , as shown in Fig. 4-5 below.

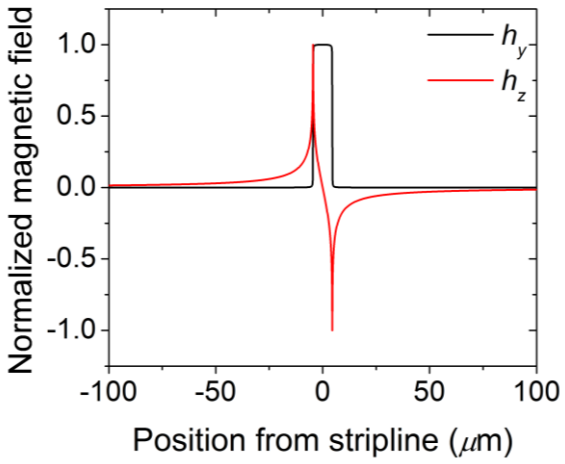

Figure 4-5: Spatial profile of the magnetic fields generated due to the square pulse current through the stripline.

The in-plane component of the excitation field (h_y) retains the same phase across the stripline, while h_z undergoes a phase change of π. As a result, the spin waves excited due to the in-phase h_y and h_z fields (on one side of the stripline) are stronger than those excited by out-of-phase h_y and h_z fields (on the opposite side of the stripline), resulting in the non-reciprocity of spin waves. The magnitude of κ is of the same order as previously reported [176, 177], and can be tuned by adjusting the width and thickness of the stripline which controls the excitation field (h_{pulse}). This phenomenon has promising potential in the field of logic devices to represent binary states of '1' and '0', as has been recently proposed [163].

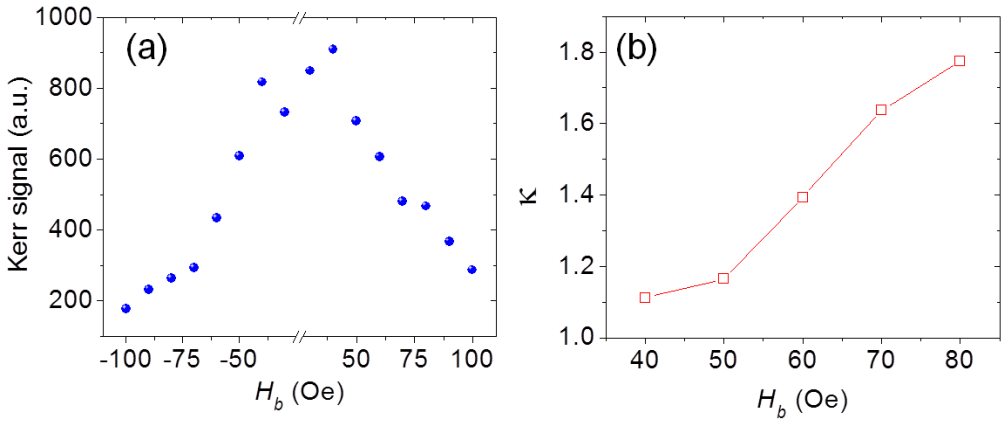

Figure 4-6: (a) Variation in the spin wave intensity as a function of magnetic field (H_b). (b) Non-reciprocity κ in magnetostatic surface spin waves as a function of magnetic field (H_b). All measurements were performed on a 10 V, 5 ns current pulse.

4.4.2 Effect of spatial confinement on spin wave mode generation

The aspect ratio (10:1) of the Py stripe is another factor that can affect the spin wave characteristics due to spatial confinement [164-166, 178]. The effects of this parameter were studied by measuring the spin wave characteristics at different distances from the left edge to the centre of the stripe. The FFT spectra are shown in Fig. 4-7(a) and 4-7(b), which correspond to the data measured at distances of 5 and 10 μm away from the current-carrying stripline, and the corresponding time-domain data are shown in Fig. 4-7(c) and 4-7(d), respectively. The measurement data, carried out at H_b = 75 Oe with a 10 V electrical pulse of 0.2 ns duration, are consistent with the existence of localized edge modes at the edges of the stripe [178-180]. Due to the shape anisotropy, the magnetization at the edges is pinned along the long axis of the Py stripe while the magnetization towards the centre of the stripe tends to align with the external bias field. This creates a varying magnetization profile across the width of the stripe [180], which has been used to explain that the spin wave dispersion relation changes as a function of position [171, 179,

181]. Due to the varying demagnetizing field profile and stronger exchange interaction effects at the edges [178, 180], a weaker effective field exists at the edges as compared to the centre of the stripe. As a result, the frequencies of the edge mode are lower than that of the centre mode.

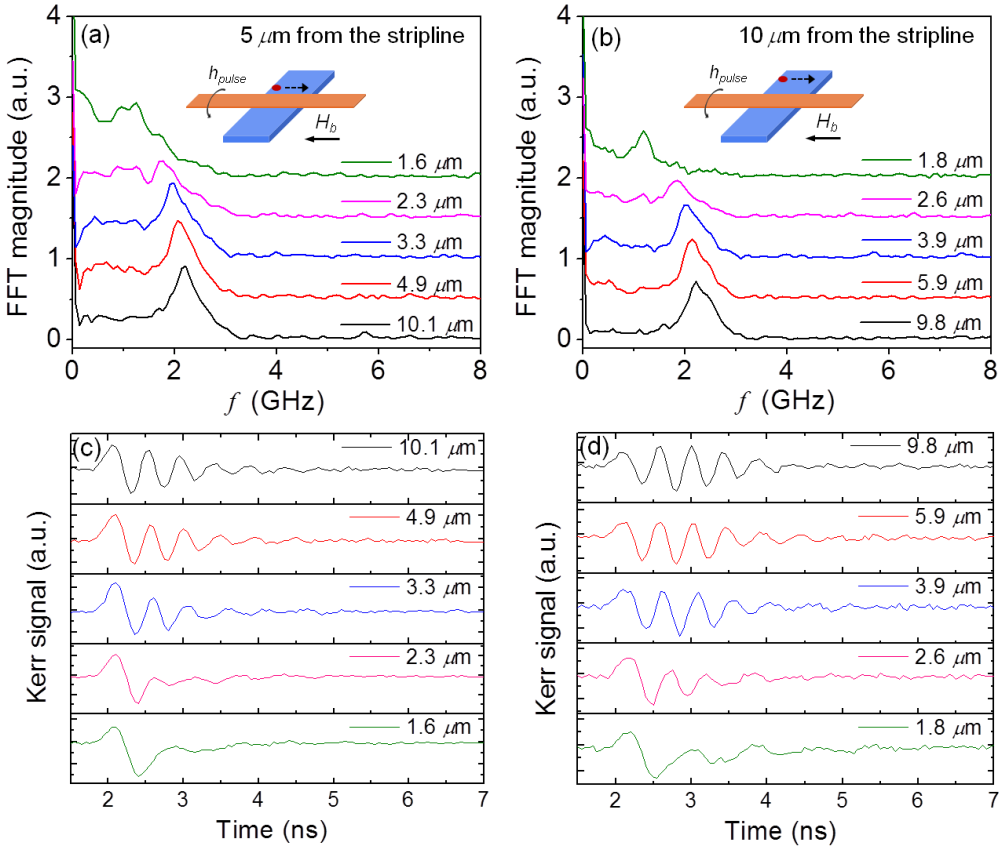

Figure 4-7: (a), (b) Spin wave frequencies at different distances from the left edge of the 20 μm wide stripe. The measurements were performed at a distance of 5 μm and 10 μm from the stripline respectively on a 10 V, 0.2 ns current pulse. (c), (d) Temporal response data of the above measurements.

4.4.3 Spin wave beating – interference in the frequency domain

Spatial dependence studies revealed the existence of a frequency beat-like interference pattern at a certain distance from the stripline, as seen in the measured signal in Fig. 4-8(a). The FFT spectrum in Fig. 4-8(b) clearly shows the existence of two frequency peaks in close proximity. Unlike previous spin wave mode interference studies [164, 166, 173], the origin of the observed

interference is not in the *k*-space, but rather in the frequency space. In other words, the spin wave modes causing the interference are separated by frequency, rather than by different '*k*' values for the same frequency. Our result is also different from a recent study, in which an oscillatory spatial intensity pattern superimposed on the exponential decay was observed by the BLS technique [182]. On the other hand, in our case, the beating pattern can be attributed to the interference of the two centre spin wave modes measured in Fig. 4-2. The two centre modes, having different frequencies, will have a phase difference with which they arrive at the same given location. We model the oscillatory beat pattern as interference between two Gaussian spin waves of slightly different frequencies arriving at a given location at the same time as:

$$y(t) = y_o + B_1 \exp\left(-\frac{1}{2}\left(\frac{t-t_1}{\sigma_1}\right)^2\right)\sin(2\pi f_1 t) + B_2 \exp\left(-\frac{1}{2}\left(\frac{t-t_2}{\sigma_2}\right)^2\right)\sin(2\pi f_2 t) \quad (4.2)$$

where f_1 = 2.22 GHz and f_2 = 2.46 GHz are the respective frequencies of the Gaussian spin wave packets, t_1 = 1.005 ns and t_2 = 4.37 ns are the temporal positions of the peaks of the respective Gaussian spin wave packets, σ_1 = 0.464 ns and σ_2 = 1.11 ns are the full-width half maximum (FWHM) of the two spin wave packets, B_1 = -197.557 a.u. and B_2 = -120.281 a.u. are the respective amplitudes of the two wave packets, and y_o = 399.766 a.u. is the initial offset. This model fits well with the experimental time-domain data shown in Fig. 4-8(a), and the frequency values also show reasonably good agreement.

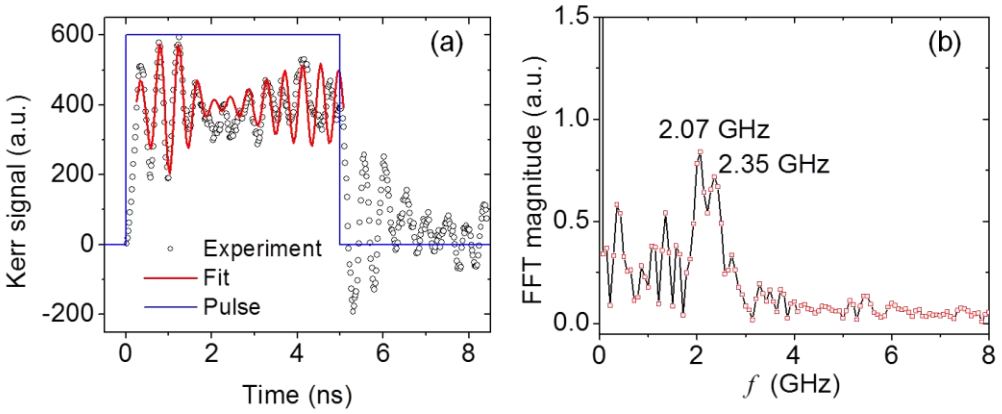

Figure 4-8: (a) Time-resolved measurements of spin wave beating interference pattern at a distance of 8 μm from the stripline in the 20 μm-wide stripe for a 10 V, 5 ns current pulse. The open black circles represent the experimental data and the solid red line represents the mathematical fit. (b) Frequency spectrum of the time-domain signal revealing two distinct peaks.

To understand if the time-domain beating signature could occur due to the interference of more than two frequency modes, we analyzed the frequency spectrum as a function of the magnetic bias field. In Fig. 4-9, two *main* frequency modes can be seen for all values of H_b, indicating that only two modes are dominant at the centre of the magnetic stripe. The mathematical expression in Eqn. 4.2 was modified to incorporate a third frequency term. However the fitting result was poor with respect to the experimental data. Thus, we confirmed that the time-domain beating was due to the interference of two main modes.

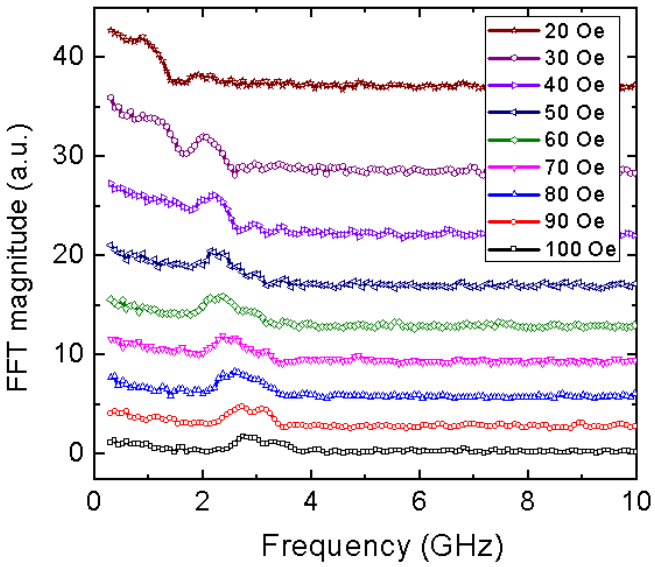

Figure 4-9: Magnetic bias field (H_b) dependence of the frequency spectrum of the excited spin waves. The data clearly shows the presence of two *main* frequency modes.

Thus, the interference of the two centre spin wave mode frequencies results in a unique mode-beating interference pattern, which is different from previous mode interference studies that were identified in the *k*-space. These results could have implications on the proposed applications of spin waves in information processing devices, and require a more detailed study of spin wave interference patterns in confined structures.

4.5 Conclusions

In summary, we have observed a beating pattern in time domain due to the interference of two spin waves with different centre mode frequencies. We model the interference based on a simple mathematical model considering frequency- and phase-separated Gaussian spin waves and show good correlation between the measured and fitting data. We have also demonstrated, in the time domain, the non-reciprocity effect of spin waves as a function of the applied bias field – a phenomenon that can be engineered to create spin

wave-based logic circuits. Our large micron-sized Py stripes also showed the presence of lower frequency localized edge modes which have been previously demonstrated for stripe widths with a larger degree of spatial confinement (width < 1 μm), hence suggesting the need for a better understanding of the shape effect on spin wave quantization. These results demonstrate that spatial confinement can result in the generation of several spin wave modes of varying strengths, leading to a complex magnetization dynamic picture. Furthermore, spin wave interference could undesirably affect synchronization schemes of spin torque oscillators using spin waves, an area of research that requires further detailed study.

Chapter 5: Spin pumping-mediated characterization of microwave-assisted magnetization reversal

5.1 Motivation

The study of the microwave-assisted magnetization reversal (MAMR) phenomena revealed that switching is most efficient under the conditions of resonance. At resonance, maximum energy is absorbed from the microwave excitation, resulting in larger precessional torques. Hence, it is important to identify and access these resonant states in a ferromagnetic material to make switching by MAMR easier. Techniques such as FMR spectroscopy and magneto-optic Kerr effect (MOKE)-based spectroscopy require expensive, state-of-the-art equipment and careful design of the coplanar waveguides (CPWs) to ensure good impedance matching. A characterization technique that can assess the suitability of magnetic materials to MAMR processes, while simplifying the design considerations for testing would be of great use in the MAMR research field.

In this chapter, we study the microwave-assisted reversal behavior of magnetic structures for different aspect ratios. By utilizing the phenomenon of spin pumping, we are able to convert a time-varying magnetic signal into a simple DC output signal which provides information about the magnetic state of the material under consideration. This technique will be shown to be a simple yet efficient characterization technique.

5.2 Introduction

The ferromagnetic resonance (FMR) technique is one of the most well-known methods for characterizing small angle magnetization dynamics [183]. In the FMR mode, all the magnetic moments are precessing in phase, and therefore do not propagate any magnetic disturbances. It is possible to determine the resonance frequency of a given material in a magnetic field from the Kittel formula, as discussed in Chapter 2. Thus, it is possible to map the resonant states in a given material by sweeping the microwave frequency and magnetic field simultaneously in a vector network analyzer (VNA). Recent experiments have harnessed this technique to determine the conditions at which the lowest microwave excitation power is required to cause magnetization reversal [76-78]. Another useful feature of the VNA measurement scheme is the ability to generate non-linear dynamics in patterned devices such as rings [184] and nanowires [185]. The MAMR process is one of the non-linear resonance dynamics [69] and hence, such studies are of practical significance in understanding the criteria for reversal and the critical microwave fields required to do so. In MOKE studies [80, 81], simple experiments have proven the concept of MAMR by analyzing the static hysteresis loops with and without the addition of a microwave signal. Magnetic force microscopy (MFM) has also been utilized to study MAMR [48, 75], but this technique is severely limited in understanding the switching process as it cannot access the dynamic magnetic information. With the exception of MFM, complex impedance matching between the sample and the measurement equipment is required in order to obtain good signals in other measurement methodologies. Therefore, a novel characterization technique

that converts the time-varying magnetic signal to a simple output signal is of great importance and timely.

In this chapter, a new way of detecting microwave-assisted reversal in patterned and thin film magnetic structures utilizing the spin pumping phenomenon is proposed. It has been shown that the magnetization reversal of the ferromagnetic material can be detected by a change in the polarity of the measured spin pumping voltage signal. The measured signal is a simple DC output voltage, and though it is a static measurement technique, the ability to sweep frequency while measuring the spin pumping signal simultaneously enables us to extract information about the switching mechanism involved. In both thin films and patterned microwire arrays, the presence of partial switching is detected by the onset of switching processes below the FMR frequency of the device under consideration. The effect of the static bias field in reducing the energy gap between the two stable states is also investigated by means of spin pumping.

5.3 Spin pumping and the inverse spin Hall effect (ISHE)

Spin pumping is a phenomenon in which a spin current is induced in a non-magnetic material (NM) that is attached to a ferromagnet (FM) with precessing magnetization [32, 159, 186, 187]. In other words, the precessing magnetization ‘pumps’ spins into the NM layer, thereby generating a spin current flow. This effect has been postulated by Berger [188] and it was observed in a simple $Ni_{81}Fe_{19}$/Pt film using the inverse spin Hall effect (ISHE) [189-191]. The spin current generates a proportional charge current in the NM layer (in this case, Pt), which is detected as a voltage across the end of the Pt

layer. The generated charge current, spin current induced in the NM layer and the spin polarization can be related as:

$$J_c = \theta_{SH}\left(J_s \times \sigma\right) \tag{5.1}$$

$$\text{where, } J_s = \left[-\frac{\hbar g_{\uparrow\downarrow}\gamma^2 h_{rf}^2 \left(M\gamma + \sqrt{M^2\gamma^2 + 4\omega^2}\right)}{8\pi\alpha^2\left(M^2\gamma^2 + 4\omega^2\right)} \frac{\lambda_{NM}}{d_{NM}} \tanh\left(\frac{d_{NM}}{2\lambda_{NM}}\right) \right] \hat{z} \tag{5.2}$$

and, J_c is the charge current density, J_s is the density of the spin current induced from spin pumping, θ_{sh} is the spin Hall angle of the nonmagnetic heavy metal, σ is the spin orientation, $g_{\uparrow\downarrow}$ is the interlayer spin-mixing conductance, α is the damping constant in the magnetic layer, h_{rf} is the rf field amplitude, ω is the ferromagnetic resonance frequency ($2\pi f$), M is the saturation magnetization of the magnetic layer, γ is the gyromagnetic ratio of a free electron, λ_{NM} is the spin diffusion length in the NM layer, and d_{NM} is the thickness of the NM layer [191]. When the FM layer is at resonance, the spin pumping effect is maximized and we use this effect to study MAMR in ferromagnetic material systems. The phenomenon of spin pumping occurs as a result of energy minimization considerations in the system. The precessing magnetization, in contact with a paramagnetic metal, transfers spin angular momentum to the nonmagnetic metal across the interface resulting in increased damping of the magnetization oscillations. The conversion of the spin current to charge current is, on the other hand, a result of spin orbit coupling in the nonmagnetic metallic layer. In addition to intrinsic coupling effects, two main mechanisms are responsible for this conversion – namely skew scattering and side-jump scattering. All three mechanisms arise due to the spin orbit interactions in the nonmagnetic layer, and are usually stronger in

heavy metals such as Pt or Ta (due to the band structure) [192-197]. The measure of this conversion of spin current to charge current is given as a ratio θ_{SH}, and is called the spin Hall angle. Further discussion on the spin-orbit coupling mechanisms is not in line with the objectives of this study on MAMR, and hence, we proceed with the current understanding.

5.4 Experimental methods

The films for this study were deposited in a magnetron sputtering chamber with background pressure of 2×10^{-9} Torr, followed by standard photolithography, ion milling, and lift-off process steps. Two samples with in-plane anisotropy were prepared. Sample A was a Pt (10 nm)/$Co_{60}Fe_{20}B_{20}$ (20 nm) stack, and sample B was a Pt (10 nm)/$Ni_{78}Fe_{22}$ (20 nm) stack. A Pt strip of dimensions 800 μm × 600 μm × 14 nm was patterned first, followed by the addition of the magnetic layer, before which 4 nm of the Pt stack was ion-milled to ensure good electrical contact between the two layers. The magnetic layer in sample A was patterned into a large thin film of dimensions 300 μm × 619 μm × 20 nm, as shown in Fig. 5-1(a,b). Sample B, on the other hand, was patterned into an array of 53 equally-spaced micro-wires of dimensions 5 μm × 619 μm × 20 nm with a spacing of 5 μm, as shown in Fig. 5-1(c). Both sample stacks were encapsulated by a 20 nm-thick SiO_2 layer covering only the area of the magnetic layer. Finally, shorted coplanar waveguides (CPWs) and DC probe pads of Ta (5 nm)/Cu (150 nm) were defined and sputter-deposited on the samples. The oxide layer between the CPW and the magnetic layer ensures that only the microwave field is coupled to the latter and there

are no current shunting effects. Sample A was annealed at 300 °C for 30 minutes in a magnetic field of 200 Oe.

Figure 5-1(a) also shows a schematic representation of the experimental setup and the orientation of the co-ordinate axes. The bias field (H_b) was applied along the *x*-axis and the microwave signal was applied to the 50 Ω-shorted CPW to generate an Oersted field ***h*** perpendicular to the external field. This setting ($\boldsymbol{h} \perp H_b$) induces precessional dynamics in the magnetic layer. The precessing magnetization pumps a spin current into the adjacent Pt layer, and this spin current generates a proportional charge current across the Pt strip as a result of ISHE. The charge current was detected as a dc voltage at the contact pads.

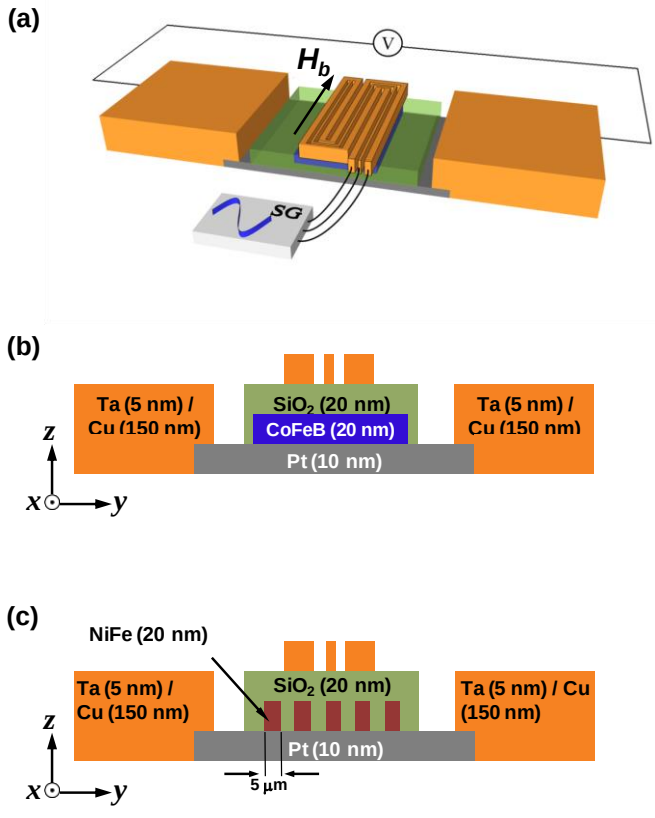

Figure 5-1: (a) Schematic representation of the device geometry (not to scale) and the measurement setup. The CPW is connected to a signal generator (SG) and a voltmeter is connected across the Pt for measuring the spin-pumping signal (V_{SP}). (b) Cross-sectional view and film composition of sample A. The

CPW shown here is a simplified version. (c) Cross-sectional view and film composition of sample B in an experimental setup similar to sample A. In this case, the magnetic layer is Permalloy (NiFe) patterned into an array of 5 μm-wide wires with a spacing of 5 μm.

Line-shape analysis of the measured spin pumping signal:

The DC voltage signal measured in the experimental configuration described above is not limited to spin pumping contributions alone. Spin rectification effects occur when a portion of the rf current in the waveguide is capacitively coupled into the ferromagnetic layer. This coupled current also flows in the same direction as the rf current in the waveguide, and generates a DC signal due to effects such as anomalous Hall effect (AHE), planar Hall effect (PHE) and anisotropic magnetoresistance (AMR) effect. As the spin pumping phenomenon is maximized at resonance, it follows that the contribution due to spin pumping will have a symmetric line-shape about the resonance field. In this section, an analytical study is carried out to understand the contributions of the spin rectification effects.

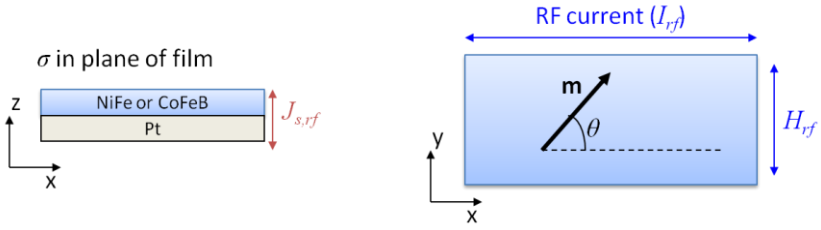

Figure 5-2: Schematic of the experimental configuration used for measurements. '**m**' indicates the instantaneous magnetization of the material undergoing precession.

In the above experimental configuration shown in Fig. 5-2, the magnetization dynamics can be described by the LLG equation as follows:

$$\frac{dm}{dt} = -\gamma\left(m\times\left(H_{DC}+H_{rf}\right)\right)+\alpha\left(m\times\frac{dm}{dt}\right) \tag{5.3}$$

where H_{DC} is the applied static magnetic field, H_{rf} is the microwave field generated due to the current (I_{rf}) flowing through the coplanar waveguide, m is the instantaneous magnetization of the ferromagnetic material, α is the damping constant, and γ is the gyromagnetic ratio. The magnetization will oscillate along both *x* and *y* directions, however the m_y oscillation is important for our experiment. The precessing magnetization *m* can be written in the form $m = Ae^{i\omega t}$. The solution of Eq. (5.3) is then found to be

$$m_y = \frac{H_{rf}\gamma\left[\gamma\left(\mu_0 + H_0\right) + i\omega\alpha\right]}{\omega_0^2 - \omega^2\left(1+\alpha^2\right) + i\omega\alpha\gamma\left(\mu_0 + 2H_0\right)} e^{i\omega t} \tag{5.4}$$

The ratio of the imaginary and real parts gives the phase difference (δ) of the precessing magnetization with respect to the microwave input. As a consequence of the oscillating magnetization, the Hall resistance also fluctuates as

$$\begin{aligned}
&R(\theta) = \mathrm{r}\cos\theta\sin\theta \\
&R(\theta,t) = \mathrm{r}\cos^2\theta\frac{d\mathrm{r}}{d\theta}\Delta\theta(t) - \mathrm{r}\sin^2\theta\frac{d\mathrm{r}}{d\theta}\Delta\theta(t) \\
&R(\theta,t) = \mathrm{r}\cos 2\theta\frac{d\mathrm{r}}{d\theta}\Delta\theta(t) \\
&R(\theta,t) \approx \mathrm{r}\frac{d\mathrm{r}}{d\theta}\Delta\theta(t), \text{as } \theta \approx 0^\circ \\
&\Delta\theta(t) = m_y
\end{aligned} \tag{5.5}$$

By algebraic simplification, we then have the spin rectification contribution as $V_{SR} = I'_{rf}R_{DC} = \left(I\cos(\omega t)R_1\cos(\omega t + \delta)\right)_{DC} = IR_1\cos\delta/2$. A plot of cos δ versus applied field, as seen in Fig. 5-3 (a, b), shows an anti-symmetric line-shape about an arbitrarily chosen resonance field. This is the reason for the

anti-symmetric line-shape observed for the DC contributions due to spin rectification.

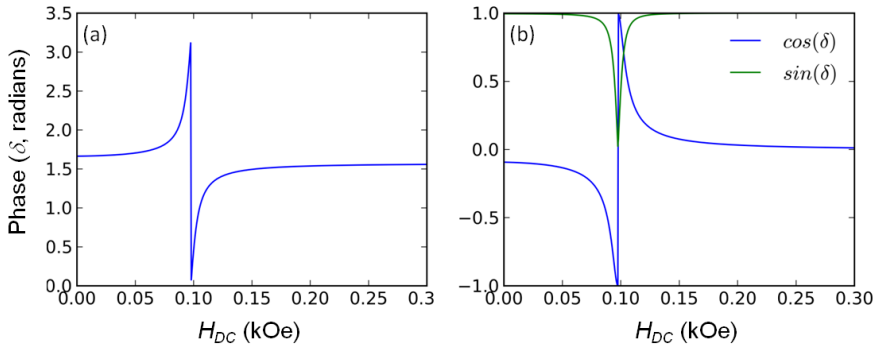

Figure 5-3: (a) Variation of phase of magnetization oscillation w.r.t to microwave input as a function of applied field (H_{DC}). (b) Variation of sinusoidal functions of the phase difference as a function of H_{DC}.

The symmetric and anti-symmetric components of the measured DC signal are then plotted as a function of the applied magnetic field, and are found to fit well with a Lorentzian wave-function. The fitting is one of convenience and accuracy, rather than due to an exact theoretical prediction; in fact, any peak function such as a Gaussian or a Lorentzian wave-function will be able to fit the measured waveforms to a reasonable degree.

5.5 Characterization of the magnetic quality of the films

The basic magnetic properties of the films were analyzed by studying the spin pumping signal as a function of the applied bias field, as shown in Fig. 5-4(a-d). The sample was initially saturated by a strong bias field in the *–x* direction. The microwave signal was applied in a frequency range from 1 GHz to 10 GHz at a constant power of 15 dBm, while the bias field was swept across the resonance field, given by the Kittel formula: $f_{res} = \gamma\sqrt{H_{res}\left(H_{res}+M_s\right)}$, where γ = 2π(28 GHz/T) is the gyromagnetic ratio

chosen for both CoFeB and Py. The magnetic layer was reset to its initial state for each microwave frequency. At resonance, the number of spins pumped into the Pt layer was maximized, therefore a peak was observed in the output voltage in Fig. 5-4(a,c). The peak shape is a summation of the symmetric and anti-symmetric parts of the spin-pumping signal, and the resonance field (H_{res}) can be extracted by fitting the waveform to a Lorentzian wave-function. The measured dc voltage was fitted with a Lorentzian wave-function to extract the symmetric and anti-symmetric components. Spin rectification effects such as AMR, AHE and PHE contribute a dc voltage that has an anti-symmetric line-shape in our experiments, due to the measurement configuration. The analytical derivation and theoretical description of the symmetric and antisymmetric contributions to the measured DC signal have already been discussed in Section 5.4; hence, we will proceed with that knowledge to quantitative contributions. We find that the antisymmetric component (0.42 μV) is one order lesser than the symmetric component (4.4 μV) and hence, is of negligible effect in our experiments. To analyze the contributions to the symmetric component of the measured voltage, an angular dependence study was performed by varying the angle (θ) of the magnetic bias field with respect to the direction of the microwave current. The measured data showed a clear dependence on the cos θ function, which is known to be the characteristic of the spin pumping phenomenon. The saturation magnetization (M_s) of the deposited CoFeB film in sample A was then extracted by fitting the resonance frequency versus bias field data to the Kittel formula, as shown in Fig. 5-4(b). The M_s for sample A was estimated to be 2.07 T. The FMR line-widths (62 Oe at 5 GHz) are comparable to the previous reports [198], and the enhancement

of Gilbert damping ($\Delta\alpha$) due to spin pumping has also been observed like the other studies [191, 199-202]. Similarly, the properties of sample B with the Py microwires were analyzed by fitting the resonance frequencies seen in Fig. 5-4(c) with the Kittel formula. This is shown in Fig. 5-4(d) where the extracted M_s value was 0.81 T. Reported values of the saturation magnetization of Py are close to 1 T. We believe that the decrease in our wires is a result of patterning defects.

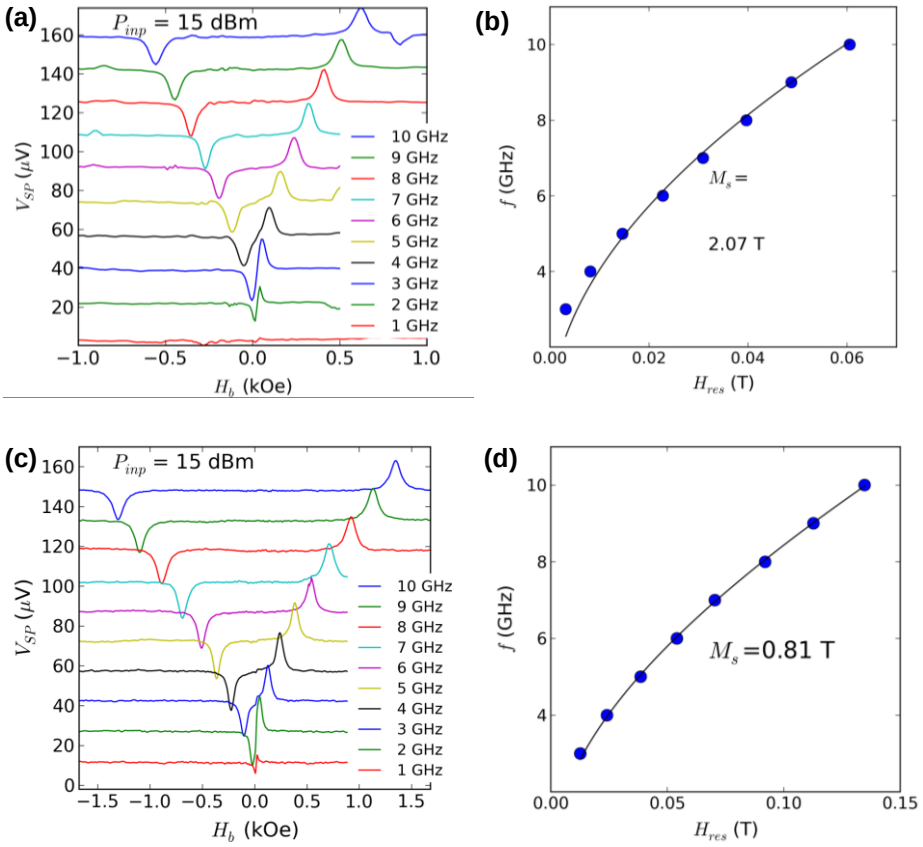

Figure 5-4: (a) Spin pumping signal (V_{SP}) of sample A as a function of the bias field at a constant microwave output of 15 dBm. (b) Kittel fitting of the resonance peaks to extract the saturation magnetization (M_s) of CoFeB. (c) Spin pumping signal (V_{SP}) of sample B as a function of the bias field at a constant microwave output of 15 dBm. (c) Kittel fitting of the resonance peaks to extract the saturation magnetization (M_s) of patterned Py. In both cases, the magnetization is saturated in the $-x$ direction for every microwave frequency before sweeping the magnetic field.

5.6 Spin pumping-MAMR experiments on extended CoFeB thin films

The application of a microwave field generates Larmor precession in the thin film. As the microwave field increases, the precessional torque – and as a result, the precession angle – increases under conditions of resonance. If the rate of energy absorption from the microwaves exceeds the rate of damping, the magnetization will reverse for a sufficient value of the bias field. This reversal is detected by a change in the polarity of the ISHE voltage, as the orientation of the pumped spins has changed. A change in the spin orientation will cause a change in the direction of the charge current flow. Therefore, we see a change in the polarity of the ISHE voltage upon magnetization reversal. Thus, the two main tuning parameters of the microwave signal are its excitation power (P_{inp}) and frequency (f).

Figure 5-5 shows the results of the variation in microwave power. At P_{inp} = 13 dBm, the magnetization showed clear resonant behavior (a dip) for H_b = 4.1 Oe and H_b = 15.6 Oe, before it completely reversed at H_b = 27.2 Oe, resulting in a peak. At P_{inp} = 14 dBm, the magnetization exhibited an abrupt change rather than a broad dip in the measured spin-pumping voltage (V_{SP}) at H_b = 15.6 Oe. The sudden decrease and change in the polarity of V_{SP} can be attributed to the partial reversal of the magnetic layer (domains are formed in parts of the CoFeB thin film), while the rest of the film remained in its initial magnetic state. This reversal caused a change in the orientation of some of the pumped spins, and consequently the overall ISHE voltage decreased in its absolute value. As the microwave power was increased to 16 dBm and then 18 dBm, this domain reversal behavior extended to larger regions. The

stronger microwave fields caused larger domains to form, and at 18 dBm the reversal was almost complete as evidenced by the presence of a clear peak with reversed polarity and line-widths comparable to those at higher bias fields. The increasing value of V_{SP} at higher microwave powers is due to larger oscillations causing higher spin pumping and in turn, a higher spin current that generates a higher charge current. At P_{inp} = 20 dBm, the magnetization has completely reversed from a dip to peak at H_b = 15.6 Oe, as there were no visible abrupt changes in the output signal.

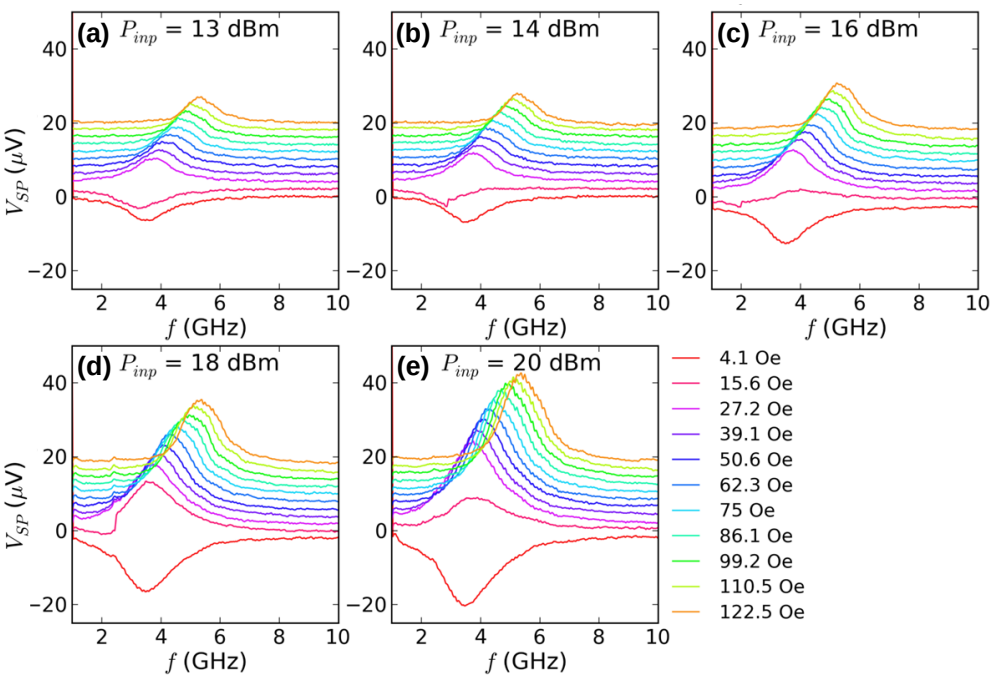

Figure 5-5: (a-e): Change in the effective coercivity of the CoFeB layer in sample A is seen as the microwave power is gradually increased, at different values of the bias field. The microwave power is swept from 10 dBm to 20 dBm in steps of 1 dBm. The abrupt jumps in the spin pumping voltage from P_{inp} = 14 dBm onwards indicate the onset of reversal.

To gain a more qualitative picture of the MAMR process, the switching process was studied as a function of the applied microwave power at a constant value for H_b. Figure 5-6(a-c) shows the data for an applied power in the range of 11 – 20 dBm. The CoFeB film was saturated in the –x direction

for every increment of the microwave power. At H_b = 3.3 Oe in Fig. 5-6(a), no switching occurred as the microwave field at P_{inp} = 20 dBm was not high enough to switch the material. The small dip in the spin pumping voltage at resonance is attributed to the small oscillations generated at this bias field value. At H_b = 15.2 Oe in Fig. 5-6(b), we observed the onset of microwave-assisted reversal at P_{inp} = 14 dBm, and by 19 dBm the material was completely switched, as indicated by a change from a dip to peak. At H_b = 39 Oe, the reversed polarity of V_{SP} indicates that the magnetic layer has already switched at P_{inp} = 11 dBm. This behavior can be understood by considering the energy barrier between the two stable magnetic states. For a magnetization reversal, the magnetization has to overcome this energy barrier and cross over into the other stable energy well. The static bias field helps to reduce the barrier height, while the precessional dynamics excited by the microwave field are used to climb up the energy well and cross over, where energy interactions determine the likelihood of switching. The static field is used to pull the magnetization out of its stable state in the energy well and increase its potential energy. At H_b = 3.3 Oe, this increase in energy is very small, and as a result the oscillations are also small, resulting in a weak signature of resonance.

In summary, a clear signature of microwave-assisted magnetization reversal was observed in thin films of CoFeB. In addition, it is also possible to identify the stages of switching from partial to full reversal of the thin film. A 37% effective change in coercivity was observed, which is in a similar range to other reported results in the literature [76, 78, 79, 85, 203].

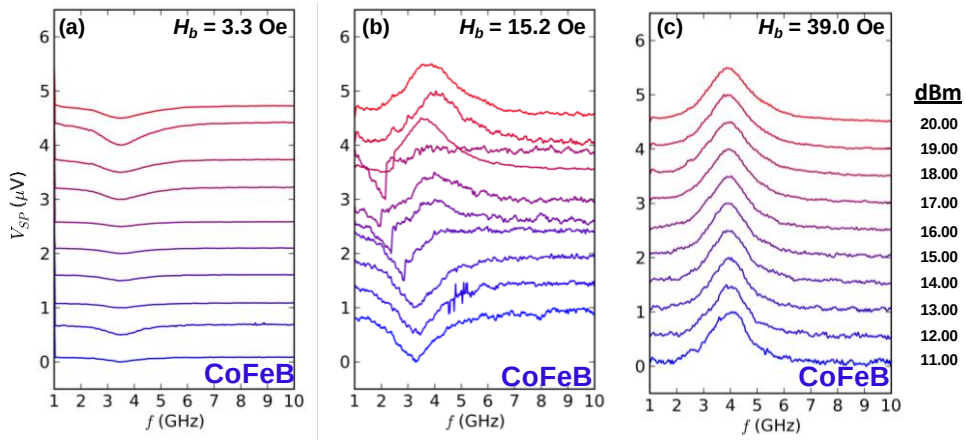

Figure 5-6: (a) ─ (c) Switching characteristics of the CoFeB layer in sample A for different values of constant bias field. The microwave power is swept from 10 dBm to 20 dBm at each bias field to study the switching behavior. (a) shows no reversal for any power, while (b) showing a switching profile at P_{inp} = 14 dBm onwards. Figure (c) shows that the magnetization has already switched even for the minimum power used.

5.7 Spin pumping-MAMR experiments on patterned permalloy microwires

In order to demonstrate that this characterization technique is suitable for other materials, we studied a patterned array of Py microwires in sample B. The external bias field was applied along the axis of the wires (*x*-direction) and the microwave field was applied perpendicular to the axis, as shown in Fig. 5-1(a,c). The reversal behavior was studied by sweeping the microwave power from 0 to 20 dBm, in finer steps of 1 dBm due to the soft magnetic nature of Py. Figure 5-7(a-f) shows a characteristic data set at 4 dBm intervals where the switching is most evident. At P_{inp} = 4 dBm, magnetization reversal is seen at H_b = 20.3 Oe, indicated by a change from a tip to peak. As the power increases to 8 dBm, we see a small abrupt jump at H_b = 11.8 Oe at f = 1.75 GHz, which is likely a case of partial switching followed by relaxation to the initial state. At 12 dBm, this reversal is more prominent at H_b = 11.8 Oe

represented by a broad peak; however, at f = 1.75 GHz the magnetization suddenly reverses back to its initial state. At higher powers, the Py wires switch completely and remain stable in the new configuration (peak).

The random 'switch-back' events at P_{inp} = 12 dBm can be attributed to the effects of spin pumping into the Pt strip and the design of the CPW over the microwire array. The dimensions of the CPW in both samples were 270 μm × 619 μm, which covers 90 % of the magnetic layer in sample A and 50% of the magnetic layer in sample B. As a result, the microwave field strength decreases as the distance of the wire from the CPW increases [204]. As the microwave power increases, the wires underneath the CPW undergo reversal while those away from the CPW do not switch as the microwave-generated fields are not strong enough to influence magnetization reversal. This partial switching is a likely scenario as seen from the output voltage frequency response at P_{inp} = 12 dBm where two features at 1.25 GHz (peak) and 1.75 GHz (dip) are seen. At higher microwave powers when the microwave field $\boldsymbol{h}$ is strong enough to overcome these inhomogeneous field effects, successfully complete switching takes place.

As in the case of sample A (CoFeB), the microwave-assisted switching data were analyzed under the conditions of a constant bias field and varying microwave power in Fig. 5-8. The magnetization was saturated initially in the $-x$ direction for every increment of the microwave power. The microwave power was varied from 5 dBm to 30 dBm, and a switching profile similar to the case of sample A (CoFeB) was observed. At the static field of H_b = 8.1 Oe, no switching was seen in sample B, even at the highest microwave power of 30 dBm. When the static field was then increased to H_b = 10.5 Oe as shown in

Fig. 5-8(b), clear microwave-assisted switching was observed at P_{inp} = 11.57 dBm. However, signatures of partial switching behavior were seen both before and after P_{inp} = 11.57 dBm. At H_b = 16.4 Oe, the static field contributions were strong enough to switch below P_{inp} = 5 dBm, as seen in Fig. 5-8(c).

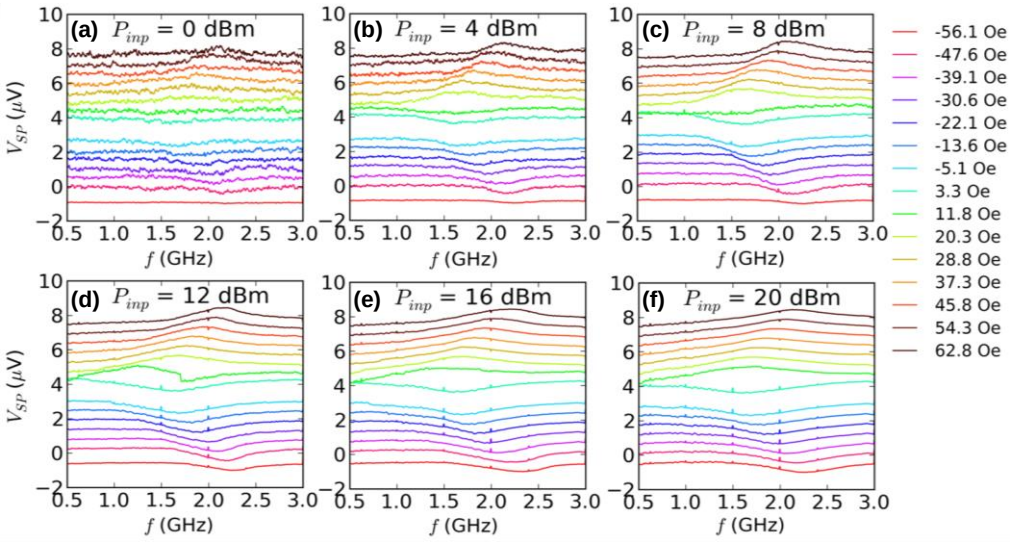

Figure 5-7: (a-e): Change in the effective coercivity of the Py layer in sample B is seen as the microwave power is gradually increased, at different values of the bias field. The microwave power is swept from 0 dBm to 20 dBm in steps of 1 dBm. The data shown here is a characteristic data set as the changes due to microwave excitation is very small for consecutive increments in power. The abrupt jumps in the spin pumping voltage from P_{inp} = 14 dBm onwards indicate the onset of reversal.

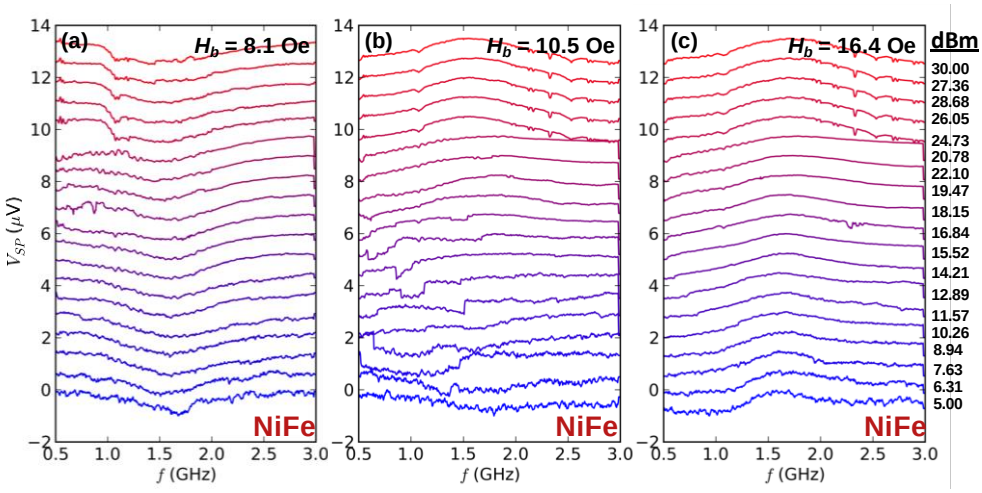

Figure 5-8: (a) – (c) Switching characteristics of the NiFe layer in sample B for different values of the constant bias field. The microwave power is swept from 10 dBm to 20 dBm at each bias field to study the switching behavior. (a) shows no reversal for any power, while (b) shows a switching profile at P_{inp} = 11.57 dBm onwards. Figure (c) shows that the magnetization has already switched even for the minimum power used.

5.8 Energy profile diagram of MAMR and the conditions for switching

The reversal mechanism can be discussed as a result of the competition between the injected energy and damping energy in a system with microwave excitation. The external static bias field reduces the energy barrier height between the two stable magnetization states, and the absorption of energy from the microwave field causes the precessing magnetization to climb up the energy well and arrive at the threshold point, as shown in Fig. 5.9. Considering a perturbative approach [70], the magnetization in a single domain is assumed to be precessing with no damping as it is taken into account as a separate energy contribution. If the magnetization is precessing with the same angular frequency as the microwave excitation in a given precessional mode, then the reversal is determined by competition between the injection and damping energies. If the injection process is dominant, a

particular amount of energy is coupled to spin wave excitations [159, 205] and this makes the precessional mode unstable, resulting in a change of the precessional path to a different cone angle. Depending on the values of the Gibbs free energy, the injection, and damping energies of the system, the magnetization will surmount the energy barrier and fall in the other energy well, thereby achieving magnetization reversal. In a multi-domain model, the effect of microwaves on magnetization reversal is initiated by domain nucleation as seen in our experiments. This is followed by a reversal process similar to the single domain model, but with additional interactions between domains due to spin wave modulations and domain wall dynamics.

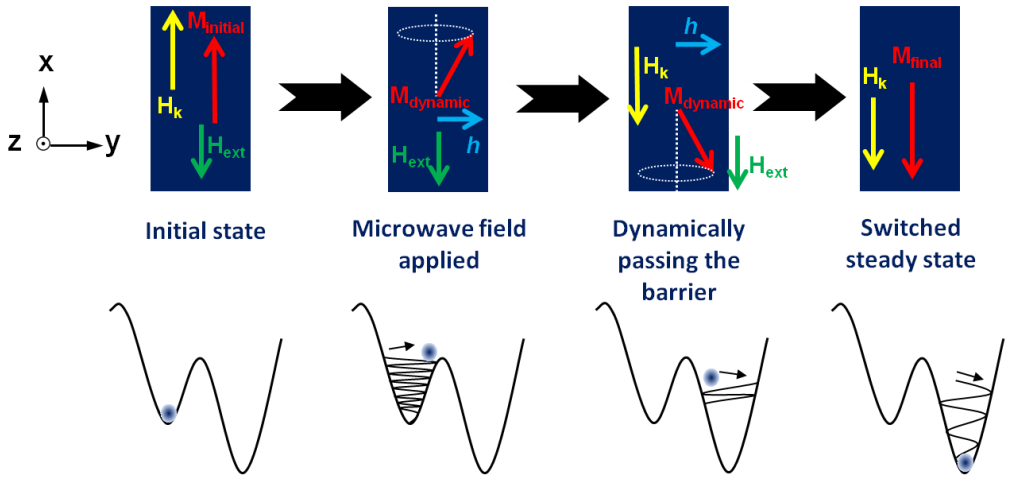

Figure 5-9: Evolution of the magnetization in the FM material from one stable energy state to the other. The increase in the potential energy of the initial state is due to the application of the static bias field (H_{ext}) in a direction opposite to the magnetization ($M_{initial}$). H_k is the shape anisotropy of the film under consideration and $\boldsymbol{h}$ is the applied microwave field.

5.9 Conclusions

We have presented a new technique of characterizing MAMR driven by the spin pumping phenomenon. This technique is able to provide a quick and accurate picture of the reversal mechanism in the magnetic structure,

regardless of material parameters and geometric features. A qualitative understanding of the factors governing the reversal mechanism, specifically the competition between the injection and damping energies, is presented for both single domain and multi-domain models. The interaction between domains through spin wave modulations and domain wall dynamics is an important criterion for multi-domain switching, and requires more in-depth research to quantify their contributions. This technique can also be used to characterize granular films and their switching modes – a practical concern in reaching the goal of high areal densities greater than 1 Tb/in^2.

Chapter 6: Direct imaging of microwave-assisted magnetization reversal in patterned elements

6.1 Motivation

Since its first demonstration in 2003, research in MAMR has covered a lot of ground in measurement techniques, device design, novel materials study and recently, commercial media materials. These materials require an excitation frequency in the range of 20 – 40 GHz and at high powers (> 25 dBm), making them highly unfeasible for current applications. Hence, the need is to switch real media materials, while maintaining lower frequencies of microwave excitation.

In this chapter, we study the microwave-assisted reversal behavior of patterned sub-micron magnetic elements in a time-resolved setup. By analyzing the reversal mechanism of the element, we are able to reveal that propagating spin waves are the dominant forces in the reversal process and are also at thrice the frequency of the microwave excitation. We observe that shape effects play a significant role in generating higher order spin wave modes that seem to drive the reversal process. Thus, we present a new technique that can be used to overcome the issues stated above.

6.2 Introduction

Experiments on MAMR have primarily been carried out by ferromagnetic resonance (FMR) experiments using a vector network analyzer (VNA) [76-78], or by the magneto-optic Kerr effect (MOKE) [80, 81]. In VNA-based experiments, by simultaneously applying the static and

microwave-generated magnetic fields and sweeping the microwave frequency, it is possible to identify the natural resonance frequency of the magnetic structure at which the switching process is most efficient [76]. These techniques have been used to study MAMR in commercial media materials such as CoCrPt [77-79, 206-208]. However, the best result on CoCrPt till date is the approximately 30% reduction in the coercive field at an applied power of 25 dBm (~316 mW) [78], which requires designing a high power microwave source in the write heads for HDD applications.

To overcome the problems posed by high coercivity PMA materials, it is necessary to understand the physics involved in a MAMR process. Despite the extensive literature available on the phenomenon of microwave-assisted switching, the factors that govern the mechanism of reversal and the exact role of the microwaves are still under debate. The most complete understanding till date has been limited to the single-domain model as studied by Thirion *et al.*[69] in switching Co nano-particles. However, in larger elements, and the geometries and anisotropies relevant for applications, the dynamical magnetization is inhomogeneous and hence follows a more complex and incoherent switching process. Time-resolved techniques are an efficient tool in mapping such magnetization dynamics due to their high temporal resolutions (< 500 ps). Most MOKE-based time-resolved studies have very good temporal resolutions (tens of picoseconds and lower); however, the limited spatial resolution often does not allow for the identification of the switching processes. The photoemission electron microscopy (PEEM) and scanning transmission X-ray microscopy (STXM) techniques possess the necessary temporal and lateral resolution to identify intermediate switching states.

In this chapter, we look at the microwave-assisted switching mechanism in elliptical permalloy elements and study the switching dynamics using micromagnetic simulations and Fourier analysis. Spin waves along the field direction are shown to initiate the reversal and generate additional spin wave modes, fundamental and edge-mode, which are dominant throughout the reversal process.

6.3 Experimental Methods

The substrates used for this study were 75 nm thick silicon nitride (SiN_x) membranes. The thin film stack with a composition of $Ni_{78}Fe_{22}$ (30 nm) / Ta (2 nm) was grown in a magnetron sputtering chamber with a base chamber pressure of 2×10^{-9} Torr. The Py elements were patterned into 4×0.4 μm^2 elements by electron-beam lithography and lift-off processing. Following lift-off, 4 μm-wide linear striplines were defined by photolithography on top of the magnetic elements. Contact pads with a composition of Ta (5 nm)/Cu (150 nm) were sputter-deposited, followed by lift-off processing.

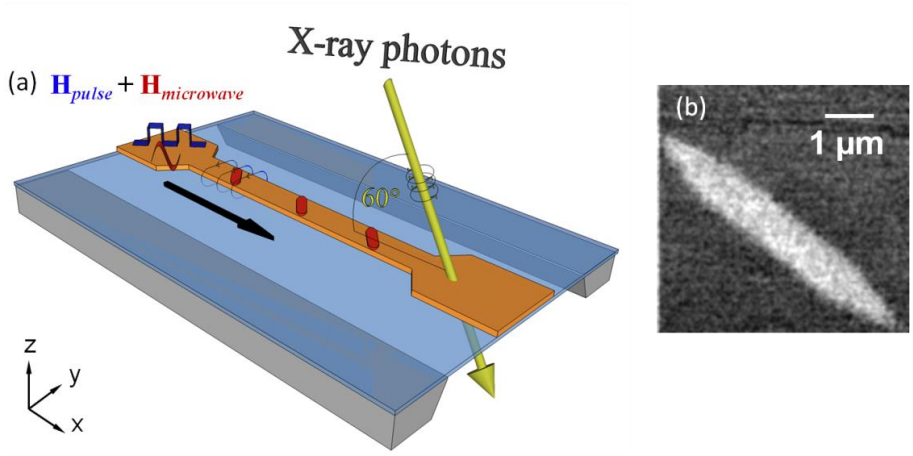

Figure 6-1: (a) Schematic of the sample used for STXM experiments. The ferromagnetic elements are shown here on top of the stripline for clarity. The current pulse through the stripline is a superimposition of a microwave signal and a square pulse to generate the microwave-assisted dynamics. (b) Differential XMCD image of the ferromagnetic element.

Figure 6-1 shows a schematic diagram of the sample in the experimental configuration. Soft X-rays in the energy range of 2 keV were transmitted through on the sample and collected on the other side by a photodiode. The in-plane component of the magnetization was dynamically imaged by employing time-resolved scanning transmission X-ray microscopy (STXM) using the pump-and-probe technique. Magnetic contrast was obtained by taking advantage of the X-ray magnetic circular dichroism (XMCD) [147]. The data were recorded at the L_3 absorption edge (852.7eV) of the Ni atom. The sample was tilted by 30° with respect to the X-ray beam to measure the m_x and m_z components of the magnetization with a spatial resolution of 25 nm. Given this configuration, it is not possible to obtain any information on m_y. The magnetic response to the external field was imaged by the individual photon flashes of the synchrotron, with a time resolution of 166 ps. A fast digital pulse generator and a signal generator in combination with a frequency mixer were used to inject rectangular pulses (pulse of 2 ns duration, and rising and falling times of ~ 300 ps), superimposed with sine wave burst pulses (pulse width of 4 ns) through a stripline to generate the in-plane magnetic field burst pulses. The field strengths were calculated from the currents and had an estimated systematic error of ~ 10 %. In order to increase the signal-to-noise ratio and yield reasonable dynamic contrast, the sample was measured for several million excitations per pixel. The structure was excited at a repetition rate of 12 MHz in order to record one series of time-resolved images.

6.4 Direct dynamic imaging of microwave-assisted magnetization reversal

The elliptical elements considered for imaging were aligned at 45° to the current-carrying stripline, as shown in the sample schematic in Fig. 6-1(a). This was done to maximize the output signal measured due to oscillations in the m_x component of the magnetization, as opposed to the conventional arrangement of the element along the stripline. The latter case would result in oscillations primarily along the m_y component, which cannot be measured in our experimental configuration. Figure 6-2 shows the current excitations in the stripline which consists of a unipolar square pulse of 2 ns duration superimposed on a 4 ns long, 1.8 GHz sinusoidal microwave input pulse with a 1 ns offset in time, as seen in Fig. 6-1(b). The Oersted fields generated due to both the unipolar square pulse and the superimposed microwave signal are along the y-axis. Therefore, the initial state destabilizing magnetization dynamics occurs primarily along the y-axis. The static field applied during this process was -75 Oe and the microwave field was 30 Oe peak. The black and white contrast in Fig. 6-1(b) corresponds to the direction of the magnetization along the *x*-axis of the element.

Figure 6-3(a-f) shows the time evolution of a typical reversal process in the element measured experimentally with both the square static and microwave fields. In the experiment, $t = 0$ is defined as the time of the onset of the 4 ns-long microwave pulse. The square pulse is turned on at $t = 1$ ns and reaches its maximum value at $t = 1.3$ ns. Thus, Fig. 6-3(a) indicates the state of the element before switching at $t = 1.27$ ns, followed by domain nucleation at the foci of the elliptical element at $t = 1.44$ ns, as seen in Fig. 6-3(b).

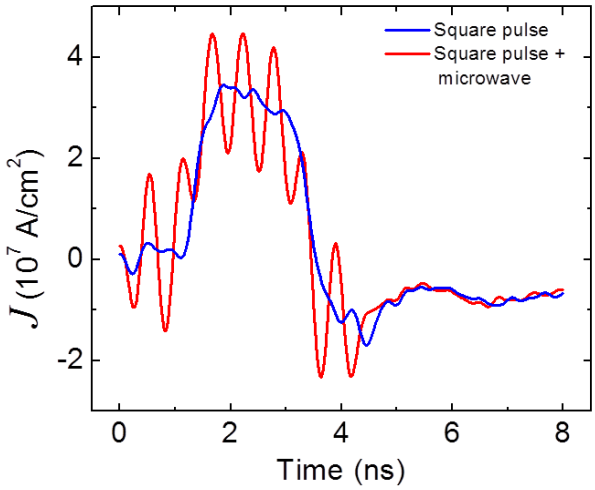

Figure 6-2: A 4 ns, 1.8 GHz microwave signal superimposed on a 2 ns square pulse. Due to reflections from the measurement equipment, the microwave signal is seen to extend up to 6 ns.

The formation of the taper angle of the domains is influenced by both the shape-dependent demagnetizing field in the element and the 'instability regions' formed as a result of spin wave creation and propagation [209]. These domains gradually undergo relaxation and expansion processes as seen at t = 1.77 ns in Fig. 6-3(c). The sequence of the domain expansion processes seen in Fig. 6-3(e-f) indicates that the element does not follow a uniform, coherently precessing switching model. The edges of the element remain unswitched until t = 2.43 ns in Fig. 6-3(e) and reverse only at the end of the square pulse. This can be attributed to the significantly higher demagnetizing field at the edges of the element. A unique 'S'-shaped magnetic domain feature was also detected as seen in Fig. 6-3(d). To confirm that such a magnetic domain feature was not due to surface defects created during the fabrication process, micromagnetic simulations were performed to confirm the switching sequence. This will be discussed in the following section.

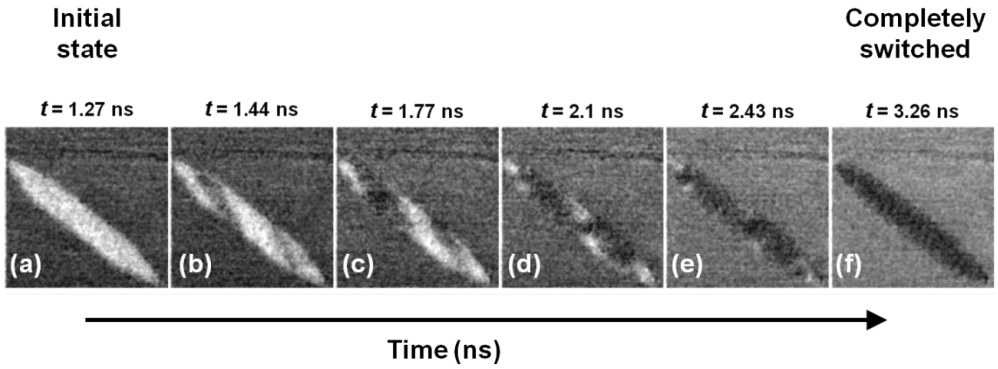

Figure 6-3: (a-f) Time-resolved images of a reversal process. The jitter of the experiment is ± 25 ps.

In order to demonstrate that the assistance of the microwave pulse is significant in switching the element, a set of control experiments were performed. In the first control experiment, only the square pulse excitation was applied to the stripline without the microwave excitation. The current pulse flows along the *x*-axis (from left to right), and the Oersted field is generated along the –*y*-axis. Figure 6-4(a-f) shows the time-resolved images of the magnetic element at different time instants after the application of the square pulse at t = 1 ns. Clearly, the element undergoes partial switching along the foci of the element; however, once the pulse excitation is removed, the domains gradually annihilate and the element relaxes back to its initial state.

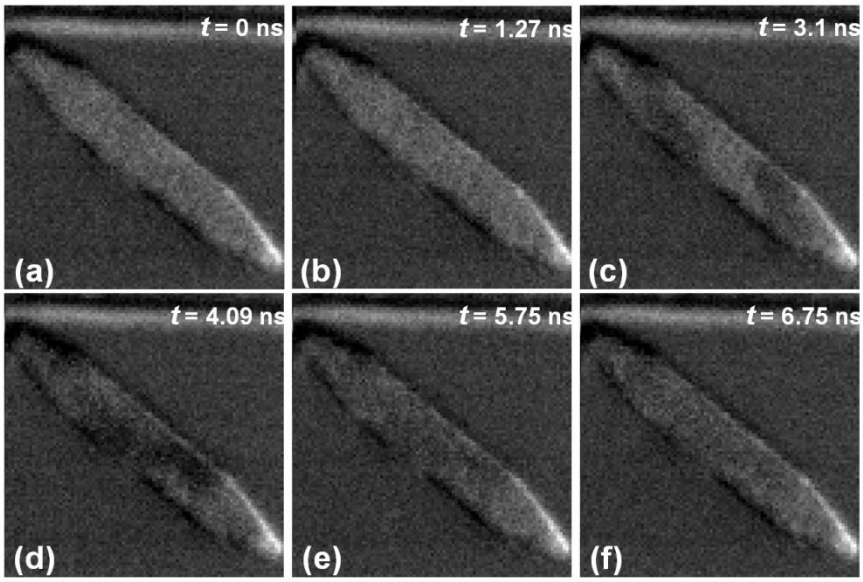

Figure 6-4: (a-f) Time-resolved images of a reversal process with only square pulse excitation.

In the second control experiment, only the microwave excitation was applied to the stripline and we see that a very weak excitation was generated in the element as shown in Fig. 6-5(a-c). A full switching was not possible in this case either. These control experiments confirm that a full switching is only possible with the help of a microwave pulse on top of a static field.

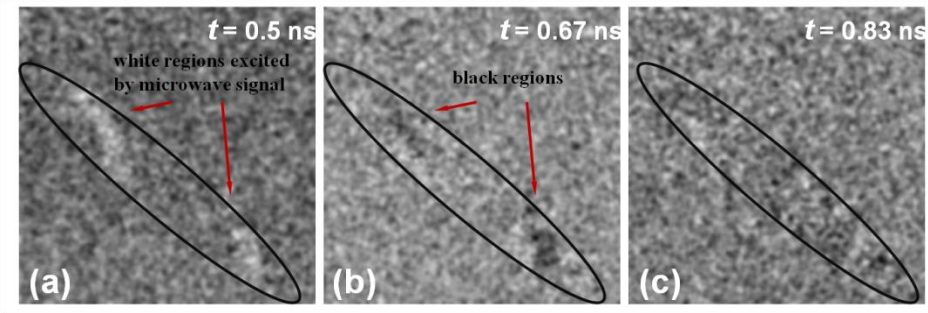

Figure 6-5: (a-c): Time-resolved images of weak magnetization dynamics under the influence of only a microwave current excitation without the square pulse. The weak changes in contrast are indicated by the red arrows and no switching occurs.

Due to the grainy background of the time-resolved images, it is difficult to extract any useful information by Fourier analysis of the image files. To

overcome these difficulties, micromagnetic simulations were performed to replicate the switching behavior seen experimentally.

6.5 Micromagnetic simulations of microwave-assisted reversal experiments

The micromagnetic simulations were carried out with the object oriented micromagnetic framework (OOMMF) [210]. We chose a cell size of $10\times10\times30$ nm^3 such that the minimum cell size is in the same order as the exchange interaction length of Py (~4 nm). Standard material parameters for Py were used in the simulations such as the saturation magnetization M_s = 860×10^3 Am^{-1}, exchange stiffness $A = 1.3\times10^{-11}$ Jm^{-1}, zero magnetocrystalline anisotropy, and a damping constant α = 0.001. The images of the spatial variation of m_y magnetization were plotted using a Python code and Endthought's Pylab shell. The simulated images shown in Fig. 6-6(g-l) are plots of the magnetization in the m_x and m_z directions only. This was done to ensure maximum correlation between the experimentally measured and simulated data.

Even though micromagnetic simulations cannot include magnetic and surface defects that contribute to domain pinning effects and other non-uniformities in the switching sequence, the presence of the 'S'-shaped magnetic domain feature in both experiments in Fig. 6-6(d) and the simulation in Fig. 6-6(j) confirms that the underlying phenomena are similar in both cases. Thus, a clear correlation is obtained between the experimental findings and the micromagnetic simulations to justify further analysis on the simulated data. To further visualize the switching process, Fig. 6-7(a-f) depicts the same

simulated switching sequence in a different color scale to enhance the contrast between the domains, with arrows to indicate the direction of magnetization.

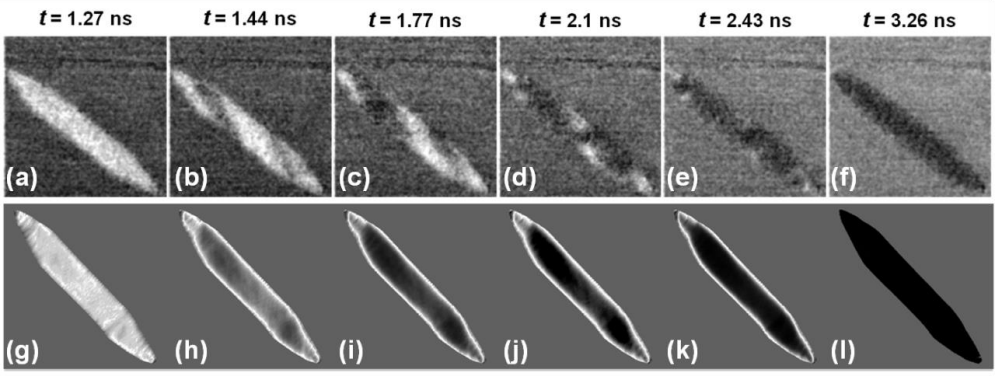

Figure 6-6: (a-f) Time-resolved images of the switching process obtained experimentally. They are shown here for ease of correlation with simulation results. (g-l) Images of the magnetization reversal obtained by micromagnetic simulations of a microwave-assisted reversal process. The images are shown in the exact time sequence of the switching process. The color scale used is white-gray-black corresponding to the experimental contrast.

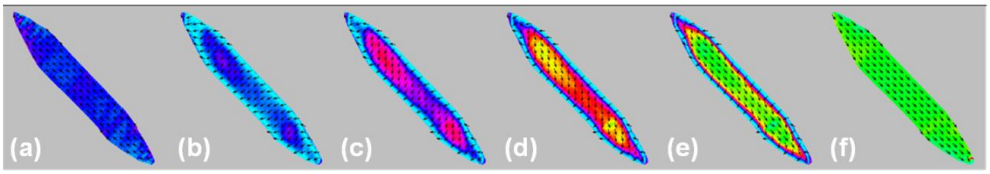

Figure 6-7: (a-f) Simulated images of the reversal sequence with arrows indicating the instantaneous direction of the magnetization. The reversal initiating fluctuations can be seen at the tapered ends of the elements in (a), while the domains nucleate first at the foci of the element in (b).

6.6 Fourier analysis in the spatial domain

6.6.1 Spatial variation of the demagnetizing field

The initiation of the switching has been previously [209, 211] attributed to the formation of instability regions as mentioned earlier, and the origin of these instabilities comes from spin wave generation. However, it is unclear to what extent spin wave generation assists in nucleation and magnetization reversal. Spatially resolving the simulated magnetization dynamics in the *k*-space highlights the contributions of spin waves at different

stages during the reversal, and the frequency domain analysis reveals the frequencies associated with these spin waves. The origin of the spin wave generation of different modes lies in the tapered shape of the magnetic element. In our elliptical elements, the demagnetizing field has a spatial variation due to the fact effective field required to switch the material is different at different regions of the element. The demagnetizing field across the element is determined by simulations. The element is saturated along its easy axis in the initial state and allowed to relax for 5 ns. Figure 6-8(a-c) shows the components of the demagnetizing field in the *x*, *y*, and *z*-directions. In particular, the field is weak near the foci of the element in the *x*- and *y*-directions, and very strong in the *z*-direction. This suggests that the magnetization reversal is an in-plane process.

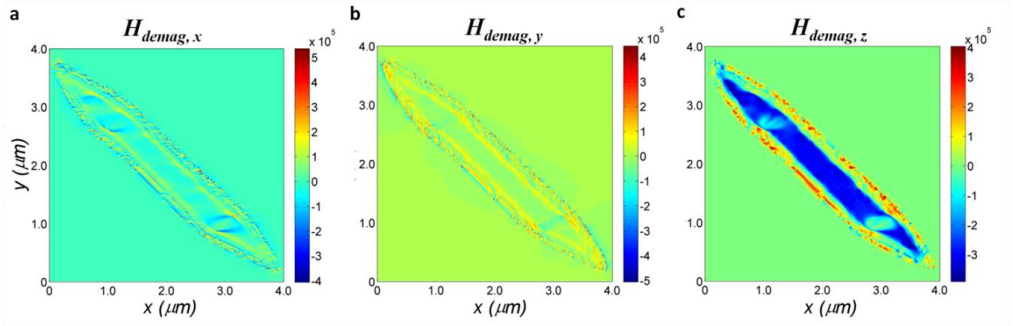

Figure 6-8: Spatial variation of the demagnetizing field across the elliptical element. (a) Component of the demagnetizing field along the *x*-direction. (b) Component of the demagnetizing field along the *y*-direction. (c) Component of the demagnetizing field along the *z*-direction.

6.6.2 Effects of precessional dynamics on spatially-resolved FFT plots

Under the influence of additional Oersted fields due to the currents in the stripline, there is a variation in the effective field across the element, and this generates different precessional frequencies across the element as well as spin waves along the hard axis, as confirmed by our fast Fourier transform

(FFT) results discussed below. The precession of the spins, under the influence of the microwave excitation, leads to a time-varying nature in the temporal response of the magnetization in the *x*, *y* and *z*-directions, as shown in Fig. 6-9(a,b). We can see a clear time-varying nature in all three components just after the square pulse is turned on (~ 1.3 ns) and near the end of the reversal process (3.3 ns). The points chosen in the following spatially-resolved FFT analysis are marked in the appropriate locations by star symbols. This oscillation in the magnetization signals primarily contributes to the strength of the signal seen in the spatially-resolved FFT plots in Figs. 6-11, 6-12 and 6-14. After the switching process is complete (~ 3.3 ns), we see a relaxation frequency in Fig. 6-9(a) that is calculated to be ~6.7 GHz.

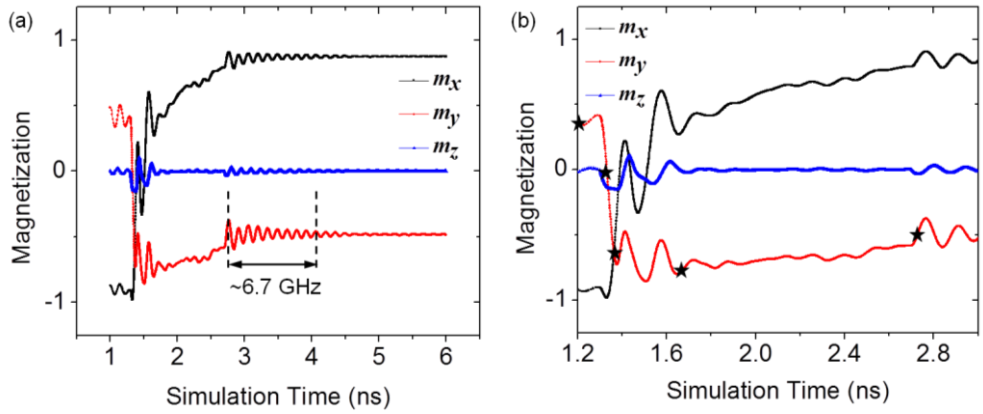

Figure 6-9: (a) Change in the normalized magnetization m_x, m_y, and m_z with simulation time. (b) A closer look for the time period between 1.2 ns and 3 ns. The time instants chosen for analysis in Fig. 4, 5, and S1 are indicated by black star symbols.

6.6.3 Fourier analysis in the spatial domain over the entire element – bulk and edge effects

To understand the dynamical processes driving the reversal mechanism, a Fourier analysis of the simulated data is performed. Owing to the noisy background in the experimental data, Fourier analysis reveals few

features of note. As we have already seen a good correlation between experimental and simulated results, further Fourier analysis in the sections below are performed solely on the simulated data. The objectives of this study are to analyze the frequency components that drive the reversal process. In a general case, the magnetization precession is expected to be driven at the frequency of the microwave. However, we hypothesize that due to shape-dependent demagnetizing field in the element, the precessional frequencies can vary across the element giving rise to spin wave behavior. To prove our hypothesis, FFT analysis has been carried out and discussed below. We will show that higher frequency spin wave modes can be excited by lower frequency microwaves, and these spin waves are the dominant driving mechanism in MAMR of patterned elements.

Figure 6-10(a-f) shows the spatial FFT plots plots of the measured magnetization signal of the entire element at different instants of time during the reversal process. Comparing the *k*-space plots with the physical orientation of the element in Fig. 6-3(a), it is clear that the strongest dynamics are seen along the hard axis of the element. This can be understood as the initial magnetization is oriented along the easy axis and the microwave excitation tends to cause a precession around the easy axis giving rise to magnetization fluctuations in the hard axis direction. The presence of high intensity peaks along the hard axis, passing through the central region ($k \sim 0$), of the plots agrees with the theory [212] that different fundamental ($k = 0$) and spin wave modes ($k \neq 0$) are excited across the element. In addition, a closer look at Fig. 6-10(c) shows the presence of two faint lines originating from (k_x, k_y) = (-0.15, -0.18)×($4\pi \times 10^7$ m^{-1}) and (-0.18, -0.15)×($4\pi \times 10^7$ m^{-1}), respectively. A

comparison of these plots with the spatial FFT plots from simulated data in the following sections will confirm that the line features are due to spin wave dynamics excited at the border locations of the element. Thus, it can be seen that several fundamental and higher order spin wave modes are excited in the element due to the microwave signal.

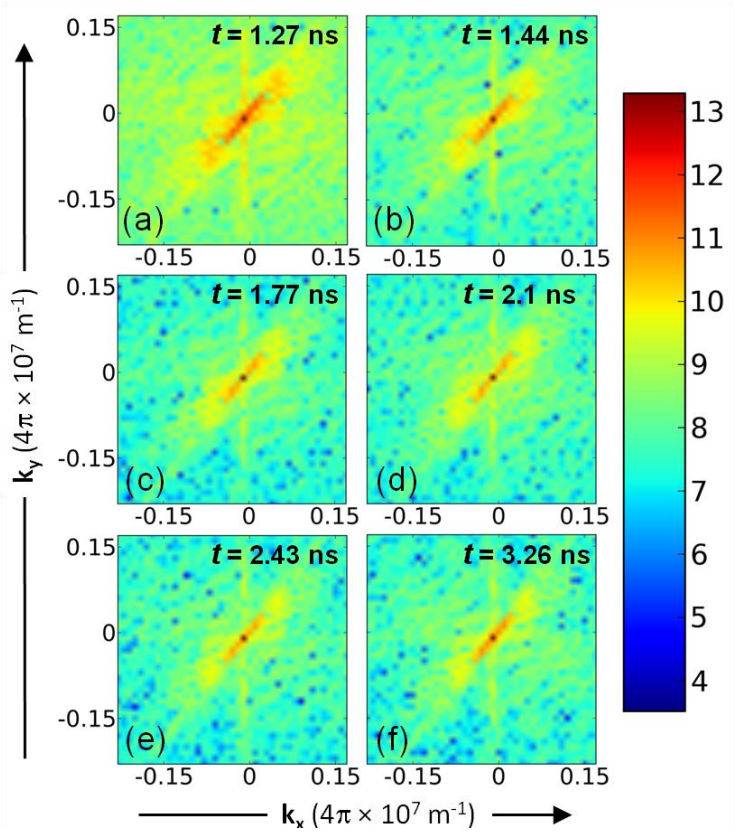

Figure 6-10: (a-f) Spatially resolved FFT plots of the measured magnetization signal over the entire element at different time instants of the switching process.

Figure 6-11(a,b) shows the spatial FFT plots of the magnetization of the entire element at different instants of time during the reversal process, along the *x*- and *y*-axis, respectively. Comparing the *k*-space plots in Fig. 6-11(a,b) with the images of the element in Fig. 6-12, it is clear that the strongest dynamics are seen along the hard axis of the element. This can be understood as the initial magnetization is oriented along the easy axis and the microwave

excitation tends to cause a precession around the easy axis, giving rise to fluctuations in the hard axis direction. The presence of high intensity peaks in the central region (k ~ 0) of the plots agrees with the theory [212] that different fundamental and spin wave modes are excited across the element. Thus, it can be seen that the spatial FFT data of experiment and simulation match well with each other, confirming the existence of multiple spin wave modes. The additional features seen in simulations along the axes of the element is due to an increased spatial and temporal resolution.

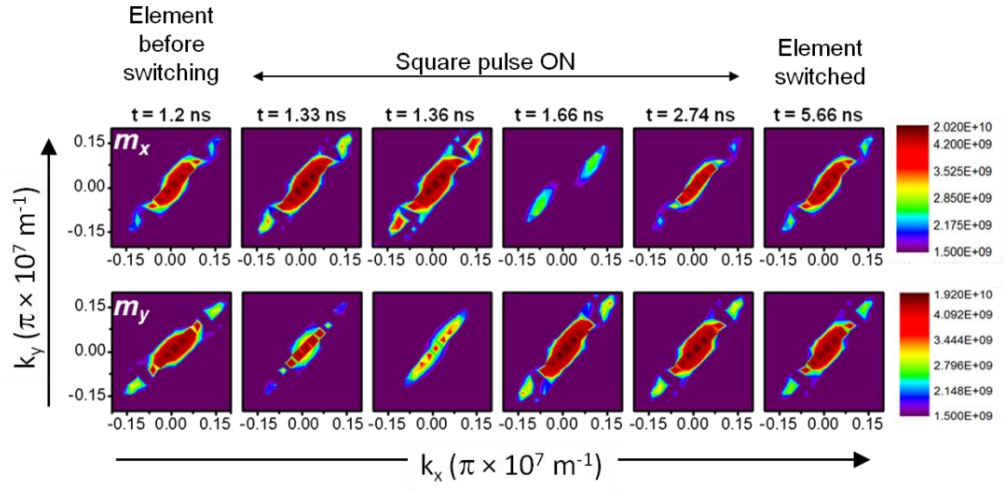

Figure 6-11: (a) Spatially resolved FFT plots of the simulated magnetization m_x over the entire element at different time instants of the switching process. (b) Spatial FFT plots of the simulated magnetization m_y over the entire element.

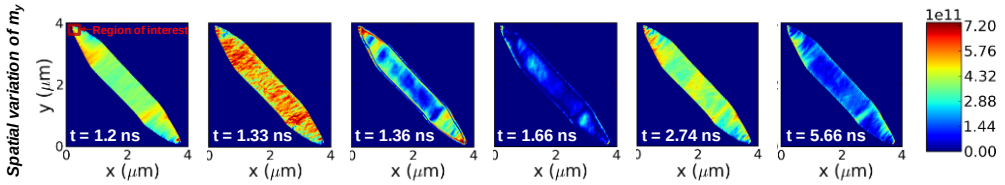

Figure 6-12: Spatial variation of m_y across the element obtained from simulations. Note the thick blue line along the border locations of the element at t = 1.36 ns, indicating possible pinning effects at these locations.

To identify the physical origin of the features along the direction of the hard-axis of the element, spatial FFT plots of the border locations of the

element were performed. Fig. 6-13 shows the regions along the edges of the element considered for this analysis, while the results are shown in Fig. 6.14(a-c).

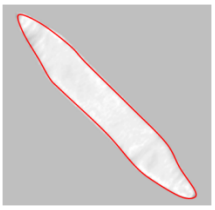

Figure 6-13: Points chosen for spatial FFT along the border regions of the element are indicated by the red line.

The clear line features along the hard axis direction confirm that the excitation of spin waves is mostly along the hard axis and is initiated at the border locations. Compared to line-shaped features in Fig. 6-14, the expanded features in Fig. 6-11(a,b) in the direction of the easy axis of the element are due to the excitations interior of the element. Due to the magnetization oscillations seen in Fig. 6-9, we observe the weaker intensities seen at t = 1.66 ns in Fig. 6-11(a) and at t = 1.36 ns in Fig. 6-11(b).

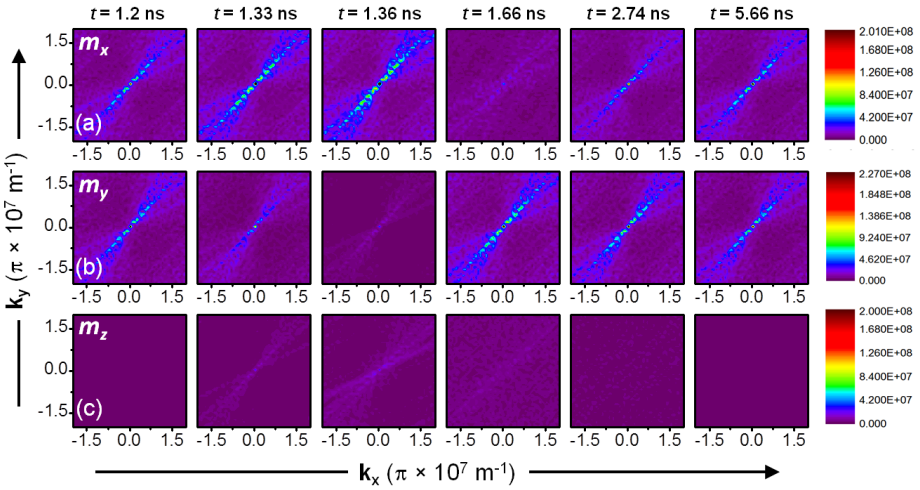

Figure 6-14: Spatial FFT plots of the magnetization at different time instants of the switching process along the x, y, and z-directions. The points for the FFT process were chosen along the edges of the element. (a) Spatial FFT plots of m_x. (b) Spatial FFT plots of m_y. (c) Spatial FFT plots of m_z.

6.6.4 Fourier analysis in the spatial domain in a confined area of interest

It can be seen from Fig. 6-7(a) that the reversal-initiating spin waves are generated from the end of the element, therefore further analysis has been conducted for the area indicated by the red box in Fig. 6-12 defined as the 'region of interest'. Figure 6-15(a,b) presents the spatial FFT plots for the m_x and m_y in this region, and Fig. 6-15(c) shows the spatial variation in m_y in this region. The spatial FFT plots in Fig. 6-15(a,b) for t = 1.2 ns show a central peak intensity node around k_x, k_y ~ 0 consisting of different k values. These peak intensity nodes represent fundamental modes. In addition, given that the non-zero k values around the peak correspond to spin wave excitations, we can see that the fundamental mode co-exists with spin waves that decay in a radial fashion away from the zone center (k = 0). We also observe faint spin wave modes further away from the peak intensity along the k_y = 0 axis (indicated by blue tails in Fig. 6-15(a,b)), which could be the edge effects present in patterned elements [213].

To identify the origin of the blue tails seen in Fig. 6-15(a,b), we used the spatial FFT technique in a secondary region next to the 'region of interest'. Fig. 6-16(a-c) shows the m_y data at t = 1.33 ns in the two regions. We can clearly see that there is a shift in the k_y = 0 line from the edge 'region of interest' to along the $k_y = \pm 0.5\times(\pi\times 10^7)$ m^{-1} lines in the 'secondary region'. We also observe that the intensity of the tail dynamics (comparing Figs. 6-16(b) and 6-16(c)) drops significantly within a range of 200 nm (dimensions of the white box in Fig. 6-16(a)). This confirms that the dynamics represented by the blue tails are a signature of the edge regions of the element.

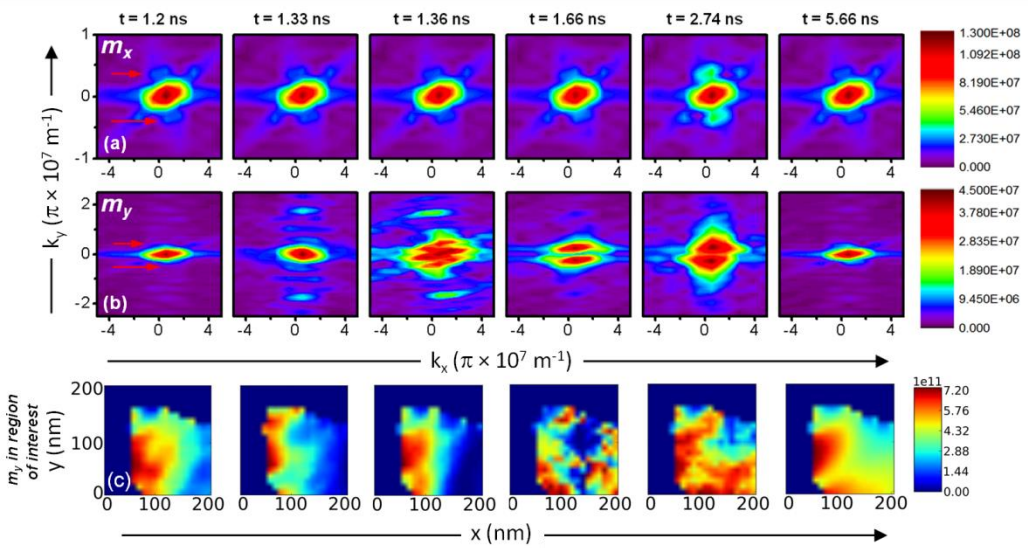

Figure 6-15: Spatial FFT plots of the simulated magnetization (a) m_x and (b) m_y in the region of interest as indicated in (c) at different time instants of the switching process. Note the different scales in the *y*-axis. (c) The region of interest chosen is a 200 nm × 200 nm region at the tapered end to the top left of the element.

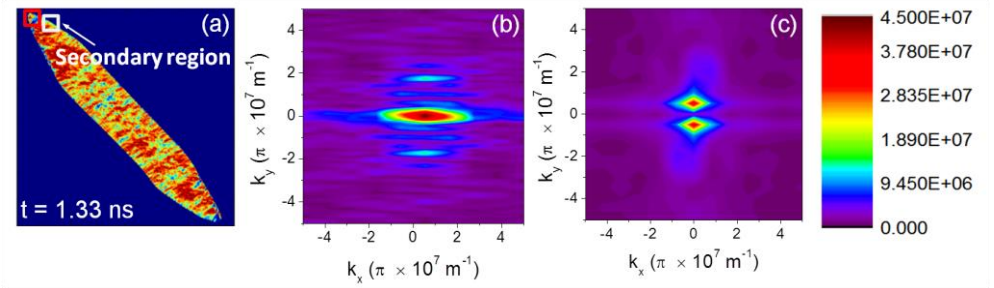

Figure 6-16: (a) The 'region of interest' is indicated by a red box, while the 'secondary region' considered here is indicated by the white box. We show the spatial FFT plots of m_y at t = 1.33 ns in both the (b) red and (c) white regions.

The presence of easy-axis spin wave dynamics is shown by the features (indicated by the red arrows) in all the plots of Fig. 6-15(a), where the direction of the features extends along the direction of the easy axis of the magnetic element. At t = 1.33 ns when the square pulse excitation is at its steady state value, we see new peaks along k_x = 0 in Fig. 6-15(b), which correspond to the spin wave propagation along the *y*-direction under the influence of the effective magnetic field from the square pulse. In the next

time instant (t = 1.36 ns), the spin wave behavior is even more pronounced with the widening and splitting of the central peak into a range of k values.

As evidenced by a thick blue line in the image in Fig. 6-12 for t = 1.36 ns, the magnetization along the border of the element does not follow that of the rest of the element and remains oriented along the edges. These border locations give rise to edge-mode spin waves that propagate towards the central regions of the element, creating a complicated magnetization picture. The expansion of the high-intensity regions along the easy axis in Fig. 6-15(b) also points to the existence of multiple spin wave modes at the end of the element. At t = 1.66 ns, we see a gradual decay in the variety of spin wave modes in the element, leaving only two dominant modes at $(k_x, k_y) = (0, \pm 0.2)\times(\pi\times 10^7)$ m^{-1} in m_y. At t = 2.74 ns, we see a subsequent increase in dynamics for both m_x and m_y. This is again due to the oscillating nature of the overall magnetization dynamics as described earlier. Once the element has been switched and undergoes slow relaxation, we see that the spatial FFT intensity at t = 5.66 ns returns to the initial state. The significant shift of major excitations in FFT plots with time in Fig. 6-15(b) is further proof that propagating spin waves dominate the efficient nucleation and reversal process.

As mentioned before, the fundamental mode or the natural resonance frequency of the element is also excited by the microwave field pulse. Previous studies have attributed microwave-assisted switching to the phenomenon of switching at ferromagnetic resonance [73], but not considered the effect of higher order spin wave modes. To prove the contribution from spin waves, the energy distribution between the (k = 0) fundamental mode and the ($k \neq 0$) spin wave modes was calculated. This was done by considering a

circular region that encloses the (k = 0) mode, and integrating the square of the intensities in the spatial FFT plots within this region as shown in Figs. 6-17(a,b).

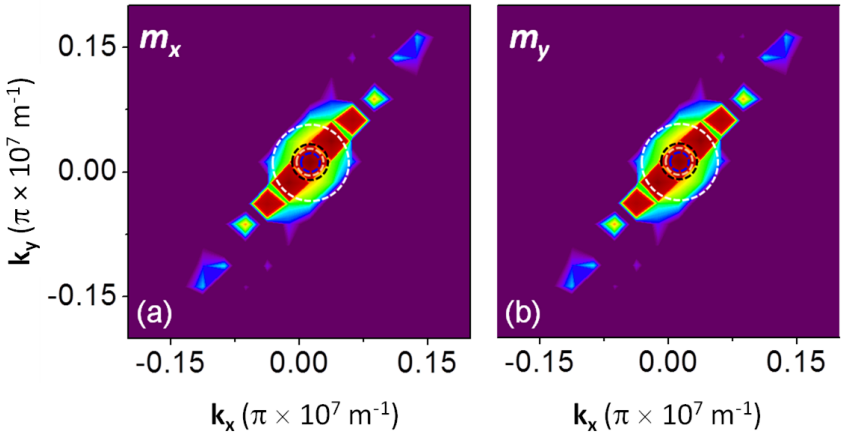

Figure 6-17: Spatial FFT plots of the magnetization (a) m_x (b) m_y over the entire element at an arbitrary time instant. The dotted lines of different colours indicate the different radii chosen to calculate the energy distribution between the fundamental and spin wave modes. The values of the radii are summarized in Tables 6-1 and 6-2 below.

The radius of the circular region chosen is varied and the energy in the FMR or fundamental mode is calculated at different time instants in the reversal process. These data are summarized in Tables 6-1 and 6-2 below.

	← Radius of spot chosen →			
t	1×10^5 m^{-1}	1.5×10^5 m^{-1}	2×10^5 m^{-1}	4×10^5 m^{-1}
1.2 ns	2.15 %	4.84 %	6.92 %	9.80 %
1.33 ns	2.65 %	5.98 %	8.36 %	11.29 %
1.36 ns	2.50 %	5.62 %	7.88 %	10.72 %
1.66 ns	0.10 %	0.47 %	1.11 %	2.57 %
2.74 ns	1.31 %	2.88 %	4.14 %	6.01 %
5.66 ns	2.30 %	5.15 %	7.26 %	9.92 %

Table 6-1: Energy contained in the FMR mode (from radii of 1×10^5 m^{-1} to 2×10^5 m^{-1}) of the magnetization m_x at different times during the magnetization reversal process.

	← Radius of spot chosen →			
t	1×10^5 m^{-1}	1.5×10^5 m^{-1}	2×10^5 m^{-1}	4×10^5 m^{-1}
1.2 ns	2.41 %	5.47 %	7.57 %	9.9 %
1.33 ns	1.64 %	3.78 %	5.33 %	7.72 %
1.36 ns	0.82 %	2.4 %	4.2 %	7.3 %
1.66 ns	1.67 %	3.87 %	5.46 %	7.37 %
2.74 ns	2.15 %	4.95 %	6.9 %	9.06 %
5.66 ns	2.33 %	5.33 %	7.44 %	9.94 %

Table 6-2: Energy contained in the FMR mode (from radii of 1×10^5 m^{-1} to 2×10^5 m^{-1}) of the magnetization m_y at different times during the magnetization reversal process.

A radius of (4×10^5 m^{-1}) includes two high intensity spin wave modes on either side of the FMR mode as seen from Fig. 6-17. Therefore, we only consider radii of 2×10^5 m^{-1} and lesser as representative of the FMR mode. For different values of radii of the circular region, we find that the energy in the FMR mode was ~8% or less at all times of the reversal process. This proves that the FMR mode does not have enough energy to drive the magnetization reversal of the entire element. The energy contained in the entire plot was calculated similarly by considering a circular region with a radius of 1.6×10^7 m^{-1}, and was found to be ~96%. This confirms that the remaining energy (~88%) is distributed amongst several spin wave modes that in turn, drive the magnetization reversal. Thus, the contribution of spin waves to the reversal process dominates over that of the FMR mode.

6.7 Fourier analysis in frequency domain

To further substantiate that high-frequency spin waves are the main factor in the switching process, we carried out an FFT in the frequency domain of the points along the easy axis of the element.

6.7.1 Magnetization dynamics in the bulk regions

The analyzed location as shown in the inset of Fig. 6-18(b) passes through the magnetically-soft central regions of the element where the in-plane demagnetizing factor is the lowest. Therefore, any disturbance or dynamics would be maximized along this line. Figure 6-18(a) shows the FFT for the m_x, m_y, and m_z data for a total simulation time of 6 ns. The regions between points 75 – 125 and 225 – 275 represent the foci of the elliptically-shaped element. As expected, these regions show the highest intensity peaks at a frequency of ~5.6 GHz, which corresponds to the natural frequency in these regions. It is interesting to note that there are no high intensity peaks at frequencies below 2 GHz as seen from Fig. 6-18(b). Note that the peaks seen in Fig. 6-18(a) (m_x and m_y) for frequencies close to DC in regions between points 0 – 50 and 300 – 354 along the easy axis are due to the mathematical FFT operation. This shows that, contrary to previous literature reports, low frequency (< 1 GHz) dynamics such as domain wall dynamics are not as critical to the switching process as spin waves [211].

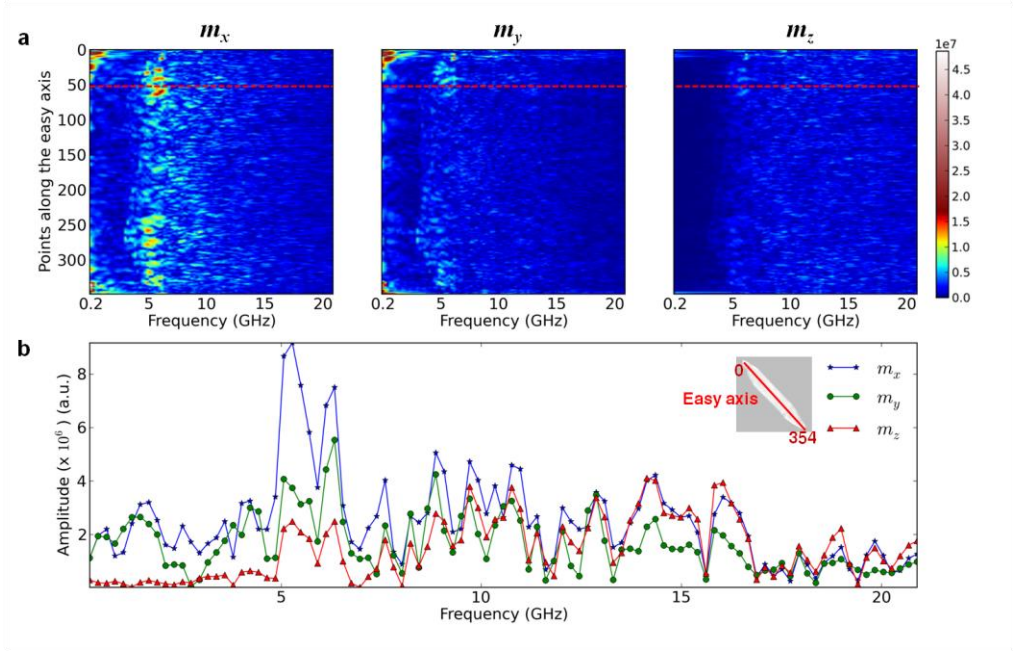

Figure 6-18: (a) FFT in frequency domain performed on the simulated data of the magnetization along the *x*, *y*, and *z* directions. The points for the FFT process were chosen along the easy axis of the element indicated by the red line in the inset of (b). (b) FFT in the frequency domain of the magnetization data at point number 50 on the easy axis of the element (denoted by red lines in a). The red line in the inset passing through the easy axis of the element indicates the 354 points for the FFT analysis.

6.7.2 Magnetization dynamics along the border regions of the element

As in the discussion of the spatially-resolved magnetization dynamics in the elliptical element, it is of practical significance to identify the frequencies of the spin waves that originate along the border regions of the element. The number of points considered for this analysis is the same as those considered for the time-domain analysis in the bulk regions of the element. There are 354 points along the edges of the element, with 177 points distributed from one tapered end of the element to the other, as shown in the inset of Fig. 6-19(b). Analyzing the frequency dependence data in Fig. 6-19(a), we see that m_x and m_y show a signature in the range of 5 – 10 GHz, with a peak at ~ 6.5 GHz in Fig. 6-19(b). This frequency is assumed to be the

frequency of the spin wave modes generated, while the signal at 10 GHz is relatively weak.

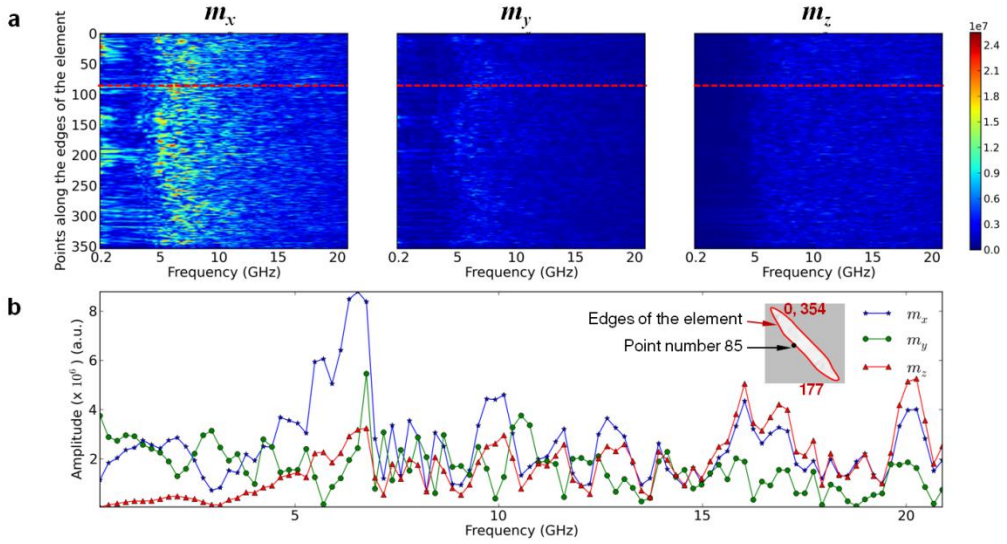

Figure 6-19: (a) FFT in frequency domain performed on the simulated data of the magnetization along the *x*, *y*, and *z*- directions. The points for the FFT process were chosen along the edges of the element indicated by red line in the inset of (b). (b) FFT in frequency domain of the magnetization data at point number 85 (denoted in the inset). Inset: The red line passing along the outer edge of the element image indicates the points that have been chosen for the FFT analysis. There are 354 points along this line.

6.8 Quantitative description of spin wave propagation characteristics

The spatial FFT plots in Figs. 6-10 and 6-11 show a wide distribution in the values of k_x and k_y around the peak intensity nodes, thus making it difficult to quantitatively describe or separate the dominant mode from the other spin wave mode frequencies. In this case, we consider the spin wave characteristics at t = 1.36 ns. We choose the k values for the main spin wave modes in Fig. 6-11(a). The wave-number k is calculated as: $k = \sqrt{k_x^{\,2} + k_y^{\,2}}$. Considering three sets of (k_x, k_y) values: (0.02, 0.005)×($\pi\times10^7$) m^{-1}, (-0.009, -0.12)×($\pi\times10^7$) m^{-1}, and (0.139, 0.136)×($\pi\times10^7$) m^{-1}, we obtain corresponding wavelengths (λ) of

10, 1.667, and 1.537 μm, respectively. Using the frequency of the dominant spin waves of ~5.6 GHz in Fig. 6-18(b), we estimate the spin wave velocity to be in the range of 8.6 – 56 km/s, which is in line with previously reported values [175, 214].

6.9 Conclusions

In summary, we have imaged – for the first time – microwave-assisted switching in patterned elements with sub-nanosecond temporal resolution. We further analyze the switching process in the *k*-vector and frequency domain, and show that propagating spin waves are the primary driving source of magnetization reversal. A thorough FFT analysis in the spatial domain reveals the presence of several fundamental and edge-modes spin waves, and a shift in the *k*-vector with time to highlight the propagating nature of the spin waves. Our results indicate that a high frequency (5.6 GHz) spin wave mediated switching can be induced by exciting low frequency (1.8 GHz) microwaves in a magnetic structure.

Chapter 7: Conclusions and future work

We have studied the magnetization dynamics associated with microwave-assisted magnetization reversal (MAMR) by electrical and optical characterization techniques. This paper has presented results that would be useful in the development of MAMR-based read/write technology to achieve ultra-high areal densities > 1 Tb/in^2 in hard disk drives (HDD).

Spin waves have been proposed as future solutions for high speed information processing applications and synchronization of STO-based read heads. To utilize spin waves, the spin wave propagation characteristics have been studied under an electrical square pulse excitation. The dynamic perturbation due to the pulse-generated Oersted field gives rise to multiple magnetostatic surface spin wave (MSSW) modes at the same location. These spin waves, with a clear frequency and phase difference, generate a beating interference pattern in the time domain. This interference study, which is distinct from previous mode interference studies in the *k*-space, was fitted with a mathematical model that shows good agreement with the experimental results. With external magnetic fields, we have shown that the non-reciprocal behavior of spin wave propagation can be tuned and this feature can be utilized for spin wave logic devices.

Characterization studies were also carried out on magnetic bilayer devices to investigate the MAMR process. By utilizing the spin pumping phenomenon and the inverse spin Hall Effect (ISHE) in a novel characterization methodology, the magnetization reversal was investigated through a change in the polarity of the measured ISHE voltage. The

microwave power dependence studies presented a clear signature and qualitative understanding of the switching process as it changes from a partial reversal at lower powers to a complete reversal at higher powers. Reversal studies on large micron-sized thin films of CoFeB and patterned arrays of NiFe microwires individually revealed a similar switching trend with microwave power, while the domain nucleation is clearer in the CoFeB sample. These results highlighted the feasibility of spin pumping-based characterization as a suitable tool for testing MAMR in different materials and aspect ratios.

We have also studied the MAMR process in smaller sub-micron patterned elliptical elements of NiFe by means of time-resolved X-ray transmission microscopy. From this study, it was found that spin waves not only initiate the reversal process, but also dominate the overall reversal regime while suppressing the contribution of other magnetization dynamics such as domain-wall dynamics. The results presented are the first time-resolved imaging of an MAMR process and they showed that the domain nucleation in the element is determined by the shape-dependent demagnetizing field. The reversal thus begins at the foci of the element, before expanding in the central regions and finally reversing at the tapered ends. Fourier analysis in the spatial domain revealed that the reversal-initiating spin waves are primarily oriented along the easy axis of the element, while the spin wave modes generated from the borders of the element are propagating along the hard axis. The *k*-space plots also revealed the propagating nature of these spin waves, as evidenced by the change in the position of the peak intensities. Frequency-domain analysis identified the spin wave frequencies at f = 5.6 GHz, and this

experiment presented an alternative methodology to implement MAMR in materials with very high resonance frequencies, such as CoCrPt and FePt.

Based on the research presented in this thesis and recent developments in the field of spintronics for magnetic data storage, a number of future works could be considered for further research as follows.

Characterization of MAMR reversal in future media material FePt with out-of-plane anisotropy

(a) Although spin pumping was sufficiently demonstrated as a feasible tool to characterize magnetization reversal in bilayer devices, this experimental configuration does not support the study of perpendicular anisotropy (PMA) materials. The spin pumping signal is given by $J_c = J_s \times \sigma$, where σ is the spin orientation, J_s is the spin current density, and J_c is the charge current density. Thus, for PMA materials it is necessary to study the spin pumping-mediated characterization in a lateral fashion, as shown in Fig. 7-1. Such a configuration can also be used to study the contribution to the measured DC signal due to spin rectification effects, aside from the contributions of ferromagnetic resonance to the spin pumping signal.

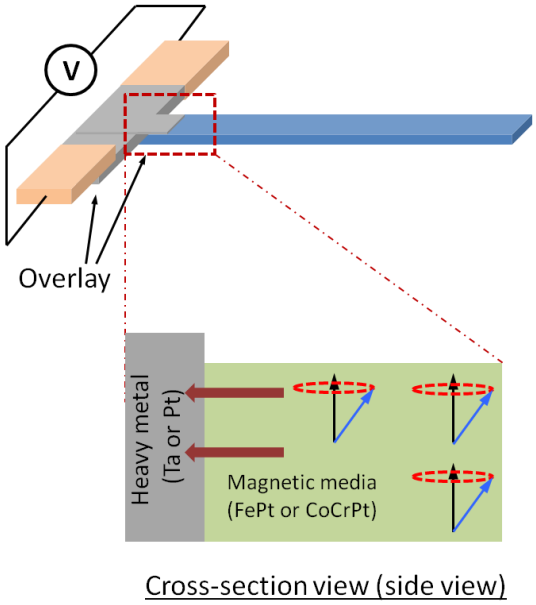

Figure 7-1: Lateral spin-pumping detection scheme in FePt.

(b) The studies of spin wave characterization in large-area thin films have revealed the existence of multiple modes in in-plane anisotropy materials leading to varied forms of spin wave interference [164, 166, 178]. It has been postulated [181] and shown in recent reports that perpendicular standing spin wave (PSSW) modes have a frequency far higher than the FMR frequency of the material, and can be utilized for switching materials such as FePt [93]. It would be interesting to characterize the spin wave modes, by experiment and simulations, in the above sample configuration to identify features that can be tuned for potential applications.

(c) The use of a square pulse excitation raises interesting questions on the feasibility of spin waves in applications for information processing as interference or cross-talk is undesirable. Hence, it is important to analyze the magnetization dynamics and subsequent reversal dynamics in FePt for different pulse excitation shapes. While a single frequency excitation avoids the issues of interference, a square pulse excitation comprises

several frequencies in its spectrum that may include the natural frequency of the material under consideration. Such an excitation method might be more efficient in reversing the magnetization of high-frequency PMA materials, or even exciting higher-order magnetization dynamics.

Diffusion studies in extremely thin MgO barriers for magnetic tunnel junction (MTJ) applications The results in this thesis demonstrated that for MTJs with MgO barrier thicknesses of 1nm and less, the diffusion rate of Mg into the ferromagnetic layers may play a key role in determining the quality of the MTJ device. It is necessary to carefully characterize the diffusion effects at different annealing temperatures and annealing times to create a high RA product device which can reduce the critical switching current density (J_c) in nano-sized MTJs under the influence of the spin transfer torque (STT) effect.

Synchronization of spin torque oscillator devices by propagating spin waves Several synchronization schemes have been suggested for coupling more than two STOs; however, the best result achieved till date is the synchronization of four spin-torque vortex oscillators (STVO) [136, 137, 215]. An interesting approach is to use propagating spin waves to mutually phase-lock a line of STOs. The propagation direction of the spin wave must be perpendicular to the STO array, and the mutually phase locking can be characterized by a spectrum analyzer connected to one of the nanopillar devices. It would also be worthwhile to analyze the distance dependence of such a synchronization scheme for comparison with other schemes.

References

[1] Frost & Sullivan, 2013 Global Storage Market Research Report.(2013).
[2] M. Murphy *et al.*, Phys. Rev. A 82, 022318 (2010).
[3] M. N. Baibich *et al.*, Phys. Rev. Lett. 61, 2472 (1988).
[4] P. Grünberg, US Patent 4,949,039.(1990).
[5] G. Binasch *et al.*, Phys. Rev. B 39, 4828 (1989).
[6] B. Dieny *et al.*, Phys. Rev. B 43, 1297 (1991).
[7] S. Parkin, N. More, and K. Roche, Phys. Rev. Lett. 64, 2304 (1990).
[8] S. S. P. Parkin, Phys. Rev. Lett. 67, 3598 (1991).
[9] J. S. Moodera *et al.*, Phys. Rev. Lett. 74, 3273 (1995).
[10] T. Miyazaki, and N. Tezuka, J. Magn. Magn. Mater. 139, L231 (1995).
[11] S. S. P. Parkin *et al.*, Nature Mater. 3, 862 (2004).
[12] S. Yuasa *et al.*, Nature Mater. 3, 868 (2004).
[13] S. Ikeda *et al.*, Appl. Phys. Lett. 93, 082508 (2008).
[14] E. Grochowski, *HGST*.(2010).
[15] G. Bertero, IEEE Santa Clara Magnetics Society (2011).
[16] B. Friedrich, and D. Herschbach, Phys. Today 56, 53 (2003).
[17] E. d. T. d. Lacheisserie, Magnetism: Fundamentals (Springer, 2004)
[18] P. P. Freitas, and L. Berger, J. Appl. Phys. 57, 1266 (1985).
[19] L. Berger, J. Appl. Phys. 50, 2137 (1979).
[20] C. Hung *et al.*, J. Appl. Phys. 63, 4276 (1988).
[21] J. C. Slonczewski, J. Magn. Magn. Mater. 159, L1 (1996).
[22] L. Berger, Phys. Rev. B 54, 9353 (1996).
[23] E. D. Daniel, C. D. Mee, and M. H. Clark, Magnetic Recording: The First 100 Years (Wiley-IEEE Press, 1998)
[24] A. S. Hoagland, IEEE Trans. Magn. 39, 1871 (2003).
[25] S. N. Piramanayagam, and T. C. Chong, Developments in Data Storage: Materials Perspective (Wiley-IEEE Press, 2011)
[26] N. Inaba, and M. Futamoto, J. Appl. Phys. 87, 6863 (2000).
[27] C. R. Paik *et al.*, IEEE Trans. Magn. 28, 3084 (1992).
[28] D. E. Laughlin *et al.*, J. Magn. Magn. Mater. 155, 146 (1996).
[29] L. Lee *et al.*, IEEE Trans. Magn. 31, 2728 (1995).
[30] B. B. Lal, M. Tobise, and T. Shinohara, IEEE Trans. Magn. 30, 3954 (1994).
[31] G. Choe *et al.*, IEEE Trans. Magn. 39, 633 (2003).
[32] T. Yoshino *et al.*, Appl. Phys. Lett. 98, 132503 (2011).
[33] D. Weller, and A. Moser, IEEE Trans. Magn. 35, 4423 (1999).
[34] B. R. Acharya *et al.*, J. Magn. Magn. Mater. 260, 261 (2003).
[35] E. N. Abarra *et al.*, IEEE Trans. Magn. 37, 1426 (2001).
[36] J. Lohau *et al.*, Appl. Phys. Lett. 78, 2748 (2001).
[37] S. Iwasaki, and K. Takemura, IEEE Trans. Magn. 11, 1173 (1975).
[38] S. Iwasaki, and Y. Nakamura, IEEE Trans. Magn. 14, 436 (1978).
[39] S. N. Piramanayagam, J. Appl. Phys. 102, 011301 (2007).
[40] S. Khizroev, and D. Litvinov, J. Appl. Phys. 95, 4521 (2004).
[41] H. Uwazumi *et al.*, IEEE Trans. Magn. 37, 1595 (2001).
[42] T. Oikawa *et al.*, IEEE Trans. Magn. 38, 1976 (2002).

[43] G. A. Bertero *et al.*, IEEE Trans. Magn. 38, 1627 (2002).
[44] J. Z. Shi *et al.*, Appl. Phys. Lett. 87, 222503 (2005).
[45] B. R. Acharya *et al.*, IEEE Trans. Magn. 40, 2383 (2004).
[46] S. C. Byeon, A. Misra, and W. D. Doyle, IEEE Trans. Magn. 40, 2386 (2004).
[47] A. Hashimoto *et al.*, INTERMAG 2006. (2006).
[48] L. Lu *et al.*, Appl. Phys. Lett. 103, 042413 (2013).
[49] E. Grochowski, and R. D. Halem, IBM Syst. J. 42, 338 (2003).
[50] H. J. Richter, J. Phys. D Appl. Phys. 40, R149 (2007).
[51] C. P. Bean, and J. D. Livingston, J. Appl. Phys. 30, S120 (1959).
[52] J. Eisenmenger, and I. K. Schuller, Nature Mater. 2, 437 (2003).
[53] S. H. Charap, L. Pu-Ling, and H. Yanjun, IEEE Trans. Magn. 33, 978 (1997).
[54] Hitachi. Please refer to http://www.hitachi.com/New/cnews/080728b.pdf.(2008).
[55] M. H. Kryder *et al.*, Proc. IEEE 96, 1810 (2008).
[56] Y. Wang, Ph.D Dissertation, Carnegie Mellon University (2011)
[57] Please refer to http://www.storagenewsletter.com/rubriques/market-reportsresearch/ihs-isuppli-storage-space/.(2012).
[58] L. L. Burns Jr., and E. O. Keizer, US Patent 2,915,594.(1959).
[59] H. Katayama *et al.*, J. Magn. Soc. Jpn. 23, 233 (1999).
[60] H. Saga *et al.*, Jpn. J. Appl. Phys. 38, 1839 (1999).
[61] R. E. Rottmayer *et al.*, IEEE Trans. Magn. 42, 2417 (2006).
[62] R. Ikkawi *et al.*, J. Nanoelectron. Optoe. 3, 44 (2008).
[63] W. A. Challener *et al.*, Nature Photon. 3, 220 (2009).
[64] J.-G. Zhu, Z. Xiaochun, and T. Yuhui, IEEE Trans. Magn. 44, 125 (2008).
[65] Y. Wang, and J.-G. Zhu, J. Appl. Phys. 109, 07B706 (2011).
[66] D. Karns, INTERMAG 2008 (2008).
[67] W. Peng *et al.*, Tribol. Int. 38, 588 (2005).
[68] L. Li, P. M. Jones, and Y. T. Hsia, Tribology Letters 16, 21 (2004).
[69] C. Thirion, W. Wernsdorfer, and D. Mailly, Nature Mater. 2, 524 (2003).
[70] G. Bertotti, I. Mayergoyz, and C. Serpico, *Nonlinear Magnetization Dynamics in Nanosystems* (Elsevier, 2009)
[71] G. Bertotti, C. Serpico, and I. D. Mayergoyz, Phys. Rev. Lett. 86, 724 (2001).
[72] Z. Z. Sun, and X. R. Wang, Phys. Rev. Lett. 97, 077205 (2006).
[73] W. Scholz, and S. Batra, J. Appl. Phys. 103, 07F539 (2008).
[74] S. Okamoto, N. Kikuchi, and O. Kitakami, Appl. Phys. Lett. 93, 102506 (2008).
[75] Y. Nozaki *et al.*, Appl. Phys. Lett. 91, 082510 (2007).
[76] Y. Nozaki *et al.*, Appl. Phys. Lett. 91, 122505 (2007).
[77] Y. Nozaki *et al.*, Appl. Phys. Lett. 95, 082505 (2009).
[78] Y. Nozaki *et al.*, J. Appl. Phys. 112, 083912 (2012).
[79] T. Moriyama *et al.*, Appl. Phys. Lett. 90, 152503 (2007).
[80] H. T. Nembach *et al.*, Appl. Phys. Lett. 95, 062506 (2009).
[81] H. T. Nembach *et al.*, Appl. Phys. Lett. 90, 062503 (2007).
[82] Y. W. Jian-Gang Zhu, IEEE Trans. Magn. 46, 751 (2010).

[83] S. Okamoto, N. Kikuchi, and O. Kitakami, Appl. Phys. Lett. 93, 142501 (2008).
[84] Z. Wang, and M. Wu, J. Appl. Phys. 105, 093903 (2009).
[85] C. Boone *et al.*, IEEE Magn. Lett. 3, 3500104 (2012).
[86] N. Narita *et al.*, INTERMAG (2014).
[87] M. Igarashi *et al.*, IEEE Trans. Magn. 46, 2507 (2010).
[88] M. Mallary, IEEE Santa Clara Magnetics Society (2012).
[89] Y. Sato, US Patent US 20130271866 A1.(2013).
[90] P. M. Braganca, and B. A. Gurney, US Patent US 20130009712 A1.(2013).
[91] Y. Shiroishi *et al.*, US Patent US 20130229895 A1.(2013).
[92] A. M. Deac *et al.*, Nat Phys 4, 803 (2008).
[93] T. Seki *et al.*, Nat. Commun. 4, 1726 (2013).
[94] T. Yoshioka *et al.*, Appl. Phys. Express 3, 013002 (2009).
[95] F. Bloch, Z. Phys. 61, 206 (1930).
[96] C. W. Sandweg *et al.*, Appl. Phys. Lett. 97, 252504 (2010).
[97] R. W. Damon, and J. R. Eshbach, J. Phys. & Chem. Solids 19, 308 (1961).
[98] J. R. Eshbach, and R. W. Damon, Phys. Rev. 118, 1208 (1960).
[99] R. W. Damon, and H. Van De Vaart, J. Appl. Phys. 36, 3453 (1965).
[100] B. Hillebrands, Spin Dynamics in Confined Magnetic Structures (Springer, 2002)
[101] A. Kozhanov *et al.*, Appl. Phys. Lett. 94, 012505 (2009).
[102] S. O. Demokritov, B. Hillebrands, and A. N. Slavin, Phys. Rep. 348, 441 (2001).
[103] J. H. Kwon, Ph.D Dissertation, National University of Singapore (2013)
[104] D. D. Stancil, and A. Prabhakar, Spin Waves Theory and Applications (Springer, 2009)
[105] B. A. Kalinikos, and A. N. Slavin, J. Phys. C Solid State 19, 7013 (1986).
[106] B. A. Kalinikos, IEE Proc. H 127, 4 (1980).
[107] N. F. Mott, Proc. R. Soc. Lond., A 156, 368 (1936).
[108] S. Ikeda *et al.*, Applied Physics Letters 93, 082508 (2008).
[109] W. H. Butler *et al.*, Phys. Rev. B 63, 054416 (2001).
[110] J. C. Sankey, Ph.D Dissertation, Cornell University (2007)
[111] T. Y. Chen *et al.*, Phys. Rev. Lett. 93, 026601 (2004).
[112] J. Grollier *et al.*, Appl. Phys. Lett. 83, 509 (2003).
[113] S. Urazhdin *et al.*, Phys. Rev. Lett. 91, 146803 (2003).
[114] M. Covington *et al.*, Phys. Rev. B 69, 184406 (2004).
[115] S. I. Kiselev, Nature 425, 380 (2003).
[116] I. N. Krivorotov, Science 307, 228 (2005).
[117] J. Z. Sun, IBM J. Res. & Dev. 50, 81 (2006).
[118] D. C. Ralph, and M. D. Stiles, J. Magn. Magn. Mater. 320, 1190 (2008).
[119] Toshiba. Please refer to http://techon.nikkeibp.co.jp/english/NEWS_EN/20110706/193118/?P=2.(2011).
[120] K. V. Thadani *et al.*, Phys. Rev. B 78, 024409 (2008).
[121] Y. Jiang *et al.*, Phys. Rev. Lett. 92, 167204 (2004).

[122] H. Kubota, Appl. Phys. Lett. 89, 032505 (2006).
[123] H. Meng, and W. Jian-Ping, IEEE Trans. Magn. 41, 2612 (2005).
[124] H. Fukuzawa, H. Yuasa, and H. Iwasaki, J. Phys. D Appl. Phys. 40, 1213 (2007).
[125] D. Bedau *et al.*, Appl. Phys. Lett. 96, 022514 (2010).
[126] E. B. Myers *et al.*, Phys. Rev. Lett. 89, 196801 (2002).
[127] L. Berger, J. Appl. Phys. 93, 7693 (2003).
[128] N. C. Emley *et al.*, Appl. Phys. Lett. 84, 4257 (2004).
[129] Y. Huai *et al.*, Appl. Phys. Lett. 87, 222510 (2005).
[130] J. K. Sankey, Nature Phys. 4, 67 (2008).
[131] H. Kubota, Nature Phys. 4, 37 (2008).
[132] P. M. Braganca *et al.*, Nanotechnology 21, 235202 (2010).
[133] K. Mizushima *et al.*, J. Appl. Phys. 107, 063904 (2010).
[134] P. Villard *et al.*, IEEE J. Solid-State Circuits 45, 214 (2010).
[135] A. Hamadeh *et al.*, arXiv:1311.7096 [cond-mat.mes-hall] (2013).
[136] A. D. Belanovsky *et al.*, Phys. Rev. B 85, 100409 (2012).
[137] C. E. Zaspel, Appl. Phys. Lett. 102, 052403 (2013).
[138] M. Igarashi *et al.*, IEEE Trans. Magn. 48, 3284 (2012).
[139] Y. Sato *et al.*, IEEE Trans. Magn. 49, 3632 (2013).
[140] P. M. Martin, Handbook of deposition technologies for films and coatings (Elsevier, 2009)
[141] L. I. Maissel, and R. Glang, Handbook of Thin Film Technology (McGraw-Hill, 1970)
[142] H. J. Levinson, Principles of Lithography : Third Edition (SPIE Press, 2010)
[143] SUSS Microtec. Please refer to http://www.suss.com/.
[144] A. Grill, Cold Plasma in Materials Fabrication: From Fundamentals to Applications (IEEE Press, 1994)
[145] E. Beaurepaire *et al.*, Magnetism: A Synchrotron Radiation Approach (Springer, 2006)
[146] A. Bisig, Ph.D Dissertation, University of Konstanz (2012)
[147] G. Schütz *et al.*, Phys. Rev. Lett. 58, 737 (1987).
[148] K. Wan-Seop, Ph.D Dissertation, University of Duisburg-Essen (1998)
[149] The Neel Insitut, X-ray Magnetic Circular Dichroism (XMCD). Please refer to http://neel.cnrs.fr/spip.php?article798&lang=fr.
[150] BESSY II. Please refer to http://www.helmholtz-berlin.de/user/experimental-infrastructures/instruments-photons/index_en.html.
[151] L. Reimer, and H. Kohl, Transmission Electron Microscopy: Physics of Image Formation (Springer, 2008)
[152] V. V. Kruglyak, S. O. Demokritov, and D. Grundler, J. Phys. D Appl. Phys. 43, 264001 (2010).
[153] S. Bandyopadhyay, and M. Cahay, Nanotechnology 20, 412001 (2009).
[154] A. V. Gorshkov *et al.*, Phys. Rev. Lett. 105, 060502 (2010).
[155] Y. Kajiwara *et al.*, Nature 464, 262 (2010).
[156] P. Buczek, A. Ernst, and L. M. Sandratskii, Phys. Rev. Lett. 105, 097205 (2010).
[157] S. Kaka *et al.*, Nature 437, 389 (2005).
[158] F. B. Mancoff *et al.*, Nature 437, 393 (2005).

[159] S. S. Mukherjee *et al.*, Phys. Rev. B 85, 094416 (2012).
[160] S. S. Mukherjee *et al.*, Phys. Rev. B 85, 224408 (2012).
[161] J. H. Kwon *et al.*, Appl. Phys. Lett. 99, 132505 (2011).
[162] T. Schneider *et al.*, Appl. Phys. Lett. 92, 022505 (2008).
[163] M. Jamali *et al.*, Sci. Rep. 3, 3160 (2013).
[164] V. E. Demidov *et al.*, Phys. Rev. B 77, 064406 (2008).
[165] V. E. Demidov *et al.*, Appl. Phys. Lett. 95, 112509 (2009).
[166] V. E. Demidov *et al.*, Appl. Phys. Lett. 91, 252504 (2007).
[167] P. Clausen *et al.*, Appl. Phys. Lett. 99, 162505 (2011).
[168] K. Vogt *et al.*, Appl. Phys. Lett. 95, 182508 (2009).
[169] K. Perzlmaier, G. Woltersdorf, and C. H. Back, Phys. Rev. B 77, 054425 (2008).
[170] M. Bauer *et al.*, J. Magn. Magn. Mater. 226, 507 (2001).
[171] J. P. Park *et al.*, Phys. Rev. Lett. 89, 277201 (2002).
[172] A. Barman *et al.*, Phys. Rev. B 69, 174426 (2004).
[173] O. Buttner *et al.*, IEEE Trans. Magn. 34, 1381 (1998).
[174] R. W. Damon, and J. R. Eshbach, J. Appl. Phys. 31, S104 (1960).
[175] J. Kwon *et al.*, Appl. Phys. A 111, 369 (2013).
[176] K. Sekiguchi *et al.*, Appl. Phys. Lett. 97, 022508 (2010).
[177] P. Deorani, J. H. Kwon, and H. Yang, arXiv:1311.2686 [cond-mat.mtrl-sci] (2013).
[178] C. Bayer *et al.*, Phys. Rev. B 69, 134401 (2004).
[179] C. Bayer *et al.*, Appl. Phys. Lett. 82, 607 (2003).
[180] M. Bailleul, D. Olligs, and C. Fermon, Phys. Rev. Lett. 91, 137204 (2003).
[181] J. Jorzick *et al.*, Phys. Rev. Lett. 88, 047204 (2002).
[182] D. R. Birt *et al.*, Appl. Phys. Lett. 101, 252409 (2012).
[183] C. Kittel, Phys. Rev. 73, 155 (1948).
[184] F. Giesen *et al.*, Appl. Phys. Lett. 86, 112510 (2005).
[185] W. Wernsdorfer *et al.*, Phys. Rev. Lett. 77, 1873 (1996).
[186] Y. Tserkovnyak *et al.*, Rev. Mod. Phys. 77, 1375 (2005).
[187] M. V. Costache *et al.*, Phys. Rev. Lett. 97, 216603 (2006).
[188] L. Berger, Phys. Rev. B 59, 11465 (1999).
[189] A. Azevedo *et al.*, J. Appl. Phys. 97, 10C715 (2005).
[190] H. Y. Inoue *et al.*, J. Appl. Phys. 102, 083915 (2007).
[191] P. Deorani, and H. Yang, Appl. Phys. Lett. 103, 232408 (2013).
[192] N. A. Sinitsyn, J. Phys.-Condens. Mat. 20, 023201 (2008).
[193] N. A. Sinitsyn, Q. Niu, and A. H. MacDonald, Phys. Rev. B 73, 075318 (2006).
[194] J. Sinova *et al.*, Phys. Rev. Lett. 92, 126603 (2004).
[195] E. M. Hankiewicz, and G. Vignale, Phys. Rev. B 73, 115339 (2006).
[196] E. M. Hankiewicz, G. Vignale, and M. E. Flatté, Phys. Rev. Lett. 97, 266601 (2006).
[197] G. Vignale, J Supercond Nov Magn 23, 3 (2010).
[198] Y. P. Chen *et al.*, J. Appl. Phys. 110, 053905 (2011).
[199] S. Mizukami, Y. Ando, and T. Miyazaki, Phys. Rev. B 66, 104413 (2002).
[200] T. Taniguchi, and H. Imamura, Phys. Rev. B 76, 092402 (2007).
[201] Y. Tserkovnyak, A. Brataas, and G. E. W. Bauer, Phys. Rev. Lett. 88, 117601 (2002).

[202] R. Urban, G. Woltersdorf, and B. Heinrich, Phys. Rev. Lett. 87, 217204 (2001).
[203] H. Zhang *et al.*, Appl. Phys. Lett. 95, 232503 (2009).
[204] T. J. Silva *et al.*, J. Appl. Phys. 85, 7849 (1999).
[205] P. Martin Pimentel *et al.*, J. Appl. Phys. 102, 063913 (2007).
[206] X. Fan *et al.*, Appl. Phys. Lett. 95, 062511 (2009).
[207] M. Hayashi, Y. K. Takahashi, and S. Mitani, Appl. Phys. Lett. 101, 172406 (2012).
[208] S. Li *et al.*, Appl. Phys. Lett. 94, 202509 (2009).
[209] X. Han *et al.*, Phys. Rev. Lett. 98, 147202 (2007).
[210] OOMMF User's Guide, Version 1.0 (NIST).
[211] R. Yanes *et al.*, Phys. Rev. B 79, 224427 (2009).
[212] M. Grimsditch *et al.*, Europhys. Lett. 54, 813 (2001).
[213] G. Gubbiotti *et al.*, J. Phys.-Condens. Mat. 16, 7709 (2004).
[214] Z. Liu *et al.*, Phys. Rev. Lett. 98, 087201 (2007).
[215] V. S. Pribiag *et al.*, Nature Phys. 3, 498 (2007).

List of Acronyms

A list of the commonly used acronyms used in this thesis is given below.

AC	Alternating current
AFM	Atomic force microscopy
AP	Anti-parallel state
APD	Avalanche photo-diode
BLS	Brillouin light spectroscopy
BPM	Bit patterned media
CCD	Charge-coupled device
CD	Critical dimension
CGR	Cumulative growth rate
CIMS	Current-induced magnetization switching
CMOS	Complementary metal-oxide-semiconductor
CPP	Current perpendicular-to-plane
CPW	Coplanar waveguide
DC	Direct current
DOS	Density of states
EAMR	Energy-assisted magnetic recording
EBL	Electron-beam lithography
ECC	Exchange-coupled media
FFT	Fast Fourier transform
FM	Ferromagnet
FMR	Ferromagnetic resonance
GMR	Giant magnetoresistance
HAMR	Heat-assisted magnetic recording
HDD	Hard disk drive

ISHE	Inverse spin Hall effect
LLG	Landau-Lifshitz-Gilbert equation
LMR	Longitudinal magnetic recording
MAMR	Microwave-assisted magnetic recording Microwave-assisted magnetization reversal
MAS	Microwave-assisted switching
MFM	Magnetic force microscopy
MOKE	Magneto-optical Kerr effect
MRAM	Magnetoresistive random access memory
MSSW	Magnetostatic surface spin waves
MSBV	Magnetostatic backward volume spin waves
MSFV	Magnetostatic forward volume spin waves
MTJ	Magnetic tunnel junction
NA	Numerical aperture
NFT	Near field transducer
NM	Non-magnet
Oe	Oersted
OOMMF	Object-oriented micromagnetic modelling framework
OSA	Order selecting aperture
P	Parallel state
PEEM	Photoemission electron microscopy
PGM	Plane grating monochromator
PMR	Perpendicular magnetic recording
RA	Resistance-area product
RF	Radio frequency
SAED	Selective area diffraction
SEM	Scanning electron microscopy

SEMPA	Scanning electron microscopy with polarization analysis
SIMS	Secondary ion mass spectrometer
SNR	Signal-to-noise ratio
SPM	Scanning probe microscopy
STM	Scanning tunneling microscopy
STO	Spin torque oscillator
STS	Spin transfer switching
STT	Spin transfer torque
STT-RAM	Spin transfer torque – random access memory
STXM	Scanning transmission X-ray microscopy
SUL	Soft magnetic underlayer
TMR	Tunnel magnetoresistance
T	Tesla
TEM	Transmission electron microscopy
UV	Ultra-violet
VNA	Vector network analyzer
XMCD	X-ray magnetic circular dichroism

List of Publications and Conferences

Publications in Peer-reviewed journals

1. **S. Rao**, S.S. Mukherjee, M. Elyasi, C. S. Bhatia, and H. Yang, "Spin pumping-mediated characterization of microwave-assisted magnetization reversal", Applied Physics Letters **104**, 122406 (2014).

2. **S. Rao**, J. Yoon, J. Rhensius, C. S. Bhatia, and H. Yang, " Spin wave non-reciprocity and beating in permalloy by time-resolved magneto-optical Kerr effect", Journal of Physics D: Applied Physics (accepted).

3. **S. Rao**, J. Rhensius, A. Bisig, M-A Mawass, M. Weigand, M. Kläui, C. S. Bhatia, and H. Yang, "Time-resolved imaging of microwave-assisted magnetization reversal in patterned structures", Physical Review Letters (submitted).

Conferences

1. **S. Rao**, J. Rhensius, A. Bisig, M-A Mawass, M. Weigand, M. Klaui, C.S. Bhatia, and H. Yang, "Characterization of microwave-assisted magnetization reversal by time-resolved imaging and spin pumping-based electrical methods", submitted to the International Magnetics conference (INTERMAG), 2014.

2. **S. Rao**, J. Yoon, J. Rhensius, C.S. Bhatia, and H. Yang, "Observation of spin wave beating interference in the time domain", submitted to the International Magnetics conference (INTERMAG), 2014.

3. J. Yoon, **S. Rao**, J. Rhensius, C.S. Bhatia, and H. Yang, "Spatially confined effect of propagating spin waves in permalloy microstripes", submitted to the International Magnetics conference (INTERMAG), 2014.

4. M. Elyasi, **S. Rao**, C.S. Bhatia, and H. Yang, "An energy approach modeling algorithm for microwave assisted magnetization reversal to track spin wave evolutions", submitted to the International Magnetics conference (INTERMAG), 2014.

5. M. Elyasi, **S. Rao**, C.S. Bhatia and H. Yang, "Generalized analytical approach for microwave-assisted magnetization reversal based on energy storage and dissipation", presented at the 58th Annual Magnetism and Magnetic Materials (MMM) conference, November 4 -8, 2014 in Denver, USA. (Poster)

6. **S. Rao**, J. Rhensius, A. Bisig, M-A Mawass, M. Weigand, M. Klaui, C.S. Bhatia, and H. Yang, "Direct imaging of microwave-assisted magnetization reversal (MAMR) in patterned elements", presented at the 58th Annual Magnetism and Magnetic Materials (MMM) conference, November 4 -8, 2014 in Denver, USA. (Poster)

7. S. S. Mukherjee, **S. Rao**, P. Deorani, J. H. Kwon, and H. Yang, "The study of microwave assisted magnetization reversal via spin pumping", presented at the 19th International Conference on Magnetism with SCES, July 8-13, 2012 in Busan, South Korea. (Poster)

8. S. S. Mukherjee, P. Deorani, **S. Rao**, J. H. Kwon, and H. Yang, "Effects of nonlinear spin dynamics on spin pumping", presented at the 19th International Conference on Magnetism with SCES, July 8-13, 2012 in Busan, South Korea. (Poster)

9. **S. Rao**, A. M. Sahadevan, S. S. Mukherjee, C. S. Bhatia, and H. Yang, "High Frequency Magnetic Noise in CoFeB/MgO/CoFeB Magnetic Tunnel Junctions: a Field and Bias-dependence Study", presented at the International Conference of Young Researchers on Advanced Materials (ICYRAM), July 1-6, 2012 in Singapore. (Poster)

10. **S. Rao**, J. H. Kwon , S. S. Mukherjee, C. S. Bhatia, and H. Yang, "Low power microwave-assisted magnetization reversal in permalloy microstructures", presented at the International Conference of Young Researchers on Advanced Materials (ICYRAM), July 1-6, 2012 in Singapore. (Poster)

Miscellaneous

1. Invited as a guest scientist at the BESSY II synchrotron facility at HZB, Berlin, Germany for a 2-week period from 25th March – 7th April, 2013.

2. Best poster award at the IEEE Magnetics Society Singapore chapter poster presentation competition organized by Institute of Materials Research & Engineering (IMRE), Singapore, October 30th, 2012. Poster topic: "The study of microwave assisted magnetization reversal via spin pumping."

3. Amongst 6 finalists for 'Best Poster' from over 1500 posters at the 19th International Conference on Magnetism with SCES (ICM) 2012, South Korea. Poster topic: "The study of microwave assisted magnetization reversal via spin pumping".

4. Student Travel Award for ICM, Busan 2012, INTERMAG, Dresden 2014.

5. CAP attained in NUS examinations: 4.00/5.00